DOCTOR OF PHILOSOPHY

Mathematical models of hyphal tip growth

Mohd Jaffar, Mai

Award date:
2012

DOCTOR OF PHILOSOPHY

Mathematical models of hyphal tip growth

Mai Mohd Jaffar

2012

University of Dundee

Mathematical Models of Hyphal Tip Growth

By

M. Z. Ahlam M. Jaffar

Doctor of Philosophy

Division of Mathematics

University of Dundee

Dundee

March 2012

Contents

List of Figures

Acknowledgements

I would like to express my heartiest gratitude to God the Almighty for giving me a chance to go to through this journey along with its deep-seated lessons. Thank you so much to my supervisor, Dr. Fordyce Davidson, for his guidance, encouragement and continuous support through this PhD journey. I wish also to thank the other members of staff of Division of Mathematics and other people I have known in my life so far.

I am greatly indebted to my beloved father (1932-1999) and my beloved mother (1938-2011). This PhD thesis is specially dedicated to them.

Declaration

I declare that the following thesis is my own composition and that it has not been submitted before in application for a higher degree.

M. Z. Ahlam M. Jaffar

Certification

This is to certify that M. Z. Ahlam M. Jaffar has complied with all the requirements for the submission of this Doctor of Philosophy thesis to the University of Dundee.

Dr. Fordyce Davidson

Abstract

Filamentous fungi are important in an enormous variety of ways to our life, with examples ranging from bioremediation, through the food and drinks industry to human health. These organisms can form huge networks stretching metres and even kilometres. However, their mode of growth is by the extension of individual hyphal tips only a few microns in diameter. Tip growth is mediated by the incorporation of new wall building materials at the soft apex. Just how this process is controlled (in fungi and in cell elongation in other organisms) has been the subject of intense study over many years and has attracted considerable attention from mathematical modellers.

In this thesis, we consider mathematical models of fungal tip growth that can be classified as either geometrical or biomechanical. In every model we examine, a 2-D axisymmetric semihemisphere-like curve represents half the medial section of fungal tip geometry.

A geometrical model for the role of the Spitzenkorper in the tip growth was proposed by [7], where a number of problems with the mathematical derivation were pointed out by [50]. A suggestion is given as an attempt to revise the derivation by introducing a relationship between arc length of a growing tip, deposition of wall-building materials and tip curvature.

We also consider two types of geometrical models as proposed by [31]. The first type considers a relationship between the longitudinal curvature and the function used to model deposition of wall-building materials. For these types

of models, a generalized formulae for the tip shape is introduced, which allows localization of deposition of wall-building materials to be examined. The second type considers a relationship between longitudinal and latitudinal curvatures and the function used to model deposition of wall-building materials. For these types of models, a new formulation of the function used to model deposition of wall-building materials is introduced.

Finally, a biomechanical model as proposed by [36]. Varying arc length of the stretchable region on the tip suggests differences in geometry of tip shape and the effective pressure profile. The hypothesis of orthogonal growth is done by focusing only on the apex of a "germ tube". Following that, it suggests that material points on the tip appear to move in a direction perpendicular to the tip either when surface friction is increased or decreased.

Introduction

The purpose of this section is to describe the statement of the problem that motivates our research.

Filamentous fungi are important in an enormous variety of ways, which provide advantages and disadvantages to our life. Fungi are morphologically complex organisms, differing in structure at different times in their life cycle, differing in form between surface and submerged growth, differing also with the nature of the growth medium and physical environment. Investigating fungal tip growth has long been a topic of interest among researchers. The tip is considered to be more stretchable than more distal regions. The growth is apical, namely, the growth extension is at the tip of the cell and the building of new cell wall occurs mainly in the vicinity of the tip. However, up to now, the development of fungal tip growth is not yet fully understood and this inspires mathematicians as well to model fungal growth. Here we use mathematics in describing growth of a single filament of fungi called hypha.

Mathematical modeling of fungal hyphal tip growth can be classified as either geometrical or biomechanical. Both geometrical and biomechanical models have been approached in a variety of ways in order to provide quantitative descriptions and predictive analysis of fungal growth evolution and morphology. Examples of geometrical models are [7, 29, 31, 84]. Examples of biomechanical models are [64] (plant cell tip growth), [13] (root hair tip growth), [23] (root hair tip growth) and [32, 33, 34, 36] (general models of tip growth for filamentous

cells). In the geometrical models, the increase in wall area of an advancing tip is balanced with deposition of wall building materials without specifying the details of underlying biological processes involved. Geometrical models can often be at least partially solved analytically. In the biomechanical models, growth can be modeled by mathematically formulating mechanical processes experienced by a propagating tip. Biomechanical models can prove quite difficult because it involves complexity and challenges in numerical computation. In every model, a 2-D axisymmetric semihemisphere-like curve, C, represents half the medial section of hyphal filament geometry. Choosing an axisymmetric curve can simplify computations and generate a surface of revolution rotated about the chosen axis of symmetry through an angle of 2π.

In Chapter 2, we examine geometrical models proposed by [7, 31], where in [31] involves two different models. We first consider a geometrical model for the role of the Spitzenkorper in tip growth as proposed by [7]. It was demonstrated that the Spitzenkorper is a dynamic accumulation of vesicles that has essential roles in tip expansion. In this model, the Spitzenkorper is identified as the Vesicle Supply Center (VSC). This model predicts that the VSC releases exocytic vesicles in all directions while it moves forward. Following that, it generates an exocytosis gradient that shapes the hypha, known as the hyphoid curve, C. An equation known as hyphoid equation was derived to describe C relating deposition of exocytic vesicles per unit time, N, with speed of the VSC, U_0 and is defined by

$$y = x \cot\left(\frac{U_0}{N}x\right). \tag{1}$$

A number of problems with the derivation of Equation (1) were pointed out by [50]. Despite the erroneous derivation, the hyphoid shape does produce a remarkably good fit to images of real hyphal tips. This motivates us to revise

its derivation. A 2-D curve C on the (x, y)-plane shown in Figure 1 represents half the medial section of a generic hyphal tip and is assumed to be axisymmetric about the y-axis and is given as

$$y = C(x, t), \tag{2}$$

where, C is assumed to be axisymmetric about the y-axis and t represents time.

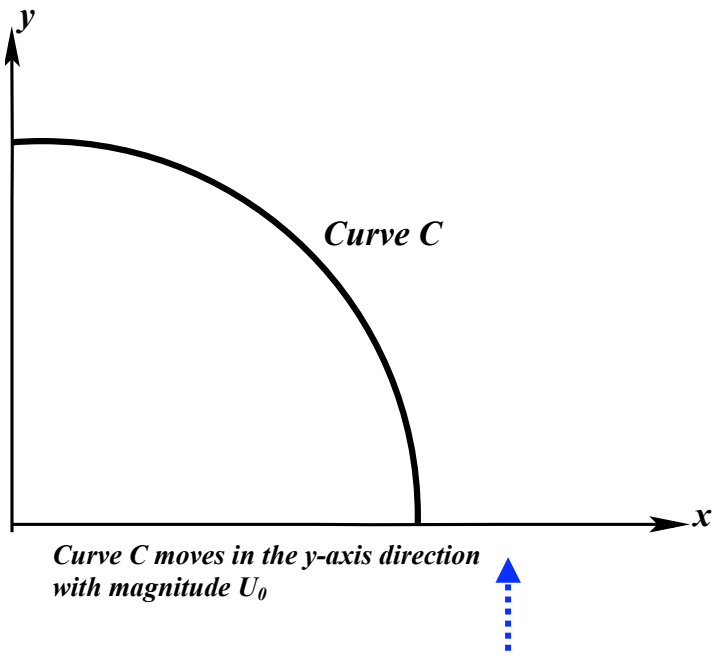

Figure 1: The medial section, C, of a generic hyphal tip. Only half the section is considered for clarity. Redrawn from [7].

As described in Figure 1, the growth direction of the hyphal tip is set in the y-direction. While releasing exocytic vesicles equally in all directions at given time t, the VSC moves forward along the y-axis with magnitude U_0. Assuming that the profile C is translated in the y-direction with speed U_0, then

$$C(x, t) = C(x, 0) + U_0 t. \tag{3}$$

From that it follows Equation (3) describes the translation of a self-similar shape. Then, [7] transformed Equation (2) in terms of polar coordinate system as follows

$$(x, y) \quad = \quad (r \sin \beta, r \cos \beta), \tag{4}$$

where r is radius and β is the angle to the y-axis. A description of Equation (3) in terms of polar coordinates is done first by differentiating both sides of Equation (4) with respect to β and r, which yields $(dx, dy) = (\sin \beta dr + r \cos \beta d\beta, \cos \beta dr - r \sin \beta d\beta)$. Since $y' = \frac{dy}{dx}$ and so $y' = \frac{\cos \beta \frac{dr}{d\beta} - r \sin \beta}{\sin \beta \frac{dr}{d\beta} + r \cos \beta}$. Finally, let $r = \rho(\beta, t)$ be the equation for Equation (2). Then by directly substituting Equation (4) into Equation (2) leads to

$$\rho(\beta, t) \cos \beta \quad = \quad C(\rho(\beta, t) \sin \beta, t). \tag{5}$$

The authors in [7] claimed that Equation (5) is equivalent to

$$\rho(\beta, t) \cos \beta \quad = \quad C(\rho(\beta, t) \sin \beta, 0) + U_0 t. \tag{6}$$

However, Equation (6) is incorrect. In fact, $C(x, 0) = C(\rho(\beta, 0) \sin \beta, 0)$ and so Equation (6) should read as

$$\rho(\beta, t) \cos \beta \quad = \quad C(\rho(\beta, 0) \sin \beta, 0) + U_0 t. \tag{7}$$

Differentiating both sides of Equation (7) with respect t yields

$$\rho_t(\beta, t) \cos \beta \quad = \quad U_0. \tag{8}$$

Equation (8) is correct but simply repeats the original assumption that the curve, C, is translated in the y-direction with the speed U_0. The subsequent analysis in [7] is therefore redundant. We then investigated a possibility of alternative derivation for the hyphoid equation.

We then consider two types of geometrical models proposed by [31] using curve dynamical assumptions, which relate curvatures of the hyphal tip with its surface growth. A 2-D curve on the (x, y)-plane, C, represents half the medial section of hyphal filament geometry shown in Figure 2, which is parameterized by arc length, s, and time, t and axisymmetric about the y-axis. The growth direction is set in the y-direction. Based on [31], it assumes s is given as a function of σ and t, that is, $s = s(\sigma, t)$, where σ is a material point on the tip surface. The growth direction of the hyphal tip is set in the y-direction with speed magnitude U_0. It is assumed that material points on the tip surface are moving perpendicular to the surface as tip grows, which is based on the hypothesis of orthogonal growth as proposed by [67]. The curve C is defined by

$$\underline{\mathrm{r}}_C(s(\sigma,t),t) \;=\; (x(s(\sigma,t)), y(s(\sigma,t)) + U_0 t). \tag{9}$$

From Equation (9), although there is no time dependence in x and y, s is dependent to time. Obviously, each value of s determines a point (x, y)-plane on C.

In [31], it introduced growth rate of the tip wall as

$$\frac{1}{\Delta A}\frac{d}{dt}\Delta A \;=\; \frac{\frac{\partial s}{\partial t}\frac{dx}{ds}}{x} + \frac{1}{\lambda}\frac{\partial \lambda}{\partial t}, \tag{10}$$

where ΔA represents a "band" of increment of area around the tip shown in Figure 3 and λ represents the longitudinal tip stretching.

The growth of an area element per (unit) area element is denoted by the left-hand side of Equation (10). While, the right-hand side of Equation (10) can be

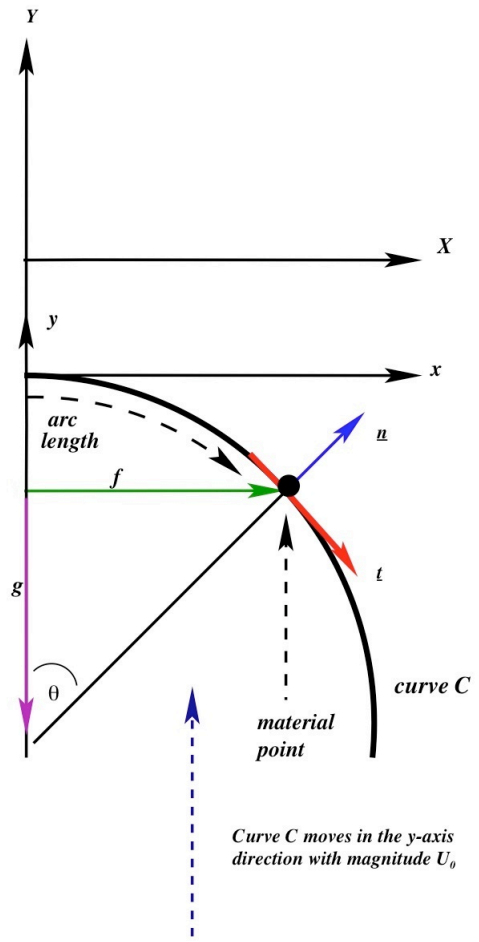

Figure 2: The medial section, C, of a generic hyphal tip. For a given material point, σ, arc length, $s(\sigma)$, is measured from the apex of the shell to that point, $f(s)$ is the radial distance from the y-axis to that point and $\underline{\mathbf{n}}$ and $\underline{\mathbf{t}}$ denote the normal and tangent vectors, respectively. The angle, $\theta(s)$, is the angle between the normal direction and the y-axis. Only half the section is shown for clarity. Redrawn from [31].

thought as the sum of local latitudinal and longitudinal stretching rates. Then, [31] made an assumption that approximately equates the new incremented area to wall-building material deposition as follows

$$\frac{1}{\Delta A}\frac{d}{dt}\Delta A \quad = \quad N(s,t), \tag{11}$$

where $N = N_0 n(s,t)$. Here N_0 sets the fundamental time scale of the wall

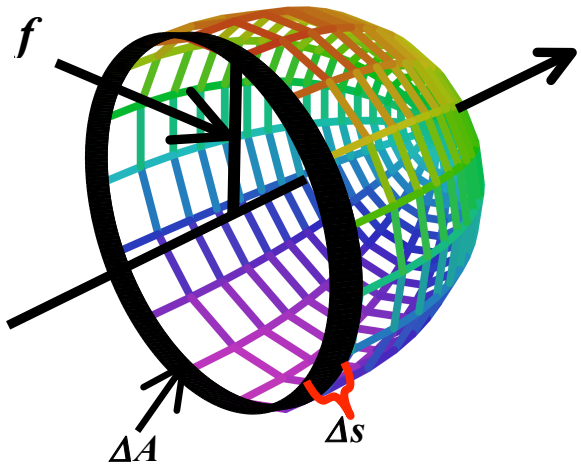

Figure 3: A "band" of increment of area ΔA around the tip and Δs represents the "band" width.

building process and $n(s,t)$ is a dimensionless function used to model the wall-building process.

The first type of geometrical model proposed by [31] considers the longitudinal stretching rate, namely,

$$\frac{1}{\lambda}\frac{\partial \lambda}{\partial t} = N_0 n(s,t). \tag{12}$$

Also, [31] further assumed that the longitudinal curvature, κ, is associated to $n(s,t)$. The relationship of κ and $n(s,t)$ is assumed to be of the form

$$n(s,t) \propto \kappa^p, \tag{13}$$

where $p \geq 1$. It was shown that $p = 1$ results in the irrelevant solution. The choice of $p = 2$ was chosen as it provides a closed form solution and an explicit form of the tip shape. Two questions arised from the first model proposed by [31]: i) Is it necessary to have $p \geq 1$ for growth concentrate at the tip? ii) Apart from the closed form solution and the explicit tip shape, what are other features represented by the model? These questions motivate us to investigate $p \geq 0$

closer, namely, effect of choosing different p on the geometric tip shape and what it says about localization of deposition of wall-building materials.

The second type of geometrical model proposed by [31] considers the sum of local latitudinal and longitudinal stretching rates, namely

$$\frac{\frac{\partial s}{\partial t}\frac{dx}{ds}}{x} + \frac{1}{\lambda}\frac{\partial \lambda}{\partial t} = N_0 n(s,t). \tag{14}$$

A relationship between the function used to model the wall-building material deposition, $n(s,t)$, and the curvatures is assumed to be

$$n(s,t) = K_g N(K_m, K_g), \tag{15}$$

where K_m represents mean curvature defined by $K_m = \kappa + k$, K_g represents Gaussian curvature defined by $K_g = \kappa k$ and k represents the latitudinal curvature. Choice $N \equiv 1$ is made specific by [31], which yields $n(s,t) \propto K_g$. This choice satisfies the need that growth should be largest at the tip and zero along distal region of the tip. In the second model proposed by [31], we thought that in order to model the growth, N is not necessarily be a constant 1. The possibility of a new choice of N must satisfy with deposition of wall-buidling materials. From that it follows, we investigate such that $N(K_m, K_g) \neq 1$ in order to generate the tip shape.

In Chapter 3, we consider a biomechanical model proposed by [36], which is based on nonlinear elasticity theory for shells. This model employed a formalism for describing the dynamics of thin shells that was developed for biomembranes by [25]. Growth mechanism is modeled by how the cell wall responds elastically to the continuous deposition of wall-building materials. Growth is assumed to be pressure driven.

The hyphal tip is considered as an elastic shell with certain elastic properties depending on the distance from the apex, where thickness of cell wall is assumed

to be a constant. A 2-D curve, C on the (z, y)-plane, represents half the medial section of hyphal filament geometry and is axisymmetric about the z-axis shown in Figure 4, where the growth direction is set in the z-direction. Generally, the curve C is parametric, namely, $(s(\sigma), r(\sigma))$, where s represents the arc length distance of a material point, σ, from the tip, and $r(\sigma)$ is radial distance of σ from the z-axis.

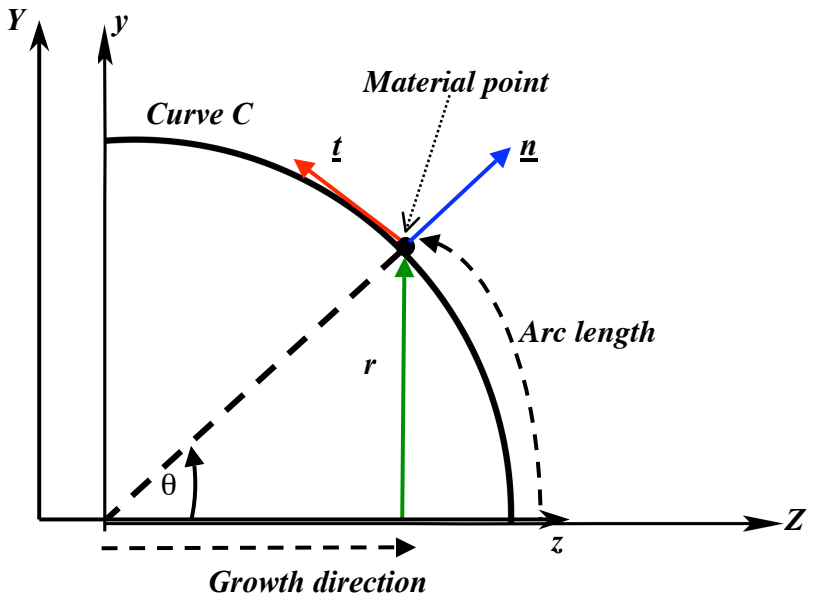

Figure 4: The medial section, C, of a generic hyphal tip. Only half the section is shown for clarity. For a given material point, σ, arc length, $s(\sigma)$, is measured from the apex of the shell to that point, $r(\sigma)$ is the radial distance from the z-axis to that point and $\underline{\mathbf{n}}$ and $\underline{\mathbf{t}}$ denotes the normal and tangent vectors, respectively. The angle, $\theta(s)$, is the angle between the normal direction and the z-axis. Redrawn from [36].

One can generally look at this model as the same formalism that is often used to descirbe the inflation of a balloon, where turgor pressure (the difference of internal and external pressure) is a purely normal stress. In this model, it is assumed that mechanical equilibrium is maintained throughout, where it is described by how the balance between the total normal stress and the total applied force. It is important to note that at the mechanical level, all that the shell

"senses" is the total normal force acting on the tip, not the origin of the forces. The equations of mechanical equilibrium are given by

$$\frac{1}{r}\frac{d(rq_s)}{ds} = q_n - (\kappa_s t_s + \kappa_\varphi t_\varphi), \tag{16}$$

$$\frac{1}{r}\frac{d(rt_s)}{ds} = \frac{\cos\theta}{r} t_\varphi + \kappa_s q_s - \tau_s, \tag{17}$$

$$\frac{1}{r}\frac{d(rm_s)}{ds} = \frac{\cos\theta}{r} m_\varphi + q_s, \tag{18}$$

where:

- θ is angle between the normal vector and the z-axis at a given σ on the tip surface,
- q_n represents the total normal stress,
- κ_s and κ_φ represent longitudal and latitudinal curvatures, respectively,
- t_s and t_φ represent longitudinal and latitudinal stresses, respectively,
- q_s and τ_s represent shear stress normal to the tip surface and tangential shear stress, respectively, and
- m_s and m_φ represent longitudinal and latitudinal bending moments, respectively.

A system of equations (Equations (16)-(18)) has been widely applied to model and examine curved biomembranes (see [72, 73, 80]). Equation (16) is a mathematical statement of balance of normal stresses as described by Young-Laplace equation, where $q_n = \Delta P$. Equation (17) is a statement of balance of tangential shear stress. Equation (18) is a mathematical statement of balance of bending moments.

Constitutive relations are used to close the system of mechanical and geometric equations (Equations (16)-(18)). The stretching of the wall, strain and stress

are linked to each other using the theory of [25]. These relations require the postulation of an elastic energy, W, for an incompressible shell. In this model, the choice of W is the neo-Hookean energy.

The "soft-spot" hypothesis proposed by [67] describes that the newly incorporated material at the tip can flow and therefore easily deform [47]. In this model, a softer material response can be interpreted as an increase in turgor pressure and a rigid material can be interpreted as an decreasing in turgor pressure. An effective pressure profile, $q_n^{(\text{eff})}(\sigma)$, is introduced in order to capture the essence of "soft-spot" and is given by

$$q_n^{(\text{eff})}(\sigma) \;=\; \frac{Q}{2}\left[1-\tanh\left(\frac{\sigma-\sigma_1}{a}\right)\right]+b, \tag{19}$$

where the parameter Q sets the scale of normal stress and the parameters σ_1 and a describe the length of the apical extension zone. The parameter b describes the effective normal force far from the tip; since $\lim_{\sigma\to\infty} q_n^{(\text{eff})} = b$, represents rigid cell walls.

The computation of a growth profile is performed by re-parameterization of the initial profile. That is, after each deformation of the wall, the material points are redistributed uniformly: thereby resetting the arc length along the wall for the next deformation step. Simulation of evolution of tip over a number of time steps is done by using the closed-simplified Equations (16)-(18) expressed all in terms of derivative with respect to σ, a neo-Hookean energy and an initial shell with a soft-spot.

This model is capable of producing a tip-like shape and capture its essential mechanical features. It demonstrates that the tip propagation appears to be self-similar to the tip shape, namely, the newly grown tip looks like a translation of the tip shape at the previous grown tip. Also, the effect of surface friction, τ_s, and the hypothesis of orthogonal growth proposed by [67] are examined. (Note that the

hypothesis of orthogonal growth describes that material points on the tip appear to move in a direction perpendicular to the tip surface as it grows.) Following that, it is suggested that as friction increases, the trajectories of material points tend to align with what would be the equivalent orthogonal trajectories on the tip surface. This is in good agreement with experimental results in [14].

The formulation presented in this model is sufficiently general to accommodate many different effects. What motivates us is to investigate a parameter σ_1, namely, arc length of stretchable region on the tip surface, and then compare it with a choice of $\sigma_1 = \frac{\pi}{12}$ made by [36], as further qualitative exams. That is, the effect of varying σ_1 on geometry of tip shape profile, effective pressure profile and sequence of the effective profile. We then consider to investigate the possiblity of a new "property" that supports the self-similar tip propagation. Finally, we examine the effect of surface friction and the hypothesis of orthogonal growth focused only on the apex of what we assume as the equivalent germ tube.

Finally, in Chapter 4, we conclude by summarising a number of important points and then suggest possible future work.

Chapter 1

Research Background

This chapter begins with a general biological overview of filamentous fungi and then is followed by literature review of mathematical modeling of fungal tip growth.

1.1 General overview: Filamentous fungi

Filamentous fungi are eukaryotic, non-photosynthetic and spore-forming organisms [44, 85]. They contain complicated structures called organelles, bounded by membranes [19, 55]. They are important organisms both in terms of their ecological and economic roles. However, they are also pathogens and are responsible for large economic losses in crops due to their infestations (see [8, 43] for details).

1.1.1 Physiology of Filamentous Fungi

Hypha

A single filament of fungi is called hypha, namely, a tubular-like structure. In a fungal hypha body, a soft-stretchable region is located at the tip, while, a rigid region is at behind the tip [3, 21].

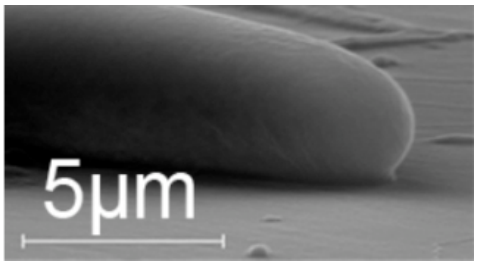

Figure 1.1: Microscope image of the hyphal tip profile of *Aspergillus niger*. Reproduced with kind permission from [12].

A hypha grows in length at its tip. Depending upon environmental conditions and species, a hypha has a relatively constant diameter ranging $1-30\mu m$ and is of indeterminate length. For example, *Neurospora crassa* can grow up to $30-40\mu m$ long. Certain hypha has the ability to extend over long distances, that is, up to $30m$. Thickness of the cell wall shows great variability. In *Neurospora crassa*, the wall is around $50nm$ thick at the apex and at distal region of the tip, wall thickness can be up to $125nm$ [22, 46]. Microscope image of the hyphal tip profile of *Aspergillus niger* [12] is shown in Figure 1.1.

The most important region in a hypha is apical region of the tip, where it is a centre of its growth activity. Also, the building of new cell wall occurs mainly in the vicinity of the tip. As the tip is continually stretched and "rebuilt", the more remote portions of the hyphal wall rigidify [31, 33, 34, 35, 36].

Wall

The fungal cell wall is an elasticity hardy structure. Generally, it is made up of a major percentage of polysaccharide (polymeric carbohydrate) along with a small percentage of lipid, protein, melanin and other components (see Figure 1.2 [2] for further details). However in certain fungi, the polysaccharide is mainly microfibrils of chitin (stiff and flexible polymer molecules), which can be found in

arthropod exoskeleton. Two of the main functions of the fungal cell wall are maintenance of the cell shape and protects the cell against mechanistic environment [2, 26, 58, 85].

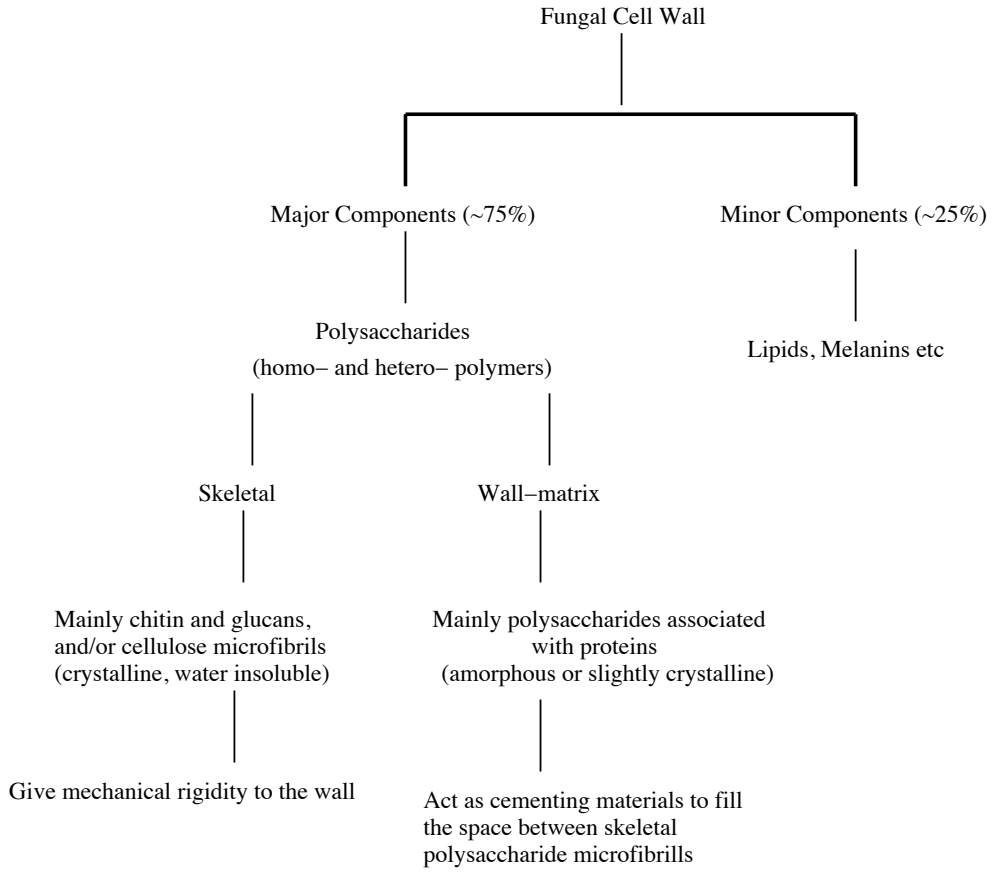

Figure 1.2: Schematic representation of composition of the fungal cell wall and its general functions. Redrawn from [2].

Plasma Membrane

Beneath the cell wall is the plasma membrane, which is a phospholipid (a class of lipids) bilayer scattered with globular proteins. It mainly consists of the sterol ergosterol and lipoprotein. The plasma membrane primarily acts as a selective permeability barrier. That is, it dictates entry of nutrient and exit of metabolites and represents a selective barrier for their translocation. Also, it is able

to block the entering of unwanted materials, like fungicidal products. A space between external to the plasma membrane and internal to the cell wall is called the periplasmic space [46, 58, 71].

Organelles

Generally, a vesicle is a bubble-like membranous of liquid structure that stores and transports cellular substances, like wall-building materials [2, 24, 55]. In Figure 1.3, it shows diagrammatic representation of the organization of wall growth at the hyphal tip [22]. The presence of large numbers of vesicles can be seen in the apical region of the tip. The organelle called the endoplasmic reticulum is used to produce these vesicles, which are then processed by organelles called golgi bodies. At the tip region, a component within the cytoplasm called the cytoskeleton is an intracellular network that acts as a "platform". It is highly dynamic structural skeleton and also provides the firm support of the cell wall surrounding the hypha. It is filled by large numbers of proteins called actin filaments, microtubules and other unknowns. Microtubules act as the "route" to the delivery of vesicles to the tip wall from golgi bodies. They are composed of the protein tubulin and generally lie parallel to the long axis of hyphae. These, together with microfilaments, composed of the protein actin, and also a number of other associated proteins, have a primary role in vesicle transport and the regulation of vesicle supply to the extreme apex.

Vesicles are involved in cell wall synthesis, delivering wall polymers and appropriate enzymes to the apex. This region can be considered as a "supply center" distributing very large numbers of vesicles to the tip for growth purposes. For example, in *Neurospora crassa*, it has been estimated that 38, 000 vesicles per minute fuse with the hyphal tip [37, 58].

Through light microscopy, the highly vesicular region at the tip of hypha was

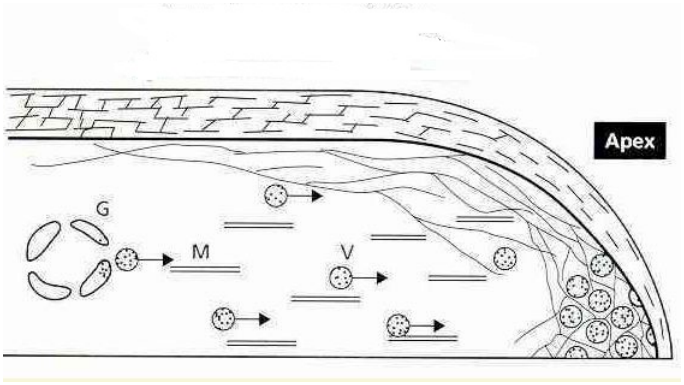

Figure 1.3: Diagrammatic representation of the organization of wall growth at the hyphal tip. Only half of the tip is shown. Vesicles (V) derived from a Golgi body (G) are transported to the apex, perhaps by microtubule (M) mediated systems. The actin meshwork at the apex is thought to provide structural support where the wall is thinnest and where there is little or no cross-linking of wall polymers. Behind the extreme tip, the wall is progressively rigidified by cross-linking of wall polymers. Reproduced with kind permission from [22].

first noticed as a dark spot and named the Spitzenkorper [77]. Furthermore, by using electron microscopy and video microscopy, it has become clear that Spitzenkorper is a highly complex and dynamic region that appears to influence tip growth and the direction of hyphal extension. That is, changes in the growth direction of hypha were accompanied by changes in the position of the Spitzenkorper. Although the Spitzenkorper is an important functioning component of the cytoplasm, it is not strictly an organelle because it is not delimited by a membrane [24, 37].

Different types of vesicles are found in the apical tip region, perform different functions and have different contents. Macrovesicles are within the size range $100 - 300nm$ diameter and microvesicles are $30 - 100nm$ diameter [37, 75]. Macrovesicles secrete the polymers and enzymes that comprise the amorphous phase of the wall, and components of microvesicles constitute the chitin skeleton of the wall. Components of macrovesicles are synthesized internally, whereas the components of microvesicles accumulate at or near a wall-membrane interface.

Cross-link

Some of the major structural components of the fungal cell wall are cross-linked strengthening filaments. Newly added wall components are polymeric molecules, namely, chitin, chitosan, beta-1,3-glucan. As time progresses, these polymers interact to form covalent (chemical bonding) linkages and to cross-link with proteins [58]. It is likely that after receiving newly added wall components, at the extreme tip, the wall is minimally cross-linked and supposed to be more plastic.

Although a great deal is known about components and organization of fungal hypha, the overall operation and control systems at the hyphal tip is not yet completely understood.

1.1.2 Life Cycle of Filamentous Fungi

Germ tube

Spores are reproductive structures of both sexual and asexual natures and are the prime units of dispersal in fungi. The majority of spores located on an appropriate substrate under favorable environmental conditions germinate to produce one or more germ tubes. Some fungal spores, such as the uredospores of rust fungi (Basidiomycota) and the zoospores (motile, flagellate cells) of Chytridiomycota have a fixed point of germination termed the germ pore, where its wall is thinner than elsewhere [22, 58]. Such fungi are able to settle and adhere to receptive surfaces so that their future point of germ tube outgrowth is located next to that surface. However, many spores seem to be able to germinate from any point on the cell periphery. Scanning electron micrograph of germinated conidia of Neurospora crassa interconnected by fused conidial anastomosis tubes [68] is shown in Figure 1.4.

Initially, a fungal spore goes through a process of swelling, where it increases in diameter due to hydration. New wall materials are incorporated over most or all

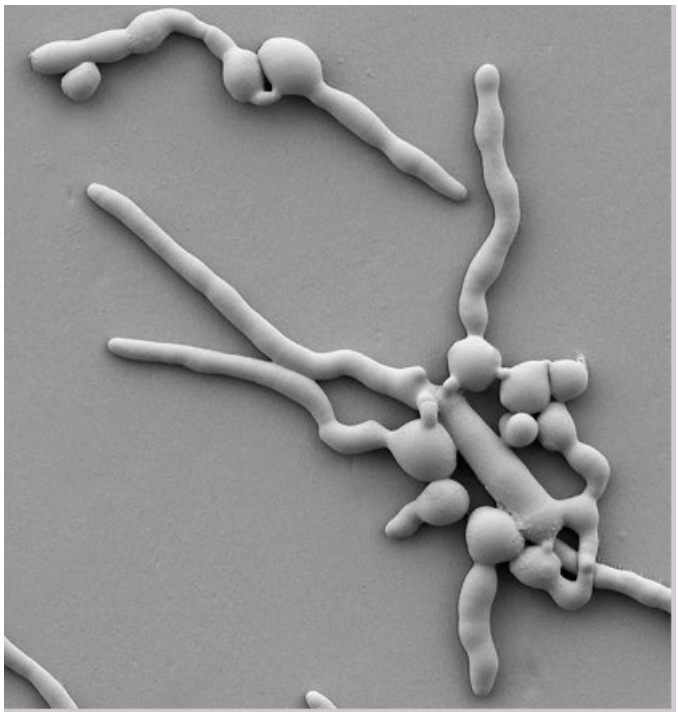

Figure 1.4: Scanning electron micrograph of germinated conidia of Neurospora crassa interconnected by fused conidial anastomosis tubes. Reproduced with kind permission from [68].

of the cell surface. During this phase, the metabolic activity of the spore increases and protein, DNA, and RNA production all increase and so it swells further. This is followed by the emergence of one or more germ tubes from a localized point on the cell surface that extend away from the spore in typical apically polarized manner. The first sign that an apex will emerge is the localized development of an apical vesicular cluster [22, 37, 58].

In *Aspergilus niger*, the transformation from nonpolar to polarized growth is temperature dependent. At a normal temperature of about 30^0C, the spore initially incorporates new wall materials over the whole surface and then an apex is formed. However, when the spores are incubated at 44^0C, they continue to swell for $24-28$ hours, producing giant rounded cells up to $20-25\mu m$ diameter and wall thickness up to $2\mu m$. At this stage, the cells stop growing. But if these "giant cells" are shifted down to 30^0C before they stop growing [22], they will

respond by producing a hyphal apex, and this behaves in an unusual way; instead of forming a normal hypha, it produces a small spore-bearing head.

A spore can remain dormant and delay its germinations due to unfavorable conditions. Examples of these conditions are lack of nutrients, low temperature, an unfavorable pH or the presence of an inhibitor [28] (for example, on a surface of a plant). Spore experiencing one of these conditions is called *exogenously dormant* and will only begin to germinate when environmental conditions become favorable. However, there are also fungal spores that fail to produce spores even under favorable conditions. Factors of such a scenario come from within the spore itself [58], such as nutrient impermeability or the presence of endogenous inhibitors. Spores of this sort are said to be *endogenously dormant*. Dormancy of these spores is usually broken by aging or by some physiological shock permitting nutrients to begin to enter, or the endogenous inhibitors to leach out of the spore [40]. For example, *Neurospora crassa* is broken by a 30-minutes heat shock at 60^0C or exposure to $0.12mM$ furfural.

The production of spores from germinating spores with a minimum of intervening growth is termed microcycle sporulation [78], particularly, if they grow in water films with nutrient-limited conditions. Examples are some saprotrophs on leaf surfaces (*Cladospotrium, Alternaria* spp.) and some leaf-inflecting pathogens (*Septoria nodorum*) [22]. All these fungi will germinate to form normal hyphae in nutrient rich conditions, so their microcylcling behavior in nutrient poor conditions might be a means of spreading to new and potentially more favorable environments [17].

Hyphal Branching

A hypha initiates branches in order to become hyphae, either by internal cross-walls called septa or non-septa walls. Septa are usually perforated by pores

large enough for ribosomes, mitochondria and sometimes nuclei to flow among cells. The processes that control branching are not fully known [24]. Based on demonstration in mutants of *Schizophyllum* and *Neurospora crassa*, it is suggested that branching may be under general control. Microscope image of the branching tip profile of *Aspergillus Niger* [12] is shown in Figure 1.5.

The branch does not seem to emerge from some specific point on the hypha although the formation of branches just behind septa is usually observed. However, the branch initiation is associated with the appearance of a Spitzenkorper at the site of tip emergence and extension [58]. This is exactly as in an aggregation of vesicles at the tip of a single filament hypha. A reasonable suggestion for the origin of branches behind septa is that the septum prevents the passage of some of the vesicles that would ordinarily move to the hyphal tip [46]. As a result of that, an aggregation of tip-forming vesicles is formed just behind the septum forming a tip from which the branch appears.

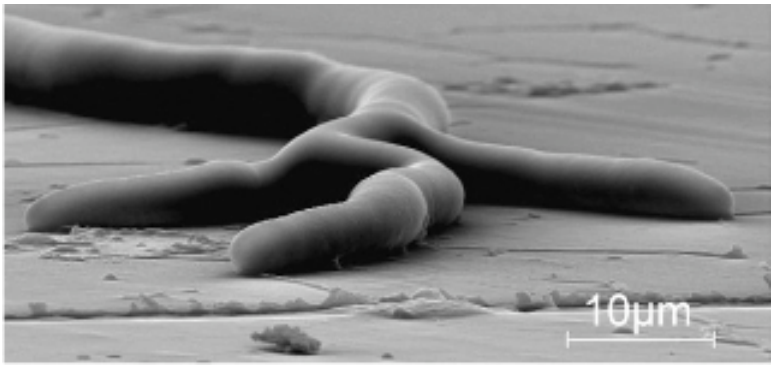

Figure 1.5: Microscope image of the branching tip profile of *Aspergillus Niger*. Reproduced with kind permission from [12].

Hyphae branches may be described as follows: primary (which subtend a primacy branch), tertiary (which subtend a secondary branch) and so on. A sparsely branched colony (low hyphal density) is due to a nutritionally weak growth medium. While, upon a nutritionally rich growth medium, a densely branched colony is developed [24, 58].

Branches extend away from one another and filling the gaps between existing hyphae according to certain 'rules'. In early phases of growth, branches usually subtend an angle of approximately 90^0 to the long axis of the parent hypha. As we have seen, hyphae tend to avoid their neighbors (negative autotropism) and to grow radially away from the centre of the colony [58]. So a circular colony is formed eventually, with radially directed hyphae, approximately equally spaced, and extending at the margin at a constant rate.

Based on study of *Neurospora crassa*, up to about 20 hours of growth, all hyphae have similar diameters, growth zone lengths and extension rates and all branches are at an angle of 90^0 to parent hypha. After about 22 hours growth, branch angle decreases to 63^0, hyphal extension rates and diameters increase [58]. This generally shows that main hyphae are wider and have greater extension rates than their branches. Furthermore, the ratios between diameters of leading hyphae, primary branches and secondary branches being 100: 66: 42 and between extension rates being 100: 62: 26 [58].

Mycelium

A fungal mycelium is a 'mass of hyphae', from which the apically growing hyphae seek out, exploit and translocate available nutrients. On agar in a culture dish, it can grow symmetrically up to 10 cm. However, in nature, it is rarely symmetric. The mycelium spreads throughout its growth environment, such as overripe fruit, wood or soil, and so it is difficult to estimate its actual size [37, 22]. But it is usually large enough to be seen with naked eyes and generally it has a rough-cottony texture [37, 63]. In Figure 1.6, it shows microscope image of the mycelium profile of *P. velutina* [9].

Depending on species and growth conditions, different interconnected regions

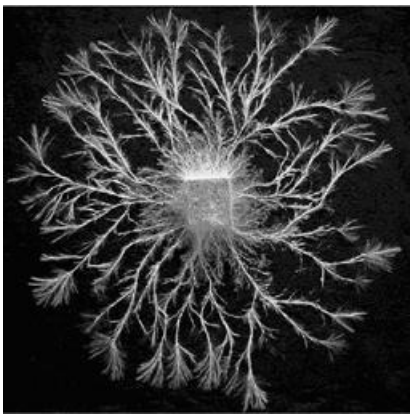

Figure 1.6: Microscope image of the mycelium profile of *P. velutina*. Reproduced with kind permission from [9].

of the fungal mycelium may grow, branch, anastomose (fuse), age, die and sporulate. As a result, it displays a variety of physiological and biomechanical activities at different times or even simultaneously. A mycelium which grows on relatively homogeneous environment condition may be pigmented, exhibit different morphological sectors, produce aerial structures, grow as fast-effuse or slow-dense forms and exhibit rhythmic growth. While, certain fungi, for example, the basidiomycetes grows on heterogeneous environment condition in which nutrients are distributed heterogeneously[58]. They can differentiate into long string-like structures called rhizomorphs or cords. These long string-like structures evolves to rapidly explore for, connect and translocate water and nutrients between patches of resources. Examples of resources are pieces of fallen timber on the forest floor or from tree root to tree root. Accordingly, mature rhizomorphs have wide-diameter internal vessel hyphae. These vessels can be seen as a channel running along the organ. The boundary of hyphae are often closely packed and melanized for insulation [46].

During early growth phase, nutrients are in excess and the young mycelium is unrestricted and undifferentiated. Subsequently, within undifferentiated growth phase, the mean rate of hyphal extension is dependent on the specific growth rate

of the organism (namely, the maximum rate of growth in biomass per unit time) and the manner and degree of branching. By observing the older mycelium, it is notable that hyphal fusions are at its center and hyphal avoidance reactions at its margin [46]. Between them, the distribution of hyphae in a mycelium is influenced by the main growth processes (polarized hyphal growth, branching frequency and autotropism) [17]. Following that, a dynamic relationship occurs in the mycelium, namely, change with the age and with the developmental state as its biological functions change.

Furthermore, the distribution of biomass in a fungal mycelium varies, depending on the age of the hyphae. Generally, one part of a mycelium may be growing rapidly as a rapidly extending, sparsely branched exploratory sector; another part may be a highly branched and interconnected network exploiting nutrients [24]; while a third region reverses the autotropisms so that hyphal tips gather together and cooperate in formation of a fruiting structure [58].

1.1.3 Role In The Environment

Soil

Since filamentous fungi are lack of chlorophyll, they incapable synthesizing their own food and so are designated as heterotrophs. They obtain food through absorption [57].

Absorptive nutrition enables fungi to live as decomposers and symbionts. They absorb small organic molecules from the surrounding medium. Exoenzymes, powerful hydrolytic enzymes secreted by the fungus, break down food outside its body into simpler compounds that the fungus can absorb and use. The absorptive mode of nutrition is associated with the ecological roles of fungi as decomposers (saprobes), parasites and mutualistic symbionts [79]. Saprobic fungi (obtain food from dead tissues or organic waste) absorb nutrients from

nonliving symbionts [22]. Parasitic fungi absorb nutrients from the cells of living hosts. Some parasitic fungi, including some that infect humans and plants, are pathogenic. Fungi cause 80% of plant disease. Mutualistic fungi also absorb nutrients from a host organism but they reciprocate with functions that benefit their partner in some way [69, 79].

Moreover, fungi generally have $40-55\%$ carbon use efficiency so they store and recycle more carbon. Fungi have higher carbon content and less nitrogen in their cells [62]. Fungus helps recycle both nitrogen and phosphorus to plants [4]. Due to their smaller size and much greater surface area, fungus can efficiently scavenge for nitrogen and phosphorus better than plant root hairs and greatly increase the plant root nutrient extraction efficiency. Many plants cultivate certain species of both bacteria and fungus to increase nutrient extraction from the soil [27, 62].

Aqueous

Water is as essential for the growth of fungi as it is for any other organism and, although fungal dispersal structures are often resistant to desiccation, mycelial hyphae are generally poor at withstanding dry conditions. Most require comparatively high levels of water in the environment to enable vegetative growth. The majority of fungi prefer wet aerobic conditions and most of those that are known in culture can be grown in liquid media, in some cases including unamended water [48] (see also [17, 8]). Irrespective of a dependency on high water levels, many fungal excel as ologotrophs, scavenging nutrients from whatever sources that may be available, however dilute or recalcitrant. It is unsurprising therefore that fungi are frequently found in waters of all sorts and that their activities contribute to many of the microbial processes which are of concern to the water-related industries, including biodeterioration, bioremediation, biofilms, biofouling, as well to health effects and taste and odor issues.

In many cases, fungi were detected only incidentally during the course of bacterial isolation programmes. Fungi are to be found in raw (water taken from the environment), surface and groundwater and may increase in numbers in storage reservoirs. More fungi are present in surface water than in groundwater. More fungi are present in untreated than in (chlorine) treatment water [11]. Fungi are less susceptible to chlorine treatment than are bacteria. Sedimentation and flocculation remove many fungi, but rapid filtration is not an effective treatment. There is evidence to suggest that fungi survive and multiply in distribution systems in surface films and in sediments, particularly, where conditions are warmer or flow rates are restricted. Fungi are capable of contributing off-tastes, odors and flavors, but no links to ill health had been reported [48].

Air

As described earlier, each fungal hypha grows in masses to form a network of hyphae called mycelia. Some hyphae extend out from the mycelium and project up into the air [11, 54, 40]. These hyphae are called aerial hyphae. Examples of aerial hyphae are *Fusarium solani*, *Penicilium* and *Aspergilus*. Spores are usually produced on aerial hyphae, where through spores, fungi are reproduced [11, 54].

The orientation 'axis' of these hyphae changed from 'horizontal' to 'aerial'. Growing up in the air allows air currents to carry the spores to new areas through wind or animal contact [22]. Cytoplasm of an aerial hypha is rich with nuclei, which forms into many spores, each containing several nuclei [1]. As the outer layer of the spore case known as sporangium breaks open, either dry spores are shot out and dispersed by air, or spores in a sticky substance are carried away by insects.

Furthermore, when hyphae are growing into the air, they are lined with a layer of hydrophobins (fungal wall protein) [40]. It has been demonstrated that

hydrophobins are very potent surfactant proteins [76, 86] and are able to self-assemble at any hydrophilic/hydrophobic interface. This hydrophobin layer can also be involved in colonization by hyphae of any other hydrophobic surfaces like insect or plant cuticles, wood fragments or other hyphae.

1.1.4 Role In The Industry

Filamentous fungi are used extensively by industry for manufacture of a large variety of useful products. The products include metabolites, enzymes and food.

Food Industry

As food source

Filamentous fungi can be used directly as a food source for human beings. Mycoprotein is a food material which is manufactured by growing a species of the filamentous soil fungus *Fusarium venenatum*. It is sold under the brand Quorn^{TM}. It is a successful application for fungal biomass in the food industry using fungal vegetative growth [46]. Mycoprotein is manufactured by growing the mycellial fungus *Fusarium* in huge fermenters which run continuously for periods of 6 weeks at a time. When the mycoprotein is first produced, it has a fairly bland taste, however it is very versatile because it can easily be flavored, colored and processed in a variety of ways [16, 58]. The market virtues of the material focus on its filamentous structure, which enables it to stimulate the fibrous nature of meat. Quorn^{TM} as an alternative to meat, which is rich with nutritional value of fungal biomass, low-fat, low-calorie, cholesterol-free health food. Although expensive, Quorn^{TM} is sold as a healthy 'meat alternative' [16, 58].

As food processor

Filamentous fungi are also used in the processing of various food products. The fungus role is especially focused on generating a certain characteristic odor, flavor or texture and may or may not become part of the final edible product.

Indonesian tempeh is produced by fermentation of partially cooked soya bean cotyledons with *Rhizopus oligosporus*. The fungus binds the soya bean mass into a protein-rich cake that can be used as a meat substitute. There are a variety of other fermented products of this sort [58, 11, 17]. For example, in China and the the Philippines, ang-kak is a rice product, which is fermented using *Monascus* species. *Monascus purpureus* produces the characteristic pigments and ethanol which are used for red rice wine and food coloring. The pigments are a mixture of red, yellow and polyketides and about ten times more pigment is obtained from solid-state fermentation than from submerged liquid fermentation.

Another fermentation product is soy sauce. Soya beans are soaked, cooked, mashed and fermented with *Aspergillus oryzae* and *A. sojae* [58]. When the substrate has become overgrown with the fungus, the material is transferred to brine and inoculated with the bacterium *Pediococcus halophilus* and 30 days later with *Saccharomyces rouxii*. The brine fermentation takes 6 to 9 months to complete, after which the soy sauce is filtered and pasteurized.

Filamentous fungi have been used for cheese production in Europe. Cheese is a solid or semisolid protein food product manufactured from milk. Some cheeses are produced by species of the genus *Penicillium*, in particular, *P. roqueforti* for blue cheese and *P. camemberti* for white cheese. Two important processes to which filamentous fungi involve are the provision of enzymes for initial coagulation and mold-ripening. Cheese is produced through the action of enzymes, which coagulate the proteins in milk [46], forming solid curds (from which the cheese is made) and liquid whey. Such enzymes and molds are *Aspergillus* species and

Mucor michei [58].

Enzyme Industry

Enzymes are among the most important products obtained for human needs through microbial sources. Also, a large number of industrial processes in the areas of industrial, environmental and food biotechnology utilize enzymes at some stage or the other. Filamentous fungi are easy to be cultivated and have high production of extracellular enzymes of large industrial potential. Filamentous fungi produce different groups of enzymes, as shown briefly in Table 1.1 [70]. These enzymes are used in the industrialization of detergents, starch, drinks, food, textile, animal feed, baking, pulp and paper, leather, chemical and biomedical products [41].

Enzyme production is an increasing field. Enzyme manufacturers produce enzymes either by submerged fermentation (SmF) or solid-state fermentation (SSF). In the case of submerged fermentation (SmF), the microorganisms and the substrate are present in the submerged state in the liquid medium, where a large quantity in the form of solvent is present [65] (see also [2]). Since the contents are in submerged state in the liquid medium, the transfer of heat and mass is more efficient, and is amenable for modeling the process. Solid-state fermentation (SSF) involves the growth of microorganisms on moist solid particles, in situations in which the spaces between the particles contain a continuous gas phase and a minimum of visible water. Although droplets of water may be present between the particles, and there may be thin films of water at the particle surface, the inter-particle water phase is discontinuous and most of the inter-particle space is filled by the gas phase. The majority of the water in the system is absorbed within the moist solid-particles [65].

Filamentous fungi produce a wide range of natural products called secondary

Table 1.1: Enzymes From Filamentous Fungi.

Enzyme	Main Source
Asparaginase	*Aspergillus* spp. and *Penicillium* spp.
Amylase	*A.niger*, *Aspergillus oryzae*
Catalase	*Aspergillus* spp. and *Penicillium* spp.
Cellulase	*A. niger*, *T. reesei*, *T. viride*, *Penicillium finiculosum*,
Dextranase	*Penicillium* spp.
β-Glucanase	*A. niger*, *Penicillium emersonii*, *T. reesei*, *T. viride*
Glucoamylase	A. niger, A. oryzae
Glucose oxidase	*A. niger*, *Penicillium* spp.
Hemicellulase	*A. niger*, *A. oryzae*, *T. reesei*, *T. viride*, *P. emersonii*
Laccase	*Pyricularia oryzae*
Lipase	Several species including *A. niger*, *A. oryzae*
Pectinase	Several species including *A. niger*, *Rhizopus oryzae*
Protease	Several species including *A. niger*, *A. oryzae*

metabolites [82, 51]. Interest in these compounds is considerable as many natural products are of medical, industrial, and/or agricultural importance. For example, penicillin and derivatives, produced by *Aspergillus*, *Cephalosporium* and *Penicillium* species, are widely used as antibiotics [61]; lovastatin is a potent cholesterol-lowering drug produced by *Aspergillus terreus*; and aflatoxins (AFs), produced by several *Aspergillus* species, are highly toxic carcinogens contaminating many agricultural crops [82].

1.1.5 Pathogen

In order to complete a part or all of their life cycle, certain fungi grow inside their host and in so doing has a detrimental effect on their host. A pathogen or

infectious agent is a biological agent that causes disease to its host. Fungal host can be plants, animals or humans.

Plant Pathogen

More than 8,000 described species of fungi are plant pathogens. A variety of symptoms can be seen when the plant is infected [28, 10]. These symptoms are for example, leaf spots and blights, root rots, seedling blights, seed discoloration, wilts and stem rots [59, 60].

Fungal plant pathogens have developed specialist ways of infecting the plants. Some penetrate the plant surface directly using mechanical pressure or enzymatic attack. Others pass through natural plant openings, for example, stomata or lenticels, whilst many take advantage of previous wounds [54]. Once inside the plant, three main colonization strategies are deployed to utilize the host plant as a substrate for pathogen growth and development [42].

Biotrophic (parasitic) plant pathogens ensure the plant cell remains alive. A biotrophic plant pathogen known as *Fulvia (Cladosporium) fulvum* causes blue mould disease of tomato plants. Necrotrophic plant pathogens kill plant cells in advance of colonization [22, 46, 58]. For example, *Botrytis cinerea* is a necrotrophic fungal pathogen, which affects a vast number of economically important crops. Hemibiotrophic plant pathogens initially keep host plant cells alive but then kill them at later stages of the infection. A classic example of hemibiotrophic pathogen is *M. oryzae* that infects exclusively rice [22, 46].

Human Pathogen

There are only a few fungal species that are life-threatening to human health. Both those with immunosuppressed and healthy people can be infected by a fungal pathogen. Infected areas range from the skin to the internal organs [58]. Fungal

infections of humans are common, for example, 50% of woman have been infected by *Candida albicans*. There are only a few species that are life-threatening, for example, farmer's lung infected by *Aspergillus fumigatus*.

Certain environmental and physiological conditions can lead to the development of fungal diseases [1]. For example, surrounding of building renovation, inhalation of fungal spores, localized colonization of the skin, through wounded skin or the ability of the fungi to switch between unicellular yeast cells, hyphae and pseudohyphae (morphological dimorphism).

Fungal infection is easily involved with the skin, the hair and the nails [58]. Dermatophytosis infection is caused by *Epidermophyton*, *Microsporum* and *Trichophyton* genera. These fungi species invade and grow in human dead keratin [11]. Generally, infected skin becomes raised, red, itchy or lesion. Also, infection also may occur from the wounded skin. One example in this case is Sporotrichosis infection caused by *Sporothrix schenckii*.

Fungi infections of the internal organs is thought to enter through the lungs, gastrointestinal tract or intravenous lines. Infection occurs in previously healthy people and arises through the respiratory route [17]. Histoplasmosis infection is caused by *Histoplasma capsulatum*. Opportunistic fungi like *Aspergillus* and *Candida albicans*, infect immunosuppressed individuals easily. Such fungi are dimorphic [58].

Animal Pathogen

It is thought that almost all animals are subject to attack by pathogenic fungi.

Groups of aquatic fungi that attack aquatic animals with Saprolegniasis infection are mainly *Saprolegnia*, *Achlya* and *Aphanomyces*. When a fish is infected, its skin changes from white to brown cotton-like grows on skin, fins, gills and dead eggs. *Saprolegnia* invades epidermal tissues, which initially begins on the

head or fins and can spread over the entire surface of the body [58]. When surface of the skin or gills is damaged mechanically or has an on-going parasitic activity, the fungal spores can easily and frequently penetrate into the fish body.

Fungi also can invade insects by penetrating their cuticle, for example, *Entomophthora muscae* infects flies [58]. Once inside the insect, the fungus can proliferate and disseminate throughout the insect body [22]. Tissue destruction and toxins produced by the fungus lead to death .

Like human, dermatophytosis infection also can attack the animal skin, for instance, guinea pig [58]. The fungi infect keratinized areas of the body, namely, hair, skin and nails [78]. Symptoms include round lesion of scaling skin, hair loss or breakage or sometimes reddened and crusting of infected skin.

1.2 Mathematical Models of Fungal Tip Growth

Filamentous fungi have extraordinary functional intracellular and abilities complexity. Apart from that, they play an important role in our environment and several industries. Following that, the growth of such cells have been a topic of interest and the subject of studies among researches, including mathematicians.

Studies of fungal hyphal tip growth has been done since over 100 years ago. However, the growth mechanism remains to be fully explained. Questions regarding shape maintenance, delivery of wall-building materials and many more have only been answered partially. In fact, only parts of the tip growth process have been investigated and often not based on the same species or the same developmental stage of cell.

Mathematical modeling has contributed a significant role in the development of understanding fungal hyphal tip growth. For many years, modeling techniques have been employed in this area, either based on, or assisted by mathematical modeling. Subsequently, it can help to provide quantitative descriptions and

predictive analysis of their temporal evolution and morphology. This is because mathematics is a powerful and efficient method of investigation, which is able to capture deep insight into the complex interactions of their biological system.

Construction of a meaningful mathematical description of fungal hyphal tip growth is quite a challenge. Describing this process mathematically has been approached in a variety of ways, ranging from geometrical to biomechanically to delivery of vesicles based models. In the following section, we will review a number of mathematical models used in this area.

1.2.1 Geometrical model

The geometrical model provides the most basic representation of the possible tip shape. Generally, such description is developed by describing a relationship between the increase in wall area of a growing tip and deposition of wall-building materials. Following that, it can often be at least partially solved analytically. Also, it is easy to examine the effectiveness of the involved parameters towards the growth, for example, which parameter drives the formation of narrower tip shape [47].

In early stage of mathematical modeling of fungal hyphal tip growth, a number of mathematical models have been proposed, for example, in [39, 84]. A relationship between the mechanism of wall-building material deposition and the tip shapes adopted by the hyphal extension zone was proposed. These predetermined tip shapes were joined onto a cylindrical tube. Basically, the generated tip shapes did not evolve naturally through the mathematical rules or assumptions. Most of the early models were presented either without better knowledge of underlying growth processes or with observation of the tip growth.

In more recent times, the tip shape evolves automatically from a description of tip growth in a mathematical form, which provides a much better insight of

fungal hyphal growth [20].

Hypothesis of Cosine Relationship

In 1966, [39] proposed a mathematical model of hyphal tip growth. Note that this work applied a model to describe hyphal growth of a plant tip, namely, alga *Nitella* [37]. Having said that, it was used as a reference for fungal hyphal tip growth by [84]. Although there are obvious fundamental differences in the internal cellular structure and wall composition, there appear to be certain common characteristics in the growth of these diverse cells at the morphological level. That is, the growth extension is at the tip and the building of new cell wall occurs mainly in the vicinity of the tip [31, 33, 34, 35, 36].

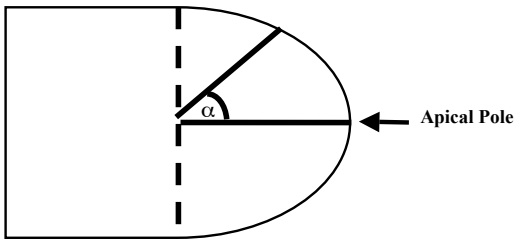

Figure 1.7: A mental picture of the medial section of a generic hyphal tip, where only half the section is considered, proposed by [39]. It describes hypothesis of cosine relationship for hyphal tip growth. The angle α, is the angle between the longitudinal axis and the line drawn hemishphere to the point on the wall being considered. Redrawn from [4].

The concept of a relationship between tip shape and growth mechanisms mediated through expansion of the tip acting against wall-building materials with different degrees of extensibility was introduced. This work proposed that the gradient of wall expansion needed to generate a tubular cell by tip growth followed a cosine function of an angle that measures the displacement of a growing point along apical dome. Such hypothesis describes a cosine relationship between the specific rate of wall expansion and distance from the hyphal apex.

A simple mental picture of the medial section of a generic hyphal tip, where only half the section is considered is shown in Figure 1.7. Accordingly, the tip shape was predetermined by assuming that it is hemispherical.

To get a rough idea on modeling of tip expansion, please refer to Figure 1.8. Accordingly, parameters of interest are: m is the length of the meridional arc from the apex to a point on the circle, l is the latitudinal length from the apex to a point on the circle, r is the radius of the extension zone at the appropriate point on the tip wall, R is the radius at the base of the extension zone, two circular regions of wall-building materials at level G and H.

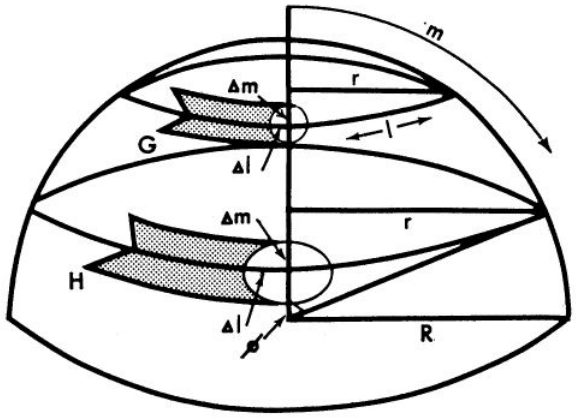

Figure 1.8: A 3-D mental picture of a generic hyphal tip proposed by [39].

Consider a small circular region at level G of wall-building materials as illustrated in Figure 1.8. As the tip apex extends, such region at level G moves downward to level H. From that it follows, tip expansion was described by the change in this region as it moves backwards from the tip and outwards from the central longitudinal axis of the hypha. If the change is equal in both planes (namely, Δm and Δl), the circular shape of such a region will result in a hemispherical shape. While, if the change in both planes varies, it will result in an elliptical shape.

The degree of anisotropy is described by the allometric coefficient, K. That

is, the coefficient K is the ratio of the relative rates of growth along the meridian and along the latitudinal directions. A relationship between the movement of the small circular region over the surface of the tip and K, is given by

$$\frac{dm}{dt} = A\frac{r^K}{R}, \tag{1.1}$$

where m is the length of the meridional arc from the apex to a point on the circle, t is time, A is a constant and r is the radius of the extension zone at the appropriate point on the tip wall. Note that radius r is 0 at the hyphal apex and equal to R at the base of the extension zone. Equation (1.1) describes that the rate of increase of distance from the tip, of the small circular region is proportional to the K^{th} power of its radial distance r from the axis.

Anisotropy was modeled by reinforcing the membrane at different points and the model was tested for different values of K. The effects of anisotropy was investigated by varying K. Subsequently, these effects were compared with predictions given by Equation (1.1) with results from a physical model of the extension zone of an expanded rubber membrane constrained at the rim.

In 1973, [3] proposed that new 'packets' of wall-building material are incorporated from membrane-bound vesicles, after softening of existing wall by the action of wall-lyric enzymes. Following that, in 1974, [38] proposed a more new direct application of Equation (1.1) related the different degrees of extensibility to the mechanism for wall growth. However, the data quoted by [38] do not show such a relationship. This represents a deficiency in the assumption of hemispherical shape.

Hypothesis of Cotangent Relationship

In 1977, [84] proposed a geometrical model of fungal hyphal growth, which is a revised model of [39] that predicted the cosine relationship for hemispherical tips,

as in the original model. However, tip eccentricity increased as observed in fungal tips and this led to a cotangent relationship between the angle subtended by a point on the extension zone wall and the specific rate of wall expansion. Furthermore, the cotangent relationship fits better with data quoted in [38] and also with experimental data on wall expansion in a number of fungi. It is concluded that provided growth is isotropic, the specific rate of wall area expansion will be more nearly proportional to the cotangent of the position angle than to its cosine [84].

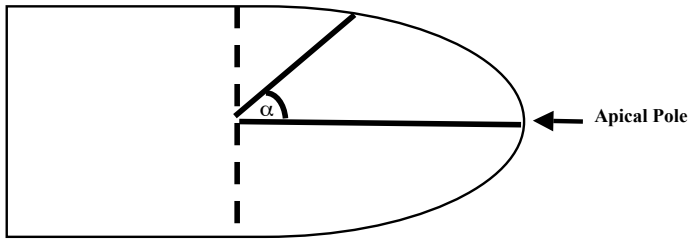

Figure 1.9: A mental picture of the medial section of a generic hyphal tip, where only half the section is considered, proposed by [84] It describes hypothesis of cotangent relationship for hyphal tip growth. The angle α, is the angle between the longitudinal axis of the filament and the point on the tip wall. Redrawn from [4].

A simple mental picture of the medial section of a generic hyphal tip, where only half the section is considered is shown in Figure 1.9. Initially, the tip shape was assumed to be arbitrary.

A 3-D mental picture of the medial section of a generic hyphal tip shown in Figure 1.10. Accordingly, parameters of interest are: A is the apex of the hypha and 0 is the point on the axis at which the growth zone ends and the hypha becomes cylindrical. A point P on the tip surface at a distance m (the length of the meridional arc from the apex to P) and a distance l (the latitudinal length from the apex to P), r is the radius of the tip at P.

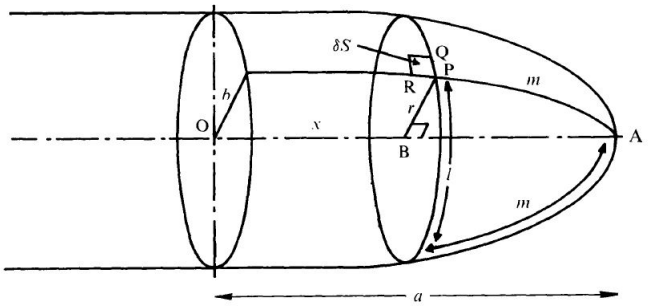

Figure 1.10: A 3-D mental picture of a generic hyphal tip proposed by [84].

To model tip expansion, consider a small area in which its growth is given by $\delta S = \delta l \delta m$, as illustrated in Figure 1.10. It was assumed that the growth of length PQ is proportional to the growth of the circumference of the tip and so, proportional to the growth of the radius r, namely, $\frac{1}{\delta l}\frac{d(\delta l)}{dt} = \frac{1}{r}\frac{dr}{dt}$, where t is time. Furthermore, for a short interval of time, an increase in PQ is $\frac{d(\delta l)}{dt}\delta t$ and so P moves a distance, $\frac{dm}{dt}(m)\delta t$, while the point R moves a distance, $\frac{dm}{dt}(m+\delta m)\delta t$. From that, it follows, the change in the length of the interval PR is $\frac{d}{dm}\left(\frac{dm}{dt}\right)\delta m \delta t$.

The allometric coefficient K was quantified as the ratio of the specific growth rates between two directions (m and l) and was given by

$$\frac{1}{\delta m}\frac{d}{dm}\left(\frac{dm}{dt}\right)\delta m \;=\; K\frac{1}{\delta l}\frac{d(\delta l)}{dt}. \tag{1.2}$$

Simplifying Equation (1.2) yields

$$\frac{1}{dm/dt}\frac{d}{dm}\left(\frac{dm}{dt}\right) \;=\; \frac{K}{r}\frac{dr}{dm}. \tag{1.3}$$

From Equation (1.3), it was interpreted that K is the ratio between the distance from the base of the extension zone to the hyphal apex (m) and the radius of the extension zone at its base (r). If K is constant and solving Equation (1.3) yields

$$\frac{dm}{dt} = Cr^K, \tag{1.4}$$

where C is a constant of integration.

The specific rate of area expansion was given by the sum of the two specific rates of linear expansion as follows

$$\left(1+\frac{1}{K}\right)\frac{d}{dm}\left(\frac{dm}{dt}\right) = \left(1+\frac{1}{K}\right)\frac{d}{dm}\left(Cr^K\right). \tag{1.5}$$

From Equation (1.5), it was supposed that the actual tip shape is closed to half ellipsoid of revolution of length a and maximum medial section radius b. Subsequently, the curve AP is a part of an ellipse, whose equation is $\frac{x^2}{a^2}+\frac{r^2}{b^2}=1$, where x is the distance from O to B, the point at which the axis is cut by a plane through P and perpendicular to the axis. Concerning $\frac{dm}{dt}$, it was assumed that the coordinates of any point of this ellipse may be expressed in terms of a single parameter, α, namely, $x = a\cos\alpha$ and $r = b\sin\alpha$. Subsequently, the arc length m is

$$m = \int_0^\alpha \left[\left(\frac{dx}{d\phi}\right)^2+\left(\frac{dr}{d\phi}\right)^2\right]^{\frac{1}{2}} d\phi, \tag{1.6}$$

$$= \int_0^\alpha \left[a^2\sin^2\phi + b^2\cos^2\phi\right]^{\frac{1}{2}} d\phi. \tag{1.7}$$

From that it follows,

$$\frac{d}{dm}\left(\frac{dm}{dt}\right) = \frac{CK(b\sin\alpha)^{K-1}b\cos\alpha}{\left[a^2\sin^2\alpha+b^2\cos^2\alpha\right]^{\frac{1}{2}}}. \tag{1.8}$$

According to [84], we have the followings:

- If in the case of isotropic growth ($K=1$), then Equation (1.8) is $\frac{d}{dm}\left(\frac{dm}{dt}\right) = \frac{Cb\cos\alpha}{\left[a^2\sin^2\alpha+b^2\cos^2\alpha\right]^{\frac{1}{2}}}$.

- If in the case of isotropic growth ($K = 1$) and if the tip is hemispherical, namely, $a = b$, then Equation (3.8) is $\frac{d}{dm}\left(\frac{dm}{dt}\right) = \frac{Cb}{a}\cos\alpha$

- If in the case of isotropic growth ($K = 1$) and if the eccentricity of the ellipsoid is large, namely, $a^2 >> b^2$, then Equation (1.8) is $\frac{d}{dm}\left(\frac{dm}{dt}\right) = \frac{Cb}{a}\cot\alpha$, where except for very small values of α.

Better qualitative fits to the observed data, including from [38], are given by cotangent rather than by cosine curves. Data quoted by [18], where longitudinal and meridional wall expansion in tips of sporangiophores of *Phycomyces blakesleeanus* was measured by microscopic observation of starch grains placed on the wall surface. While, [30] presented a set of data using microautoradiography in order to determine the rate of incorporation of radiolabelled N-acetylglucosamine, a precursor of chitin, into the extension zone wall of several fungi. Another set of data was related to variation in vesicle concentration. This may provide a measure of variation in the rate of wall synthesis if membrane-bound vesicles carry precursors to the extension zone. Accordingly, using electron micrographs of transverse medial sections of hyphal tips of *N. crassa*, data of this sort were obtained by [83]. All these indicate that cotangent relationship proving to be more realistic than the cosine relationship. However, note that there was no direct quantitative fit between predictions and experimental data.

1.2.2 Biomechanical model

A biomechanical model of fungal hyphal tip growth is constructed based on underlying specific mechanical processes experienced by a growing tip. Using such approach, it is possible to capture certain mechanistic clarification that contributes to tip growth. For example, fundamental interplay or balance between the mechanical stresses on the cell wall and vesicle deposition during tip growth. The cell wall is usually assumed to be a thin and differentially elastic membrane.

Modeling tip growth biomechnically can prove quite difficult because it involves complexity and challenges in numerical computation. In fact, it is indeed hard to tackle such models fully in three dimensions.

In 1965, [52, 53] proposed a mathematical model of tip growth of plant cells at biomechanical level. Within this framework, growth was modeled by using linear plasticity theory resulted in irreversible extension of the cell wall. That is, cell wall elongation was considered as plastic flow of the wall material under stress. The idea using plasticity theory was later applied by [64] and by [23]. One of early biomechanical models of fungal hyphal tip growth proposed mathematically is by Koch, [49]. Accordingly, a growing tip is regarded analogously as a molten glass bubble blown under constant pressure throughout the tip. In response to enzymatic and vesicle fusion activities, the surface tension is minimum at the apex and increases to maximum at the distal regions. The rate of new wall synthesis was formulated.

In recent years, fungal hyphal tip growth is modeled by using the techniques of nonlinear elasticity theory proposed by [31, 33, 34, 35, 36]. This theory enables one to follow large deformations of the cell, where the cell wall is elastic.

Surface Cell Theory

In 1981, [49] proposed a biomechanical model of fungal hyphal tip, which is based on the concept of plasticity [37]. It was thought that a tubular structure with a particular tip shape can be generated if maximum wall-building material deposition at the apex in an amount proportional to $\frac{S}{r}$, where S is slope of tip surface and r is tip radius. Also, some other necessary mechanisms are needed to maintain constant thickness of the wall provided that wall has plastic properties. Turgor pressure, P, was assumed to be constant throughout the tip. Apart from that, the composition of the tip wall is not distributed evenly due to wall-building

material deposition and enzymatic activities. As a result, there exist variation in wall elasticity. Similarly, the surface tension, T, varies throughout the hypha. That is, T was assumed to be very low at the apex, but increases towards infinity at distal regions.

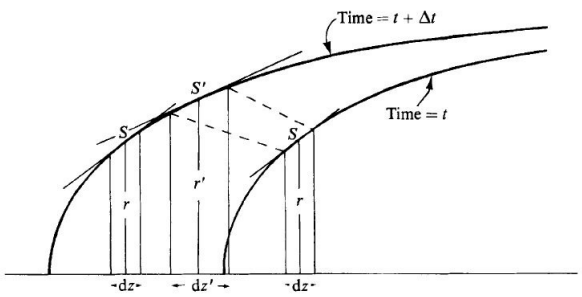

Figure 1.11: A mental picture of the medial section of a generic hyphal tip, where only half the section is considered, proposed by [49].

Tip growth is the growth that leads to a shape identical to that at a previous instant of time, but spatially displaced. A mental picture of the medial section of a generic hyphal tip, where only half the section is considered is shown in Figure 1.11. Accordingly, it shows a temporal process of hyphal tip growth, where z is tip width. Note that slope of the tip surface, S was defined by $\frac{dr}{dz}$.

To model tip expansion, it was first assumed that, at time t, a hypothetical region is labeled dz, r, and S. After wall-building material deposition, say, at a later time, $t + \Delta t$, the same region now enlarged and displaced and is labeled with dz', r' and S'. Suppose the width of the region increases proportionally to time and so it may set $dz' = (1 + a\Delta t)\, dz$, where a is the rate of axial elongation.

As stated by [49], the increase in tension-surface area (TdA) was assumed by

$$2\pi T \left((S'^2 + 1)^{\frac{1}{2}} (r')(1 + a\Delta t) - (S^2 + 1)^{\frac{1}{2}} r \right) dz. \tag{1.9}$$

While, the increase in pressure-surface volume (Pdv) was assumed by

$$\pi P \left(r'^2 (1 + a\Delta T) - r^2 \right) dz. \tag{1.10}$$

It was assumed that the growth is slow enough so that wall extension is basically an equilibrium process. From that it follows, $Pdv = TdA$, and taking $\Delta t \to 0$, $r' \to r$ and $S' \to S$ simplifies to

$$(S^2 + 1)^{\frac{1}{2}} = \frac{Pr}{2T}, \tag{1.11}$$

The reciprocal of T, $\frac{1}{T}$, may well be equated to the metabolic activity adding the new wall.

Linear plasticity theory

At the morphological level, apical growth is a common characteristic between filamentous fungi and certain types of plant. In 2003, [13], proposed a biomechanical model of plant tip growth using linear plasticity theory. This model describes a cell, that is, its cell wall as a thin elastic shell consisting cytoplasmic liquid. Its growth is driven by turgor pressure, in which, a cell undergoes non-reversible deforms of shape or size. In response to turgor pressure, two types of deformation are considered, namely, stretching and bending. These deformations are assumably balanced by proportionality relationships, generally, strain and curvature.

An overview of the mathematical description is shown in Figure 1.12. Main parameters involved are radius of curvature of the cell, R, the wall thickness, h, the elastic modulus of the wall material, E, and the turgor pressure, P, exerted on the wall. It is thought that in plant cells, growth is based on plastic deformation. The wall behaves elastically below a critical strain, a_y, and grows above by yielding to stress and so extension occurs.

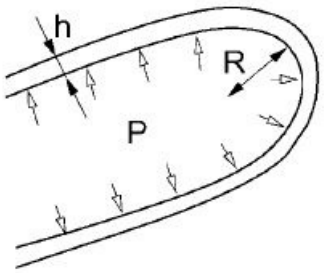

Figure 1.12: An overview of the mathematical description of the hyphal tip required for the model of [13]. Cell growth is driven by turgor pressure, P, and behaves accordingly to plastic deformation. Other parameters of interest are radius of curvature of the cell, R, wall thickness, h, and elastic modulus, E. From [13] with kind permission.

Once a new wall is synthesized, it was assumed that the cell has a 'spontaneous' radius of curvature, R_0. Also, R_0 is said to be hold in the absence of external force. It was further assumed that $R_0 \approx R$ since there is no macroscopic length scale for it. Note that the growth is considered to be slow. Slow growth occurs when the characteristic time for growth is much larger than the time needed to reach mechanical equilibrium.

Energy estimation

In this model, estimation of the cell mechanical energy is referred to stretching and bending.

The stretching energy, E_s, is proportional to the strain squared. If a cell undergoes plastic deformation, then energy is stored below the yield strain, a_y. Energy, E_s (per unit area), scales as

$$E_s \propto Eha_y^2. \tag{1.12}$$

The elastic energy (per unit area), E_b, for bending is proportional to the square

of the difference between the mean curvature and the equilibrium curvature and simplifying it gives

$$E_b \propto \frac{Eh^3}{R^2}. \tag{1.13}$$

It is important to note that in bending, the outer half of the wall (with respect to the center of curvature) is elongated while the inner half is compressed. In response to plastic flow, it is restricted to the outer wall because the cell is considered to yield only in extension. Although effective thickness is reduced in the bending energy, its order of magnitude remains the same.

The potential energy (per unit surface), E_t, corresponding to the turgor pressure is as follows

$$E_t \propto PR. \tag{1.14}$$

Characteristic Cell Size

It is generally accepted that the yield strain for most cells is much smaller than the aspect ratio, $\frac{h}{R}$. Accordingly, it is reasonable to set $a_y << \frac{h}{R}$ so that $E_s << E_b$.

It was assumed that a characteristic cell size results from the balance between bending and pressure, namely, $E_b \propto E_t$, and simplifying it gives

$$R = \alpha h \left(\frac{E}{P}\right)^{\frac{1}{3}}, \tag{1.15}$$

where α is a constant of proportionality. The best fit to the biological data gives $\alpha = 4.0$.

However one might notice a departure from Equation (1.15) at small radii and this motivates the study of $a_y >> \frac{h}{R}$ for bacteria and cochlear hair cells. In this

case, stretching balances the turgor pressure. The tension of the shell scales as the yield stress, γ, namely

$$\gamma \propto Eha_y. \tag{1.16}$$

The Laplace law requires

$$P \propto \frac{\gamma}{R}, \tag{1.17}$$

and so

$$R = \frac{\beta hE}{P}, \tag{1.18}$$

where β is proportional to a_y. The best fit to the experimental data gives $\beta = 1.0$. It has been implicitly assumed that the yield strain, a_y, varies very little for this class of cells.

Mechanical Energy

The mechanical energy, E, is the sum of the bending, stretching and pressure energies and is defined by

$$E = \frac{1}{2}k\int (c - c_0)^2 dA + \frac{1}{2}E\int \sigma_{ij}a_{ij}dA - PV. \tag{1.19}$$

where it is computed over the cell wall. From Equation (1.19), c is the wall mean curvature, c_o is its spontaneous curvature, σ_{ij} is the stress tensor, a_{ij} is the strain tensor, V is the cell volume, k is the bending modulus defined by $\frac{Eh^2}{12(1-v^2)}$, where v is the *Poisson* ratio of the wall material. Usually, for most biological materials (nearly incompressible), $v = 0.5$ will be used for numerical computation.

The stress and strain tensors are related by $\sigma_{ij} = \frac{Eh}{1-v^2}[(1-v)a_{ij} + va_{kk}\delta_{ij}]$, where δ_{ij} is the identity tensor.

The case of bending balances turgor pressure was considered, where the stretching is neglected. For the sake of simplicity, it was assumed that c_0 is constant along the wall. The simple shape for the wall is a sphere of radius R. The equilibrium condition is given by

$$\frac{PR^3}{k} = c_0R(c_0R - 2), \tag{1.20}$$

so that $c_0 > \frac{2}{R}$. One would expect c_0 to relax towards the actual curvature, $\frac{2}{R}$, and c_0 to assume the smallest possible value. Solving Equation (1.20) for c_0 yields $c_0 = f(R)$, whose minimum is reached at a radius R such that $\frac{PR^3}{k} = 8$. The maximum R_0 which a spherical cell would reach corresponds to a prefactor $\alpha = 0.96$ provided that $v = 0.5$ in Equation (1.15).

It is thought that vesicles are first unstable to prolate ellipsoid shapes provided that c_0 is large enough. Recall that the wall growth rate increases with the stress which is proportional to the curvature. If the cell adopts the shape of a prolate ellipsoid, then the growth rate is larger at the tip with maximum curvature and so the cell will be elongated. Most cells which satisfy Equation (1.15) grow in tubular forms (capped cylinders).

Shape Equation

The hyphal tip surface is axisymmetric with respect to the z-axis (horizontal axis, which is also growth axis) and matches onto a cylinder (possibly for $z \to \infty$) of unknown R. Let ψ be the angle of the surface normal to the z-axis and r is the radial coordinate. The curvature is as follows

$$\frac{d(\sin\psi)}{dr} + \frac{\sin\psi}{r}. \tag{1.21}$$

It was assumed that the curvature is bounded, then we have [87] (also can be found in [45])

$$\psi'' = \frac{1}{2}\tan\psi(\psi')^2 - \frac{1}{r}\psi' + \frac{1}{r^2}\tan\psi \qquad (1.22)$$

$$-\frac{PR^3}{k}\frac{r}{2\cos^3\psi} + \frac{\sin\psi}{2\cos^3\psi}\left(\frac{\sin\psi}{r} - c_0R\right)^2.$$

Equation (1.22) Referring to Equation (1.22), the primes are subjected to derivatives with respect to r and lengths are nondimensionalized by the radius R. Boundary conditions of Equation (1.22) are $\psi(0) = 0$ (at the tip) and $\psi(1) = \frac{\pi}{2}$ (at the cylinder), where the curvature is 1. The unknown spontaneous curvature, c_0, is equal to the curvature at the tip is $\psi'(0) = \frac{c_0R}{2}$ and $\frac{d(\sin\psi)}{dr} = 0$ (for $r = 1$).

Since c_0R and $\frac{PR^3}{k}$ are unknown, two extra boundary conditions are required. A numerical shooting leads to the solution represented figuratively by Figure 1.13, where $z(r)$ is obtained by integration:

$$\frac{dz}{dr} = -\tan\psi. \qquad (1.23)$$

From the numerical computation, it was found that $c_0 = \frac{2.34}{R}$ and $\frac{PR^3}{k} = 1.79$, which is in agreement with the scaling $c_0 \approx \frac{1}{R}$ used in the analysis. Using a reasonable *Poisson* ratio, $v = 0.5$, one gets as a prefactor of Equation (1.15), $\alpha = 0.58$. Moreover, the resulting cylindrical shapes proposed by [13] are stable as $c_0R \geq 1$ [88]. Based on [15], sufficiently negative spontaneous curvature may transform a cylinder into a tapelike form.

This model proposes that when bending balances turgor pressure, tip growth occurs. However, there are a number of drawbacks in this model. For example, the spontaneous curvature of the wall is generally not constant and its temporal evolution should be considered. Also, anisotropies in growth are neglected.

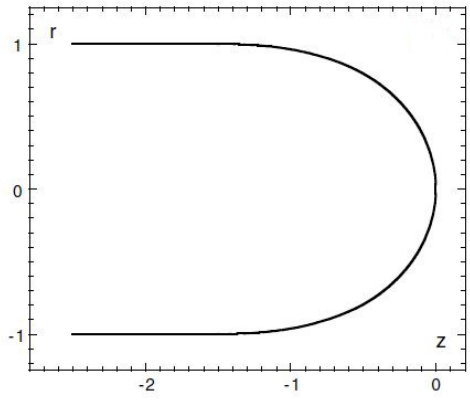

Figure 1.13: An overview of 2-D shape, $z(r)$, of a tip growing cell according to Equations (1.22) and (1.23). The surface is axisymmetric with respect to the z-axis and matches onto a cylinder. From [13] with kind permission.

1.2.3 Vesicle-based model

Fungal tip growth can be modeled mathematically through intracellular process. Namely, it suggests that the Spitzenkorper is a 'vesicle supply centre', VSC. This model predicts that the VSC releases exocytic vesicles in all directions while it moves forward with a constant speed, thereby generating an exocytosis gradient that shapes the hypha. Up to now, there are only three mathematical models of this kind. Generally, in all existing vesicle-based models, assumptions are mainly motivated by incorporation rate of vesicles into the cell wall.

The first attempt in proposing a 2-D vesicle-based model was proposed by [7]. It was assumed that once released isotropically from the VSC, vesicles are to be transported ballistically towards the cell boundary. Note that this work is divided by two main sections; mathematical construction and computer simulation of tip growth. The first section is discussed in Chapter 2.

The 2-D VSC model has an obvious drawback, namely, it cannot capture the three-dimensional aspects of growth. The requirement of 3-D model necessitates further research in which, at least, the more realistic 3-D model is assumed.

In 2001, [29], has extended their 2-D vesicle-based model to three-dimensional mathematical formulations using the same mechanism of vesicle delivery. However, the three-dimensional derivation led to an indetermination solution. In 2006, [81], proposed a more detailed 3-D model, which is generally based on [29]. This model describes that vesicles diffuse freely before being absorbed at the cell boundary. Furthermore, it also described and formulated processes like vesicle fusion and vesicle absorption.

Ballistic vesicles

A 3-D model of hyphal morphogenesis according to the 2-D vesicle-based model construction was proposed by [29]. Transition from 2- to 3-D is generally done by rotating the 2-D shape along its longitudinal axis. However, it involves much more complex thought. Its three-dimensional formulation has an indetermination solution. Following that, it is required to describe point trajectories of wall expansion. In [6], it was experimentally computed patterns of wall expansion (isometric, orthogonal and rotational) on the cell surface of a growing hypha. Subsequently, the degree of anisotropy for wall expansion can be captured. It is shown that the 3-D tip shape is essentially similar to 2-D's for orthogonal wall expansion.

The hyphal tip is symmetric about the y-axis (growth axis), with R representing the radius of the hyphal tube, as illustrated by Figure 1.14. Growth is described by a translation of the tip along the y-axis and so the shape of its growing tip is self-similar. The VSC moves with a constant speed, v, in which it is initially situated at $(0, 0, 0)$. Once released isotropically from the VSC, vesicles are delivered ballistically towards the apex and so at time $t \neq 0$, the VSC is at $(0, vt, 0)$.

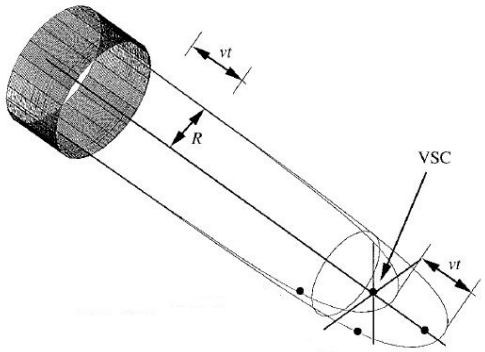

Figure 1.14: An overview of the mathematical description of the hyphal tip required for the model of [29]. The hyphal tip is modeled as being axially symmetric about the y-axis, with R as the radius of hyphal tube. The VSC moves with a constant speed, v. At time $t = 0$, the VSC is situated at $(0, 0, 0)$, while, at time $t \neq 0$ is at $(0, vt, 0)$. From [29] with kind permission.

Transition from 2- to 3-D

Generally, the 2-D tip shape is represented by a 2-D curve, $\gamma(t)$. This curve is expressed parametrically as $(x(t, s), y(t, s))$, where s is an angle between, l, namely, ballistic line from the VSC to a point on the curve and the positive y-axis called ray. Note that l intersects the curve exactly once in the point of the curve.

At time $t = 0$, the 3-D tip is given by rotating the 2-D curve, γ_0, with $(x_0(s), y_0(s))$ about the y-axis defined on $(-S, S)$. While, at time $t \neq 0$, the 3-D tip is given by rotating the 2-D curve, $\gamma(t)$, about the y-axis, with $(x(t, s), y(t, s))$. Subsequently, the growth can be described by $(x(t, s), y(t, s)) = (x_0(s), y_0(s)+vt)$.

Surface area

Note that new surface (cell wall) is inserted while the thickness of the wall remains unchanged. The surface area added at time interval, Δt, is given by $2\pi Rv\Delta t$. The amount of surface area added per time unit, N_3, is $2\pi Rv$. Furthermore, the amount of surface area dispersed per time unit is given by $N_3(\alpha) = \mu(\alpha)N_3 =$

$2\pi Rv\mu(\alpha)$, where $\mu(\alpha)$ is an angular distribution function (or vesicle distribution function) and α is a spatial angle to the positive y-axis.

Point trajectories and Anisotropy

Point trajectories of wall expansion can be described by tracing the movement of markers on the cell surface. That is, observing a point on a growing tip at t.

Let P be a point on the cell surface. While, let $\sigma(t,s)$ denote the polar angle under which P is observed from the VSC after t times units. The functions $x_0(s)$ and $y_0(s)$ with trajectories of $P(t)$ described by $x_p(t) = x(t,\sigma(t,s))$ and $y_p(t) = y(t,\sigma(t,s))$. The following is differential equations relating the shape of a tube with trajectories of a point P [29]:

$$\frac{dx}{dt}(t,\sigma(t,s)) = \frac{N_3}{2\pi}\frac{\mu(\sigma(t,s))y_0'(\sigma(t,s))}{x_0(\sigma(t,s))\sqrt{x_0'(\sigma(t,s))^2 + y_0'(\sigma(t,s))^2}}, \tag{1.24}$$

$$\frac{dy}{dt}(t,\sigma(t,s)) = v + \frac{N_3}{2\pi}\frac{\mu(\sigma(t,s))y_0'(\sigma(t,s))}{x_0(\sigma(t,s))\sqrt{x_0'(\sigma(t,s))^2 + y_0'(\sigma(t,s))^2}}, \tag{1.25}$$

$$\frac{\partial\sigma}{\partial t}(t,s) = \frac{N_3}{2\pi}\frac{\mu(\sigma(t,s))}{x_0(\sigma(t,s))\sqrt{x_0'(\sigma(t,s))^2 + y_0'(\sigma(t,s))^2}}. \tag{1.26}$$

Equations (1.24)-(1.26) can be derived by looking at a point $P(t)$ on the hyphoid at time t. Let s be the polar angle under which P is observed from the VSC at time $t = 0$, and let $\sigma(t,s)$ denote the polar angle under which P is observed from the VSC after t time units. Then the parameter function satisfies: $\sigma(0,s) = s$ and $P(t) = (x(t,\sigma(t,s)), y(t,\sigma(t,s))) = (x_0(t,\sigma(t,s)), y_0(t,\sigma(t,s)) + vt)$. The goal is to find a differential equation for $x(t,\sigma(t,s))$ and $y(t,\sigma(t,s))$. Let $s_0 = \sigma(t_0,s)$, then s_0 is the angle between the positive y-axis and the ray starting at the position of the VSC and passing through the point $P(t_0)$ hence, $\tan s_0 = \frac{x(t_0,s_0)}{y(t_0,s_0)}$. Consider the dome at the tip that is defined by a planar cut orthogonal to the axis of growth and passing through the point $(x(t,s), y(t,s), 0)$. The increase of surface area F of the hyphoid dome is

$$\frac{dF}{dt}(t_0) \;=\; 2\pi x_0(s_0)\sqrt{\left(\frac{dx_0(s_0)}{du}\right)^2+\left(\frac{dy_0(s_0}{du}\right)^2}\frac{\partial\sigma}{\partial t}(t_0,s).$$

The increase of surface area F of the hyphoid dome in a short time Δt is equal to the amount of surface area that is dispersed into the spatial angle obtained by rotating the ray starting at the origin and going through P about the positive y-axis, namely,

$$\frac{dF}{dt}(t_0) \;=\; N_3\mu(s_0).$$

Subsequently, $2\pi x_0(s_0)\sqrt{\left(\frac{dx_0(s_0)}{du}\right)^2+\left(\frac{dy_0(s_0}{du}\right)^2}\frac{\partial\sigma}{\partial t}(t_0,s) = N_3\mu(s_0)$ and this gives Equation (1.24), where the chain rule implies $\frac{dx}{dt}(t,\sigma(t,s)) = x_0'(s_0)\frac{\partial\sigma}{\partial t}(t_0,s)$. Similarly for Equations (1.25) and (1.26) $\frac{dy}{dt}(t,\sigma(t,s))$ and $\frac{\partial\sigma}{\partial t}(t,s)$, respectively.

The following relates the coefficient of anisotropy, q, with the shape, x_0 of the hyphal tube

$$q(s_0) \;=\; \frac{x_0\mu'-\mu x_0'}{\mu x_0'}. \tag{1.27}$$

Equations (1.24)-(1.26) are insufficient to determine 3-D shape because they have infinitely many solutions. Equations (1.26) and (1.27) relating point trajectories, coefficient of anisotropy and shape. By fixing any one of these three parameters, the other two would be determined. Accordingly, three different solutions were obtained by fixing the coefficient of anisotropy (isometric, orthogonal and rotational).

Result

Based on mapping the movement of internal and external surface markers, that the surface of a tip-growing hypha expands orthogonally [6]. On this basis, the

equation for an orthogonal hyphoid affords the best idealized description of the shape of a hypha in 3-D.

Diffusive vesicles

In 2006, [81], proposed a 3-D vesicle-based model of fungal hyphal tip growth. It is an extensive description of hypothesis given by [29]. The key features that define this model are the assumptions on vesicle delivery and vesicle fusion with the cell membrane.

It was assumed that vesicles diffuse spontaneously, spatially and freely from the VSC to the hyphal wall. To justify such assumption, perhaps it is obvious that the cytoplasm of a cell is more viscous than water and crowded. The additional effect of drag exerted by a possible flow in the cytoplasm (advection) is neglected. Moreover, in absence of external forces, the submicrometer-sized vesicles undergo essentially thermal motion and so move random walk-like trajectories. Note that a vesicle size was assumed to be around $50nm$ [55]. The diffusivity constant, D, was approximately assumed to be around $1\mu m^2/s$ and so vesicles travel from the VSC to the cell membrane in a few seconds.

Vesicle fusion is the merging of a vesicle with other vesicles or a part of a cell membrane. While, exocytosis requires that the lipid membrane of a vesicle to open up, which is then followed by vesicle fusion. Within the process of exocytosis, a considerable energy barrier has to be overcome and this determines the time scale for exocytosis. It was further assumed that the vesicle absorption rate, μ (or the vesicle flux, Φ), is proportional to the vesicle concentration, c, at the cell boundary. From that it follows, a proportionality constant, k, refers to the reaction constant for vesicle fusion.

An overview of the mathematical description of the hyphal tip and the variables required for this model is shown in Figure 1.15, where, R, is the radius of

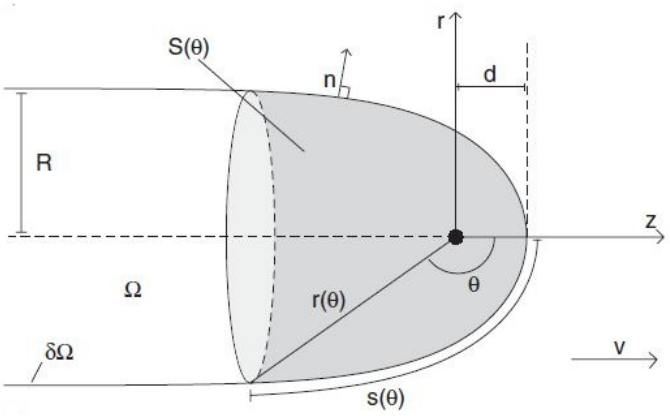

Figure 1.15: An overview of the mathematical description of the hyphal tip and the variables required for the model of [81]. The hyphal tip is modeled as being axially symmetric, with reference direction given as $\theta = 0$. The domain Ω represents the inside of the hypha whilst $\partial\Omega$ represents the hyphal wall/cell membrane complex. $S(\theta)$ is the cap that is formed by the incorporation of vesicles into the cell wall and whose formation and geometry is determined by the model. From [81] with kind permission.

the cell at its base. The cylindrical coordinates and the spherical coordinates are used to model the axial symmetry of the growing tip. It was set that the growth is in the positive z-direction in cylindrical coordinates and in the direction with $\theta = 0$ in spherical coordinates in which the cell extends at a speed v. The origin of both coordinate systems is chosen to coincide with the VSC location.

In this model, the expansion of the cell wall is only motivated by the vesicle deposition into the wall and so the associated area growth is considered. Following that, the absorption profile, $\mu(\theta)$, was introduced, which measures the relative amount of cell area deposited per unit time into the cap $S(\theta)$ at angle θ. The profile, $\mu(\theta)$, is a monotonically increasing dimensionless function. That is, at the tip when $\theta = 0$, $\mu = 0$ (minimum value) and towards the base at the cell when $\theta = \pi$, $\mu = 1$ (maximum value). Similarly, the vesicle flux, $\Phi(\theta)$, refers to the area incorporated into the cap $S(\theta)$. The profile, $\mu(\theta)$, was then assumed as follows

$$\mu(\theta) = \frac{1}{\dot{A}} \int_{S(\theta)} \Phi ds, \tag{1.28}$$

where $\dot{A}$ is the total rate of wall area growth and is defined by $\dot{A} = 2\pi Rv$. Also, $\dot{A}$ is directly proportional to the total integrated vesicle flux.

The diffusive equation is written as

$$\frac{\partial c(r,t)}{\partial t} = D\nabla^2 c(r,t) + \tilde{S}(r,t). \tag{1.29}$$

From Equation (1.29), vesicle concentration, $c(r,t)$, is described by the amount of surface area they contain per unit volume. While, $\tilde{S}(r,t)$ is the VSC in the origin expressed by $\tilde{S}(r,t) = 2\pi Rv\delta(r)$. The growth was assumed to be stationary and so stationary solutions of Equation (1.29) are of interest. Also, for simplicity purpose, the 're-scaled' concentration was given by

$$\varphi(r) = \frac{D}{2\pi Rv} c(r), \tag{1.30}$$

and substituting this in Equation (1.29) and simplifying it yields

$$\nabla^2 \varphi(r) = -\delta(r), \tag{1.31}$$

which is the *Poisson* equation. It is commonly used to describe the situation of electrostatics for a system with a point charge in the origin.

The general solution, $\varphi(r)$, of Equation (1.31) depends on the boundary condition. In this case, a Von Neumann type boundary is given as follows

$$-D\hat{n}(\phi,s) \cdot \nabla c(r(\phi,s)) = kc(r(\phi,s)). \tag{1.32}$$

The left-hand side of (1.32) describes the vesicle flux through the cell surface and the right-hand side is determined by the imperfect vesicle absorption. Substituting Equation (1.28) in $\Phi = kc$ yields $\Phi(s) = 2\pi R v \frac{k}{D}\varphi(s)$. The constant k has a certain value throughout the cell and each value will give a different solution to the diffusion equation.

The general solution, $\varphi(r)$, of Equation (1.31) is the sum of the particular, $\varphi_0(r)$, and the homogeneous, $\varphi_h(r)$, solutions. The well-known particular solution, $\varphi_0(r)$, of Equation (1.31) with the boundary conditions $\lim_{r\to\infty}\varphi(r) = 0$ is $\varphi_0(r) = \frac{1}{4\pi|r|}$. While, $\varphi_h(r)$ is given by the Laplace equation, namely, $\nabla^2\varphi_h(r) = 0$. However, the boundary conditions for $\varphi_h(r)$ are numerically very complicated and it is impossible to find the solution of the Laplace equation for arbitrary boundary conditions.

The solution of the *Laplace* equation for arbitrary boundary conditions has to be approximated using the fundamental solution method. This is done in the following way: First, a set of source rings is placed outside of the surface. These are designed to affect the solution on the boundary without violating the Laplace equation inside the surface. In analogy with electrostatics, each source ring has its own charge. Second, an equal number of response rings is located on the surface itself. The response rings are placed on the surface with equal distance, d_r, and the corresponding source rings at a distance, d_s, in the direction perpendicular to the surface.

The model of [81] shows that by tuning the incorporation rate of vesicles at the cell boundary, the cell can tune the sharpness of the tip shape. Furthermore, the different apex-VSC distances can also be obtained. However, the spectrum of different shapes that can be described this way cannot completely explain all the observed ones. In particular, the sharper and the blunter ones are not addressed. It should also be pointed out that the shape per se is perhaps not the most

sensitive test for the success of a model, as potentially many models could lead to the same shape, and the shapes found under different conditions are fairly similar.

1.3 Summary

Filamentous fungi have extraordinary functional intracellular and abilities complexity. Studies of fungal hyphal tip growth has long been done. However, the growth mechanism remains to be fully explained.

Mathematical modeling has contributed a significant role in the development of understanding fungal hyphal tip growth. Many different approaches have been taken, but these can be grouped in two main classes; geometrical and biomechanical.

The geometrical models describe growth through a relationship between the increase in wall area of a growing tip and deposition of wall-building materials. Although these models can often be at least partially solved analytically, they cannot capture mechanistic description of a propagating tip. The biomechanical models of fungal hyphal tip growth are based on underlying mechanical processes experienced by a growing tip. However, these models are quite difficult as they involve complexity and challenges in numerical computation. In the following chapters, we examine both geometrical and biomechanical models.

We first consider a geometrical model for the role of the Spitzenkorper in the tip growth proposed by [7]. However, [50] pointed out a number of problems with the mathematical derivation in this model. As an attempt to revise the derivation, we suggest a relationship between arc length of a growing tip, deposition of wall-building materials and tip curvature.

We then study two types of geometrical models proposed by [31]. The first

type considers a relationship between the longitudinal tip curvature and deposition of wall-building materials. By employing such relationship, we give generalized formulae for the tip shape and this enables us to examine localization of deposition of wall-building materials. The second type describes a relationship between longitudinal and latitudinal tip curvatures and deposition of wall-building materials. Following that, we suggest a new formulation that relates deposition of wall-building and tip curvatures.

Finally, we are interested with a biomechanical model proposed by [36]. The model suggests that deposition of wall-building materials is proportional to turgor pressure. We examine the effects of varying arc length of the stretchable region on geometry of tip shape and the effective pressure profile. Also, we observe the orthogonal growth as proposed by [67] (wall expansion is normal at right angles to the tip) occurs during early growth phases of a germ tube).

Chapter 2

Geometrical Model

2.1 Introduction

The mathematical modeling of hyphal tip growth of fungal hyphae can be described in terms of geometry. From geometrical point of view, growth is modeled by balancing the increase in tip wall area of a growing tip with the wall-building material deposition. Here we examine geometrical models proposed by [7] and [31]. The former will be discussed first in the following section.

2.2 Hyphoid Model

A geometrical model for the role of the Spitzenkorper in tip growth was proposed by [7]. In this model, the Spitzenkorper is identified as the Vesicle Supply Center VSC. This model predicts that the VSC releases exocytic vesicles in all directions while it moves forward. In response to that, an exocytosis gradient is generated that shapes the hypha. Such gradient is hypothesized to be key for the shape formation of apical dome known as the hyhpoid curve, C. A geometrical equation called hyphoid equation was derived to describe C. This equation relates deposition of exocytic vesicles per unit time, n with speed of the VSC, U_0. Curves

predicted by the hyphoid equation were found to fit microscopic medial section profiles of several real hyphae.

A number of problems with the derivation of hyphoid equation were pointed out by [50]. However, the hyphoid equation does produce a remarkably good fit to images of hyphal tips. This motivates us to revise its derivation.

2.2.1 Model Construction

The medial section, C of a generic hyphal tip is shown in Figure 2.1. Only half the section is considered. A growing tip is modeled by assuming it is axisymmetric about the y-axis.

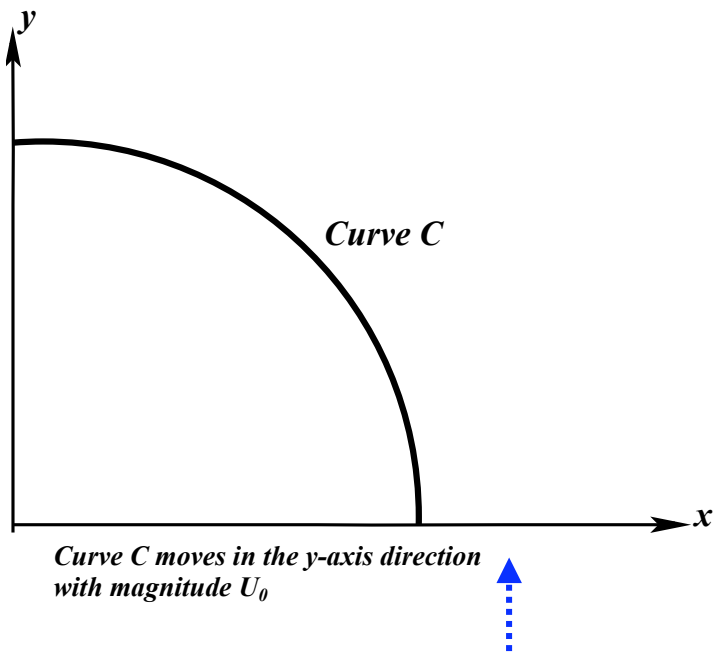

Figure 2.1: The medial section, C, of a generic hyphal tip. Only half the section is considered for clarity. The tip is based on Cartesian coordinates as given by Equation (2.1). Redrawn from [7].

The curve C can be described by

$$y = C(x,t). \tag{2.1}$$

While releasing exocytic vesicles equally in all directions at given time t, the VSC moves forward along the y-axis with magnitude U_0 (units of hyphal length per unit of time). A 3-D representation of hyphal filament geometry from half of its medial section can be obtained by rotating the profile C about the y-axis through an angle of 2π. Assuming that the profile C is translated in the y-direction with speed U_0, then

$$C(x,t) = C(x,0) + U_0 t. \tag{2.2}$$

From that it follows Equation (2.2) describes the translation of a self-similar shape. Then [7] transfromed Equation (2.1) in terms of polar coordinate system as follows

$$(x,y) \quad = \quad (r\sin\beta, r\cos\beta), \tag{2.3}$$

where r is radius and β is the angle to the y-axis. A description of Equation (2.2) in terms of polar coordinates is done first by differentiating both sides of Equation (2.3), which yields $(dx, dy) = (\sin\beta dr + r\cos\beta d\beta, \cos\beta dr - r\sin\beta d\beta)$. Since $y' = \frac{dy}{dx}$ and so $y' = \frac{\cos\beta\frac{dr}{d\beta} - r\sin\beta}{\sin\beta\frac{dr}{d\beta} + r\cos\beta}$.

Finally, let $r = \rho(\beta, t)$ be the equation for Equation (2.1). A figurative representation of C based on $r = \rho(\beta, t)$ is shown in Figure 2.2.

Then by directly substituting Equation (2.3) into Equation (2.1) leads to

$$\rho(\beta,t)\cos\beta \quad = \quad C(\rho(\beta,t)\sin\beta, t). \tag{2.4}$$

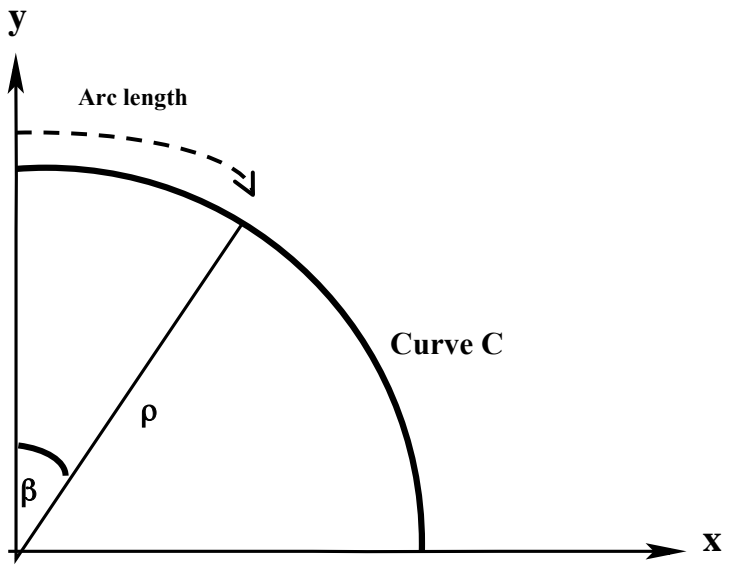

Figure 2.2: The medial section, C, of a generic hyphal tip. Only half the section is considered. The tip is described in terms of $r = \rho(\beta, t)$.

Note that [7] claimed Equation (2.4) is equivalent to

$$\rho(\beta, t)\cos\beta \quad = \quad C(\rho(\beta, t)\sin\beta, 0) + U_0 t. \tag{2.5}$$

However Equation (2.5) is incorrect. In fact, $C(x, 0) = C(\rho(\beta, 0)\sin\beta, 0)$ and so Equation (2.5) should read as

$$\rho(\beta, t)\cos\beta \quad = \quad C(\rho(\beta, 0)\sin\beta, 0) + U_0 t. \tag{2.6}$$

Differentiating both sides of Equation (2.6) with respect t yields

$$\rho_t(\beta, t)\cos\beta \quad = \quad U_0. \tag{2.7}$$

This statement is correct but simply repeats the original assumption that the curve is translated in the y-direction with the speed U_0.

2.2.2 Revised Derivation

The subsequent analysis in [7] is therefore redundant. Despite the erroneous derivation, the hyphoid shape "seems" right. We wondered then, if an alternative derivation for the hyphoid equation could be found.

2.2.3 Rate of radius ρ_t

A temporal process of C based on $r = \rho(\beta, t)$ is described in Figure 2.3, where the angle β is fixed throughout. The arc length s is measured to the y-axis and is defined by $s = \rho(\beta, t)\beta$. From that it follows,

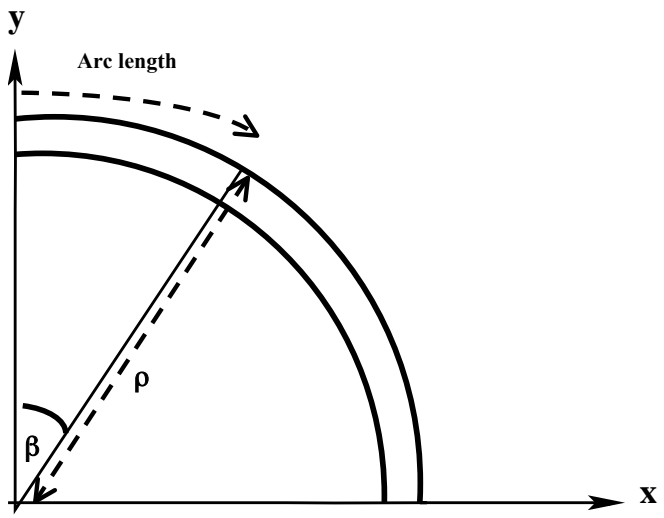

Figure 2.3: A temporal process of the medial section, C, of a generic hyphal tip. Only half the section is considered. The tip is described in terms of $r = \rho(\beta, t)$.

$$\Delta s = = s_{t+\Delta t} - s_t, \tag{2.8}$$

$$= (\rho(\beta, t + \Delta t) - \rho(\beta, t))\beta. \tag{2.9}$$

In [7], it claimed that the right-hand side of Equation (2.9) is the area added to the tip surface in time Δt in angular region $\Delta\beta$, which is incorrect [50]. Dividing both sides of Equation (2.9) with Δt yields

$$\frac{\Delta s}{\Delta t} = \frac{(\rho(\beta, t+\Delta t) - \rho(\beta, t))}{\Delta t}\beta. \tag{2.10}$$

Then taking the limit as $\Delta t \to 0$ for both sides of Equation (2.10) gives $s_t = \rho_t(\beta, t)\beta$. So we conclude that

$$\frac{1}{\beta}s_t = \rho_t(\beta, t). \tag{2.11}$$

Equation (2.11) is interpreted as the change in arc length s per unit angle β is balanced by the change in radius ρ at given time t.

2.2.4 Hyphoid Equation

A new assumption is introduced, namely,

$$\frac{1}{\beta}s_t \propto n, \tag{2.12}$$

where n denotes deposition of exocytic vesicles. Assumption in Equation (2.12) suggests that maximum deposition takes place when the change in s per unit β is maximum and vice versa. Further, n is assumed such that

$$n \propto \hat{\kappa}, \tag{2.13}$$

where $\hat{\kappa}$ may be considered as the "pseudo-curvature" and is defined by

$$\hat{\kappa} = \frac{1}{\rho(\beta, t)}. \tag{2.14}$$

The variable $\rho(\beta, t)$ in Equation (2.14) is the distance from the shape-organising center to the curve C called radius of "pseudo-curvature". At behind the tip, this

radius is infinity giving its curvature zero. This assumption tells that maximum deposition lies within a region of maximum curvature. Based on these two assumptions, maximum deposition is modeled at apical dome, where the change in s (or equivalently ρ) is maximum as well. From Equations (2.12)-(2.14), it follows

$$\rho_t(\beta,t)\rho(\beta,t) \;=\; N, \tag{2.15}$$

where N is the constant of proportionality. Based on Equation (2.7), Equation (2.15) then becomes

$$\frac{U_0}{\cos\beta}\rho(\beta,t) \;=\; N. \tag{2.16}$$

From Equation (2.16), we proceed with the followings:

$$\frac{1}{\cos\beta}\rho(\beta,t) \;=\; \frac{N}{U_0}, \tag{2.17}$$

$$\rho(\beta,t) \;=\; \frac{N}{U_0}\cos\beta. \tag{2.18}$$

Assume β is very small, then $\sin\beta = \beta$ (or $\lim_{\beta\to 0}\frac{\sin\beta}{\beta} = 1$) and so Equation (2.18) becomes

$$\rho(\beta,t) \;=\; \frac{N}{U_0}\frac{\beta}{\sin\beta}. \tag{2.19}$$

In other words,

$$\frac{N}{U_0}\cos\beta \;=\; \frac{N}{U_0}\frac{\beta}{\sin\beta}, \tag{2.20}$$

where $|\beta| < 1$ when deposition of wall-building materials is maximum at the apex. Multiplying both sides of Equation (2.19) with $\cos\beta$ yields

$$\rho(\beta, t)\cos\beta \;=\; \frac{N}{U_0}\beta\cot\beta, \tag{2.21}$$

which results in

$$y \;=\; \frac{N}{U_0}\beta\cot\beta. \tag{2.22}$$

Next, referring to Equation (2.19), β is given by

$$\beta \;=\; x\frac{U_0}{N}. \tag{2.23}$$

Substituting Equation (2.23) into Equation (2.22) yields

$$y \;=\; x\cot\left(\frac{U_0}{N}x\right), \tag{2.24}$$

which is the hyphoid equation. Positioning of the VSC is such that the distance between the VSC and the cell wall is minimized at the apex. Equivalently, the right-hand side of Equation (2.24) is

$$\frac{x\cos\left(\frac{U_0 x}{N}\right)}{\sin\left(\frac{U_0 x}{N}\right)},$$

and so obviously it is undefined when its denominator equals to 0. A plot of Equation (2.24) for $-\pi < x < \pi$, $\frac{U_0}{N} = 0.2$ (i.e $\beta = \frac{U_0}{N}x = 0.2\pi < 1$) shown in Figure 2.4. Equation (2.24), where vertical asymptotes are $x = \pm\pi$. Since, $\lim_{x\to\pm\infty} y = \pm\infty$, then Equation (2.24) does not have horizontal asymptote.

From Equation (2.24), different predicted geometric tip shapes can be obtained by varying U_0 where N is a constant. Varying U_0 results in either less-rounded edge tip or more-rounded edge tip as illustrated in Figure 2.5.

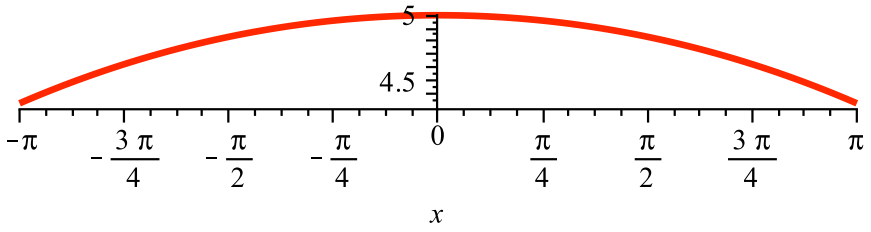

Figure 2.4: A plot of hyphoid curve, $y = x\cot\left(\frac{U_0}{N}x\right)$ for $-\pi < x < \pi$, $\frac{U_0}{N} = 0.2$, which is given in Equation (2.24).

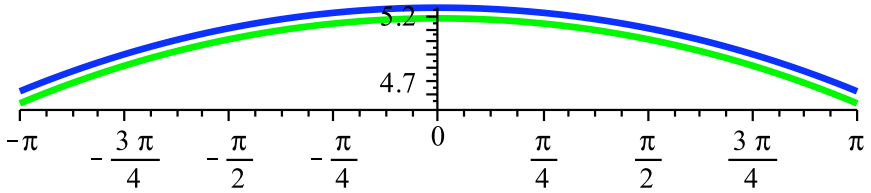

Figure 2.5: Plots of hyphoid curves, $y = x\cot\left(\frac{U_0}{N}x\right)$ for $-\pi < x < \pi$, $\frac{U_0}{N} = 0.19$ (blue), $\frac{U_0}{N} = 0.193$ (green), based on Equation (2.24).

Note that, although, say, choosing $\frac{U_0}{N} = 0.85$ does produce the hyphoid curve, it does not agree with the assumption of β because $\beta = \frac{U_0}{N}x = 0.85\pi$ is greater than 1.

2.2.5 Distance *d*

As proposed by [7], the distance between the origin location of VSC and the tip is denoted by d. Mathematically, the distance d is actually the y-intercept of the hyphoid equation, approximately defined by $\frac{N}{U_0}$. Parameter d is the position of the Spitzenkorper in the apical dome [7]. As stated by [7], d is directly proportional to hyphal diameter. The hyphoid curves based on our revised derivation of the hyphoid equation produce broader hyphal tips because values of d indicate that the Spitzenkorper is not extremely closed to the apical wall. There is no mathematical derivation of d given and so we discuss it here. Obviously, the

y-intercept represents all the points on the plane where the x value is zero and so we first do as follows.

Rewriting the right-hand side of Equation (2.24) yields

$$\frac{\cot\left(\frac{U_0}{N}x\right)}{\frac{1}{x}}, \tag{2.25}$$

where Equation (2.25) tends to $\frac{+\infty}{+\infty}$ as x tends 0. Using L'Hopital's rule for Equation (2.25) and simplifying its derivative then gives

$$\frac{U_0}{N}\left(\frac{x}{\sin\left(\frac{U_0 x}{N}\right)}\right)^2. \tag{2.26}$$

From Equation (2.26), let $\frac{U_0 x}{N} = \hat{x}$ and from that it follows

$$\frac{N}{U_0}\left(\frac{\hat{x}}{\sin\hat{x}}\right)^2. \tag{2.27}$$

Subsequently, referring to Equation (2.27), $\lim_{\hat{x}\to 0^-}\left(\frac{\hat{x}}{\sin\hat{x}}\right) = 1 = \lim_{\hat{x}\to 0^+}\left(\frac{\hat{x}}{\sin\hat{x}}\right)$ and so based on the squeezing theorem, $\lim_{\hat{x}\to 0}\left(\frac{\hat{x}}{\sin\hat{x}}\right) = 1$. From that it follows Equation (2.27) tends to $\frac{N}{U_0}$ as x tends to 0. This proves that the y-intercept of hyphoid equation is $\frac{N}{U_0}$. Obviously, the distance d is inversely proportional to U_0.

2.3 Curve Dynamic

In [31], two geometrical models were proposed based on curve dynamical assumptions, which relate curvatures of the hyphal tip with its surface growth.

The first model considers the longitudinal curvature, κ. In this model, κ is associated to $n(s,t)$, the function used to model the wall-building material deposition. The relationship of κ and $n(s,t)$ is assumed to be of the form $n(s,t) \propto \kappa^p$, where $p \geq 1$. It was shown that $p = 1$ results in the irrelevant solution. The

choice of $p = 2$ was chosen as it provides a closed form solution and an explicit form of the tip shape.

The second model is described by mean curvature, K_m, and *Gaussian* curvature, K_g, where $K_m = \kappa + k$ and $K_g = \kappa k$. A relationship between the function used to model the wall-building material deposition, $n(s,t)$, and the curvatures is assumed to be $n(s,t) = K_g N(K_m, K_g)$. Choice $N \equiv 1$ is made specific, which yields $n(s,t) \propto K_g$. This choice satisfies the need that growth should be largest at the tip and zero along distal region of the tip. An explicit form of the tip shape and closed form of its solution is then generated.

Two questions arised from the first model: i) Is it necessary to have $p \geq 1$ for growth concentrate at the tip? ii) Apart from the closed form solution and the explicit tip shape, what are other features represented by the model? These questions motivate us to investigate $p \geq 0$ closer, namely, effect of choosing different p on the geometric tip shape and what it says about localization of wall-building material deposition. We give a full derivation of the generalized formulae for the tip shape.

Referring to the second model, we thought that in order to model the growth, N is not necessarily be a constant 1. The possibility of a new choice of N must satisfy with the wall-buidling material deposition of hyphal tip. From that it follows we investigate such that $N(K_m, K_g) \neq 1$ in order to generate the tip shape. We show that using the new choice of N captures some biological process that is ignored by setting $N \equiv 1$. Morever, the computation for generating the tip shape using the new N is much simpler, which as well results in a closed form of solution.

This chapter is started off with the definitions used in this work, then is followed by model related to the longitudinal curvature, κ and finally model related to mean and *Gaussian* curvatures.

2.4 Definitions

2.4.1 Material Point and Material Coordinate

A material point can be considered as a particle, that is, a small volumetric element of a continuum. The material coordinate is a set of values that tells a position of the particle. For simplicity, we denote both material point and material coordinate using the same notation σ [56].

2.4.2 Coordinate Systems

Generally, growth is the process where a body increases in size through continuous addition of mass. Accordingly, the body is accompanied by geometric deformation. Hyphal growth is special because it is restricted to its apical region only.

To describe hyphal tip growth, it is helpful to have two Cartesian coordinate systems. Suppose that the tip initially occupies a configuration, called, the reference configuration, where a material point, σ, occupies the position in the reference configuration. After application of wall-building material deposition, σ changes its position and so assumes a new configuration for a new position of σ, called the current configuration [56].

Half the medial section of hyphal filament geometry, C, is shown in Figure 2.6. The reference configuration is (X, Y)-plane and the current configuration is (x, y)-plane. Note that C is a parametric curve, which can be parameterized by arc length, s, and time, t. As presented in Figure 2.6, a growing hyphal filament is modeled by assuming that it is axisymmetric about the y-axis in the (x, y)-plane. Furthermore, the growth direction of the hyphal tip is set in the y-direction with magnitude U_0. To get a basic 3-D representation of hyphal filament geometry from its half the medial section, the profile C is rotated about the y-axis through

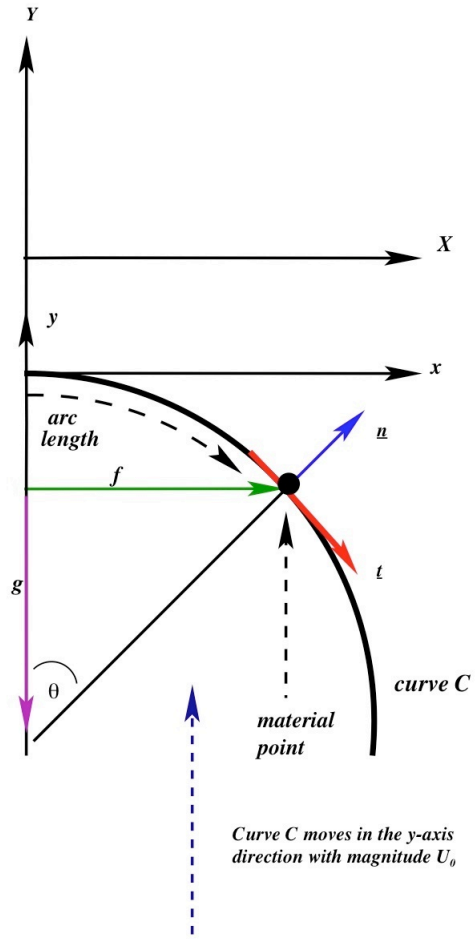

Figure 2.6: The medial section, C, of a generic hyphal tip. For a given material point, σ, arc length, $s(\sigma)$, is measured from the apex of the shell to that point, $f(s)$ is the radial distance from the y-axis to that point and $\underline{\mathbf{n}}$ and $\underline{\mathbf{t}}$ denote the normal and tangent vectors, respectively. The angle, $\theta(s)$, is the angle between the normal direction and the y-axis. Only half the section is shown for clarity. Redrawn from [31].

an angle of 2π. The curve C in the (X, Y)-plane is defined by

$$\underline{\mathrm{r}}_C(s,t) \quad := \quad (X(s,t), Y(s,t)). \tag{2.28}$$

From Equation (2.28), it follows that [31] introduced two assumptions. First, assume s is given as a function of σ and t, that is, $s = s(\sigma, t)$ and so

$$\underline{\mathrm{r}}_C(s(\sigma,t),t) \;=\; (X(s(\sigma,t),t),Y(s(\sigma,t),t)). \tag{2.29}$$

Second, it is further assumed that $X(s(\sigma,t),t) = x(s(\sigma,t))$ and $Y(s(\sigma,t),t) = y(s(\sigma,t)) + U_0$ and so C now is given by

$$\underline{\mathrm{r}}_C(s(\sigma,t),t) \;=\; (x(s(\sigma,t)), y(s(\sigma,t)) + U_0 t). \tag{2.30}$$

From Equation (2.30), although there is no time dependence in x and y, s is dependent to time. Obviously, each value of s determines a point (x, y) on C. The curve C can also be defined in terms of f and g as illustrated in Figure 2.6, that is

$$\underline{\mathrm{r}}_C(s(\sigma,t),t) \;=\; (f(s(\sigma,t)), g(s(\sigma,t)) + U_0 t). \tag{2.31}$$

Mark that we will use Equation (2.31) in subsequent calculations.

We are interested in changes of σ with respect to t and its relationship with the biology of hyphal growth. It is expected that after the wall-building material deposition at t, σ changes its position, which then gives changes in s as illustrated in Figure 2.7.

2.4.3 Wall Stretching

In response to wall-building material deposition and internal pressure, the tip stretches. The stretching tip can be thought in two ways; longitudinal and latitudinal.

Based on Figure 2.6, the longitudinal stretching, λ, is referred to an increasing arc length s and is defined by

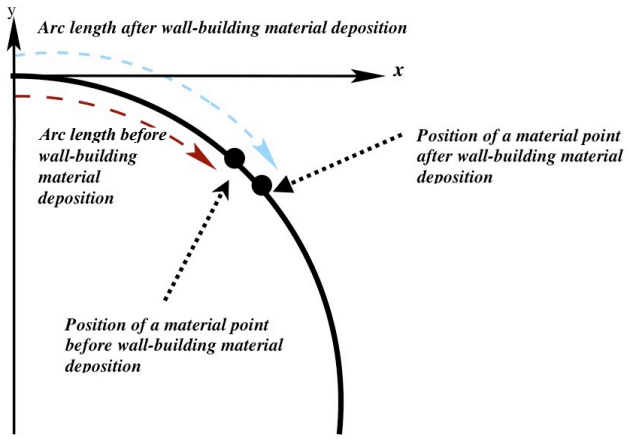

Figure 2.7: A temporal process of half the medial section, C, of a generic hyphal tip. Arc length depends on the position of material point, σ at the given time, t.

$$\lambda := \frac{\partial s(\sigma, t)}{\partial \sigma}, \tag{2.32}$$

It is assumed that λ is dependent to t implicitly. From Equation (2.32), it follows that if $\lambda = 1$, deformation does not occur. While, for $\lambda > 1$ or $\lambda < 1$ indicate the curve C is being stretched or compressed, respectively.

The latitudinal stretching, $\hat{\lambda}$, is defined by

$$\hat{\lambda} := \frac{1}{f}\frac{\partial f(s(\sigma, t))}{\partial t}, \tag{2.33}$$

where it represents the stretching wall in the f-direction as described in Figure 2.6.

2.4.4 Geometric Variables

As illustrated in Figure 2.6, $\theta(s)$ is the angle between the normal direction and the y-axis. In the calculations to follow, we will require the total differential of s denoted by ds. To understand this, refer to Figure 2.8 and so we have as follows:

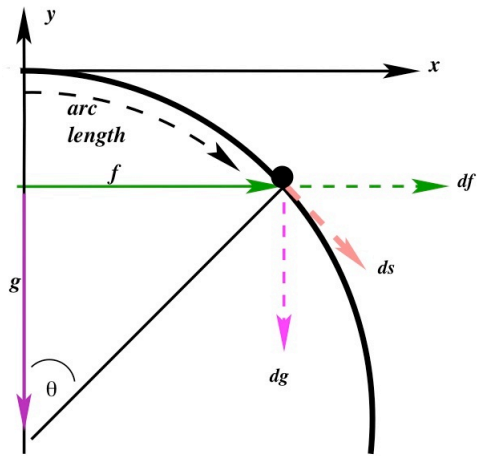

Figure 2.8: A schematic representation of geometeric variables $\frac{df}{ds}$ and $\frac{dg}{ds}$.

$$\frac{df}{ds} = \cos\theta,$$

while,

$$\begin{aligned} -\frac{dg}{ds} &= \cos\left(\frac{\pi}{2} - \theta\right), \\ &= \sin\theta, \end{aligned}$$

that is,

$$\frac{dg}{ds} = -\sin\theta.$$

2.4.5 Velocity of Material Point

As illustrated by Figure 2.6, the velocity of a material point, σ, embedded on the tip surface has two components, namely tangent, $\underline{\mathbf{t}}$ and normal, $\underline{\mathbf{n}}$. The unit tangent vector $\underline{\mathbf{t}}$ to C is defined by

$$\underline{\mathbf{t}} = \frac{\left(\frac{df}{ds}, \frac{dg}{ds}\right)}{\sqrt{\left(\frac{df}{ds}\right)^2 + \left(\frac{dg}{ds}\right)^2}}, \tag{2.34}$$

$$= (\cos\theta, -\sin\theta). \tag{2.35}$$

The unit outward normal vector $\underline{\mathbf{n}}$ is a vector that is perpendicular to $\underline{\mathbf{t}}$ and is defined by

$$\underline{\mathbf{n}} = \frac{\left(\frac{d(\cos\theta)}{ds}, \frac{d(-\sin\theta)}{ds}\right)}{\sqrt{\left(\frac{d(\cos\theta)}{ds}\right)^2 + \left(\frac{d(-\sin\theta)}{ds}\right)^2}}, \tag{2.36}$$

$$= (\sin\theta, \cos\theta). \tag{2.37}$$

The velocity can now be written in terms of tangential $\underline{\mathbf{t}}$ and normal $\underline{\mathbf{n}}$ vectors given by

$$\frac{d\underline{\mathrm{r}}_C(\sigma,t))}{dt} = W\underline{\mathbf{t}} + U\underline{\mathbf{n}}, \tag{2.38}$$

where W and U denote the magnitude of the tangential $\underline{\mathbf{t}}$ and normal $\underline{\mathbf{n}}$ components of the velocity, respectively, at each σ attached in the cell wall. By direct calculations, we have as follows

$$\frac{d\underline{\mathrm{r}}_C(\sigma,t))}{dt} = \left(\frac{df}{ds}\frac{\partial s}{\partial t}, \frac{dg}{ds}\frac{\partial s}{\partial t} + U_0\right). \tag{2.39}$$

Taking the scalar product of Equation (2.39) with $\underline{\mathbf{t}}$ and $\underline{\mathbf{n}}$, respectively, and using Equations (2.35) and (2.37) yields

$$U = \underline{\mathbf{n}} \cdot \frac{d\underline{\mathrm{r}}_C(\sigma,t))}{dt} = U_0\frac{df}{ds}, \tag{2.40}$$

and

$$W = \underline{\mathbf{t}} \cdot \frac{d\underline{\mathrm{r}}_C(\sigma,t))}{dt} = \frac{\partial s}{\partial t} + U_0\frac{dg}{ds}. \tag{2.41}$$

Take note that, in 1892, [67] proposed a hypothesis stating material points embedded in the cell wall move normal to the cell wall. By employing this hypothesis, the magnitude of the tangential component should be vanished and so set $W = 0$. Therefore from Equation (2.41)

$$\frac{\partial s}{\partial t} = -U_0 \frac{dg}{ds}. \tag{2.42}$$

2.4.6 Curvature

The longitudinal curvature κ is described by change in angle between two tangent vectors with respect to change in arc length. Consider Figure 2.9 to understand this.

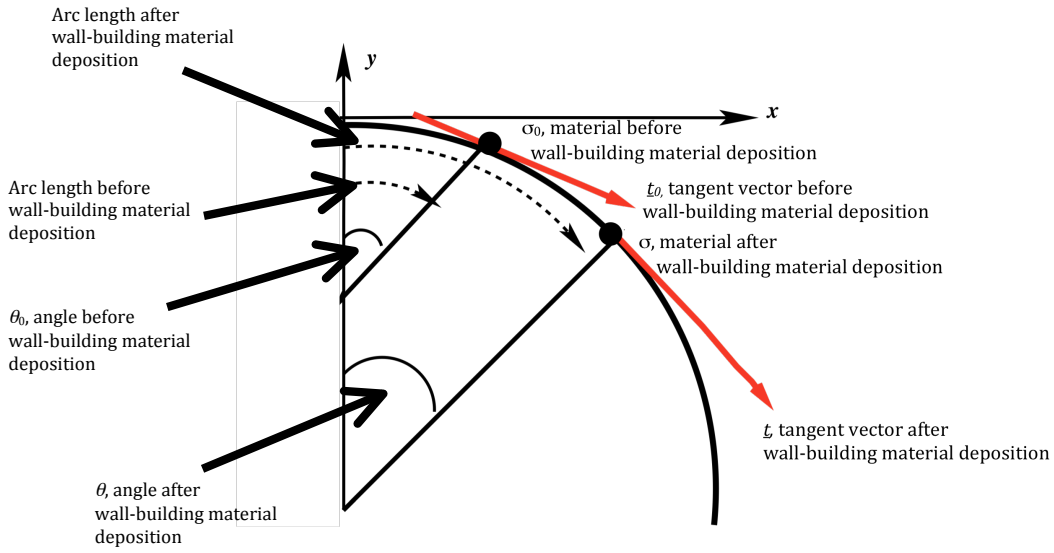

Figure 2.9: Figurative presentation of the longitudinal curvature, κ before and after the wall-building material deposition.

Based on Figure 2.9, let σ_0 and σ be two points on the curve C. The average curvature of the arc from σ_0 to σ is expressed by the fraction, $\frac{\Delta\theta}{\Delta s}$, where $\Delta\theta$ and Δs are change in angle and arc length, respectively. From that it follows κ at σ_0 is defined by

$$\kappa = \lim_{\Delta x \to 0} \frac{\Delta\theta}{\Delta s}. \tag{2.43}$$

$$= \frac{d\theta}{ds}. \tag{2.44}$$

The latitudinal curvature of C at any point on the curve can be thought as the curvature of the osculating circle, which approximates the curve most closely near that point. The latitudinal curvature k is defined by

$$k = \frac{\sin\theta}{f}, \tag{2.45}$$

which is equivalent to $\frac{1}{h}$, namely, h is a hypotenuse of a right triangle with f and g as its sides as illustrated in Figure 2.6.

2.5 Modeling Rates

This section models wall stretching rate and growth rate using the definitions as explained earlier. These rates are important parts of the geometric model construction.

2.5.1 Rate of Wall Stretching

The derivation of the rate of wall stretching begins by considering Equation (2.42). Firstly, differentiating the left-hand side of Equation (2.42) with respect to σ results in

$$\frac{\partial}{\partial\sigma}\left(\frac{\partial s}{\partial t}\right) = \frac{\partial}{\partial t}\left(\frac{\partial s}{\partial\sigma}\right) = \frac{\partial\lambda}{\partial t}. \tag{2.46}$$

Next, differentiating the right-hand side of Equation (2.42) with respect to σ yields

$$-U_0\frac{\partial}{\partial\sigma}\left(\frac{dg}{ds}\right) = -U_0\frac{\partial s}{\partial\sigma}\frac{d}{ds}\left(\frac{dg}{ds}\right) = -U_0\lambda\frac{d}{ds}\left(\frac{dg}{ds}\right). \tag{2.47}$$

So from Equations (2.46)-(2.47),

$$\frac{1}{\lambda}\frac{\partial \lambda}{\partial t} = -U_0 \frac{d}{ds}\left(\frac{dg}{ds}\right). \tag{2.48}$$

The left-hand side of Equation (2.48) can be considered as the longitudinal stretching rate. Now, $\frac{d}{ds}\left(\frac{dg}{ds}\right) = \frac{\partial \theta}{\partial s}\frac{\partial}{\partial \theta}\left(\frac{dg}{ds}\right)$ and so finally we have

$$\frac{1}{\lambda}\frac{\partial \lambda}{\partial t} = U_o \kappa \frac{df}{ds} = \kappa U_0 \cos\theta = \kappa U, \tag{2.49}$$

where from Equation (2.40), $U = U_0 \cos\theta$, the normal component of velocity at each point along the curve. The rate of wall stretching formula given in Equation (2.49) perhaps can be useful for experimental work. Accordingly, this can be done provided that U_0 is able to be estimated through images of a time lapsed sequence of growth and the tip profile is clear enough to compute its curvature.

2.5.2 Growth Rate

Growth rate of the tip wall can be described in terms of increment of area ΔA. Referring to Figure 2.10, the circumference of the tip at any point along the curve is $2\pi f$.

It follows that a *band* of increment of area ΔA around the tip is approximately given by

$$\begin{aligned} \Delta A &\approx 2\pi f \Delta s, \\ &\approx 2\pi f \frac{\partial s}{\partial \sigma}\Delta\sigma, \\ &= 2\pi f \lambda \Delta\sigma. \end{aligned} \tag{2.50}$$

Differentiating both sides of Equation (2.50) with respect to t gives

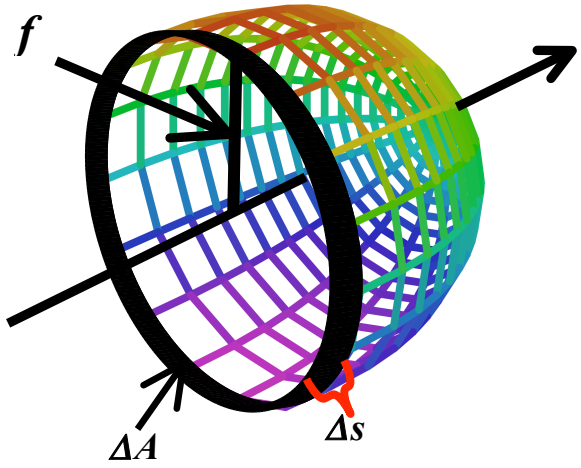

Figure 2.10: A "band" of increment of area ΔA around the tip and Δs represents the "band" width.

$$\frac{d}{dt}\Delta A = 2\pi\left(\frac{\partial f}{\partial t}\lambda + f\frac{\partial \lambda}{\partial t}\right)\Delta\sigma. \tag{2.51}$$

Noting that $\frac{\partial f}{\partial t}\lambda + f\frac{\partial \lambda}{\partial t} = \frac{df}{ds}\frac{\partial s}{\partial t}\lambda + f\frac{\partial \lambda}{\partial t}$, then Equation (2.51) becomes

$$\frac{d}{dt}\Delta A = 2\pi f\lambda\left(\frac{\frac{\partial s}{\partial t}\frac{df}{ds}}{f} + \frac{\frac{\partial \lambda}{\partial t}}{\lambda}\right)\Delta\sigma. \tag{2.52}$$

Dividing both sides of Equation (2.52) by ΔA and simplifying it lead to

$$\frac{1}{\Delta A}\frac{d}{dt}\Delta A = \frac{\frac{\partial s}{\partial t}\frac{df}{ds}}{f} + \frac{1}{\lambda}\frac{\partial \lambda}{\partial t}. \tag{2.53}$$

The growth of an area element per (unit) area element is denoted by the left-hand side of Equation (2.53). While, the right-hand side of Equation (2.53) can be thought as the sum of local latitudinal and longitudinal stretching rates, respectively. Next, an assumption is made that approximately equates the new incremented area to wall-building material deposition as follows

$$\frac{1}{\Delta A}\frac{d}{dt}\Delta A = N(s,t), \tag{2.54}$$

where $N = N_0 n(s,t)$. Here N_0 sets the fundamental time scale of the wall building process and $n(s,t)$ is a dimensionless function used to model the wall-building process.

2.6 Modeling wall-buidling material deposition

Let assume a special case in which hyphae are wide provided that slow growth due to pauses or shorter periods of growth [24]. Then, we may reasonably assume that $\frac{\frac{\partial s}{\partial t}\frac{df}{ds}}{f} << \frac{1}{\lambda}\frac{\partial \lambda}{\partial t}$. This means only the longitudinal stretching rate is considered and so we have

$$\frac{1}{\lambda}\frac{\partial \lambda}{\partial t} = N_0 n(s,t), \tag{2.55}$$

which gives $\kappa U_0 \frac{df}{ds} = N_0 n(s,t)$.

Alternatively, the longitudinal stretching rate (the left-hand side of Equation (2.55)) can as well be derived by considering increment of arc length, Δs. First off, Δs is approximately defined by

$$\Delta s \approx \frac{\partial s}{\partial \sigma}\Delta\sigma = \lambda\Delta\sigma. \tag{2.56}$$

Then differentiating both sides of Equation (2.56) with respect to t, it follows that

$$\frac{\partial}{\partial t}\Delta s = \frac{\partial}{\partial t}(\lambda\Delta\sigma) \approx \frac{\partial \lambda}{\partial t}\frac{\Delta s}{\lambda} = \frac{\partial \lambda}{\partial t}\Delta\sigma + \lambda\frac{\partial \Delta\sigma}{\partial t}. \tag{2.57}$$

However, $\sigma\frac{\partial\Delta\sigma}{\partial t} = 0$ as we consider σ and t are independent variables. Next, dividing Equation (2.57) by Δs gives

$$\frac{1}{\Delta s}\frac{\partial \Delta s}{\partial t} = \frac{1}{\lambda}\frac{\partial \lambda}{\partial t}. \tag{2.58}$$

The left-hand side of Equation (2.58) is the growth of arc length s per unit s, which is balanced by the longitudinal stretching rate. Note that however, we prefer to consider growth rate with respect to increment of area ΔA and so from Equation (2.55), it follows

$$\frac{\frac{df}{ds}\frac{d}{ds}\left(\frac{df}{ds}\right)}{\left(1-\left(\frac{df}{ds}\right)^2\right)^{1/2}} = -\alpha n(s,t), \tag{2.59}$$

or by simplifying Equation (2.59) yields

$$\cos\theta\kappa = \frac{1}{\alpha}n(s,t), \tag{2.60}$$

where $\alpha = \frac{U_0}{N_0}$ and $n(s,t)$ is the wall-building material deposition. The wall-building material deposition is assumed to be $n(s,t) \propto \kappa^p$, namely, $n = \frac{\kappa^p}{\kappa_0^p}$ as proposed by [31]. Formula Equation (2.60) is very important in generating the tip shape of wide hyphae with slow growth due to pauses or shorter periods of growth [24].

2.7 Geometric Model: Special Case

This section focuses on the derivation of the generalized formulae for the tip shape of wide hyphae with slow growth, the generalized formulae for its longitudinal curvature and its generalized wall-building material deposition. We will investigate Equation (2.60), namely, $n = \frac{\kappa^p}{\kappa_0^p}$ for different p's.

2.7.1 Derivation of the generalized formulae

We begin by showing a figurative representation of the "tip radius", $f(\theta)$ and the "tip length", $g(\theta)$ in Figure 2.11.

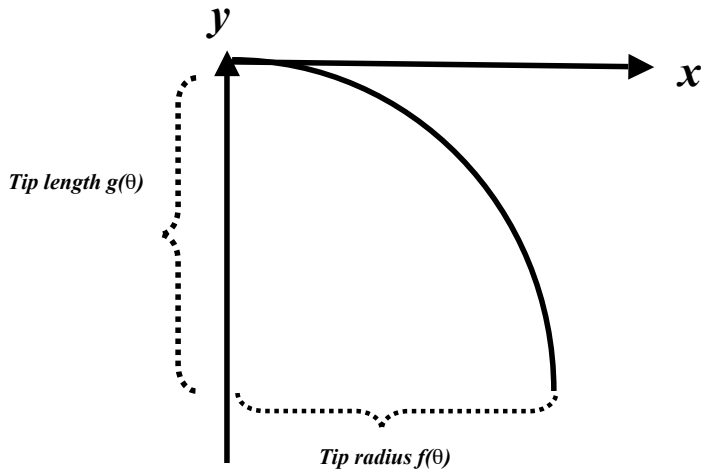

Figure 2.11: Figurative representation of the "tip radius" $f(\theta)$ and the "tip length" $g(\theta)$.

The generalized formulae for generating the tip shape is made up by *tip radius* $f(\theta)$ and *tip length* $g(\theta)$ through Equation (2.60). We first derive formula for $f(\theta)$. Substituting $n(s,t) = \frac{\kappa^p}{\kappa_0^p}$ in Equation (2.60) and simplifying yields

$$\cos\theta \;=\; \frac{1}{\alpha\kappa_0^p}\kappa^{p-1}. \tag{2.61}$$

Subsequently, multiply both sides of Equation (2.61) with $\frac{1}{\kappa}$, $(\kappa \neq 0)$, which gives

$$\cos\theta\frac{1}{\kappa} \;=\; \frac{1}{\alpha\kappa_0^p}\kappa^{p-2}. \tag{2.62}$$

Recall that $\kappa = \frac{d\theta}{ds} = \frac{d\theta}{df}\frac{df}{ds}$ and $\cos\theta = \frac{df}{ds}$. By substituting these in Equation (2.62), we get

$$\frac{df}{d\theta} = \frac{1}{\alpha\kappa_0^p}\left(\frac{d\theta}{df}\right)^{p-2}(\cos\theta)^{p-2}. \tag{2.63}$$

Multiplying both sides of Equation (2.63) with $\left(\frac{df}{d\theta}\right)^{p-2}$ and simplifying gives

$$\left(\frac{df}{d\theta}\right)^{p-1} = \frac{1}{\alpha\kappa_0^p}(\cos\theta)^{p-2}, \tag{2.64}$$

$$\frac{df}{d\theta} = \left(\frac{1}{\alpha\kappa_0^p}(\cos\theta)^{p-2}\right)^{\frac{1}{p-1}}, \tag{2.65}$$

provided $p \neq 1$. Integrating both sides of Equation (2.65) with respect to θ gives

$$f(\theta) = \frac{1}{(\alpha\kappa_0^p)^{\frac{1}{p-1}}}\int_0^\theta (\cos\phi)^{\frac{p-2}{p-1}}\, d\phi, \tag{2.66}$$

where we have used $f(0) = 0$ and it is assumed that $\alpha = 1 = \kappa_0$. Take note that such assumption will be used and appeared repeatedly in the subsequent calculations.

Secondly, we derive a general expression for $g(\theta)$. The chain rule yields

$$\frac{dg}{d\theta} = \frac{dg}{df}\frac{df}{d\theta}, \tag{2.67}$$

and on substituting $\frac{dg}{df} = -\tan\theta$ and Equation (2.65) in Equation (2.67) gives

$$\frac{dg}{d\theta} = -\tan\theta\frac{1}{(\alpha\kappa_0^p)^{\frac{1}{p-1}}}(\cos\theta)^{\frac{p-2}{p-1}}, \tag{2.68}$$

where as above, we assume $p \neq 1$. Integrating both sides of Equation (2.68) with respect to θ gives

$$g(\theta) = -\frac{1}{(\alpha\kappa_0^p)^{\frac{1}{p-1}}}\int_0^\theta \frac{\sin\phi}{(\cos\phi)^{\frac{1}{p-1}}}d\phi, \tag{2.69}$$

where using $g(0) = 0$.

Finally, it follows directly from Equation (2.60) that a generalized formulae for longitudinal curvature κ is

$$\kappa = (\alpha\kappa_0^p)^{\frac{1}{p-1}}(\cos\theta)^{\frac{1}{p-1}}. \tag{2.70}$$

(Alternatively, one could derive the formulae Equation (2.70) easily using the chain rule as following: $\kappa = \frac{d\theta}{ds} = \frac{d\theta}{df}\frac{df}{ds}$ or $\frac{d\theta}{dg}\frac{dg}{ds}$). Note that the (asymptotic) "tip radius" and (asymptotic) "tip length" to be located at $\theta = \frac{\pi}{2}$. It is instructive, therefore to investigate the limit of f, g and κ as $\theta \to \frac{\pi}{2}$. Considering κ first, we have

$$\lim_{\theta\to\frac{\pi}{2}} \kappa = \infty \quad \text{for} \quad 0 \le p < 1, \tag{2.71}$$

$$= 0 \quad \text{for} \quad p > 1. \tag{2.72}$$

A smooth matching between the cylinder and the tip requires that $\kappa \to 0$ as $\theta \to \frac{\pi}{2}$. Clearly then this can only occur if $p > 1$. The wall-building material deposition $n(s,t)$ is proportional to κ^p and so if $p = 0$, then the wall-building materials are deposited equally everywhere on the tip. For $0 \le p < 1$, maximum wall-building material deposition occurs at the most distal region of the tip. This contradicts known fungal physiology. However, in the following, we will consider this case for the sake of completeness. Moreover, we note that with formation of pollen tubes, the wall-building material deposition occurs at the most distal region part of the soft tip [10]. Another very important aspect for generating tip shapes is to examine whether the tip is finite length or not.

Next, from Equation (2.66), it follows that provided the limit exists,

$$\lim_{\theta \to \frac{\pi}{2}} f(\theta) = f\left(\frac{\pi}{2}\right), \tag{2.73}$$

$$= K\frac{\Gamma(h)}{\Gamma(h+\frac{1}{2})}, \tag{2.74}$$

where Γ is a gamma function of h, namely, $h = \left(\frac{1}{2}\frac{p-2}{p-1} + \frac{1}{2}\right)$, $K = \frac{1}{(\alpha\kappa_0^p)^{\frac{1}{p-1}}}\frac{\sqrt{\pi}}{2}$, $\alpha = 1 = \kappa_0$ and $p \geq 0$. A plot of $f\left(\frac{\pi}{2}\right)$ for $0 \leq p \leq 5$ based on Equation (2.74) is shown in Figure 2.12. We see that the behavior for $1 < p \leq 1.5$ appears somewhat erratic. This gives us the motivation to study the different cases of p.

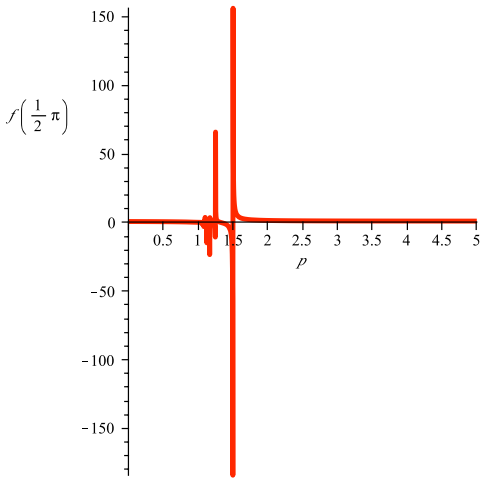

Figure 2.12: A plot of $f\left(\frac{\pi}{2}\right)$ for $0 \leq p \leq 5$, $\alpha = \kappa_0 = 1$ in which the general expression of $f\left(\frac{\pi}{2}\right)$ for every p is given in Equation (2.74).

Furthermore, from Equation (2.74), generally we know that the gamma function of a positive integer is itself a positive integer. While the gamma function of a negative integer is invariably infinite. The gamma function of zero is infinite, while the gamma function of one is one. We will discuss different cases of p for Equation (2.74) based on properties of the gamma function.

Similarly, if the limit exists, it follows from Equation (2.69) that

$$\lim_{\theta \to \frac{\pi}{2}} g(\theta) = g\left(\frac{\pi}{2}\right), \tag{2.75}$$

$$= -\frac{1}{(\alpha\kappa_0^p)^{\frac{1}{p-1}}} \int_0^{\frac{\pi}{2}} \frac{\sin\phi}{(\cos\phi)^{\frac{1}{p-1}}} d\phi, \tag{2.76}$$

$$= \frac{1}{(\alpha\kappa_0^p)^{\frac{1}{p-1}}} \lim_{\theta \to \frac{\pi}{2}} \left[\left((\cos\theta)^{\frac{p-2}{p-1}} \frac{p-1}{p-2} \right) - \left(\frac{p-1}{p-2} \right) \right], \tag{2.77}$$

where α, κ_0 and p are as defined in Equation (2.74). A plot of $g\left(\frac{\pi}{2}\right)$ for $0 \leq p \leq 5$ based on Equation (2.77) is shown in Figure 2.13, which shows discontinuity for each $1 \leq p < 2$. This motivates us for studying the different cases of p.

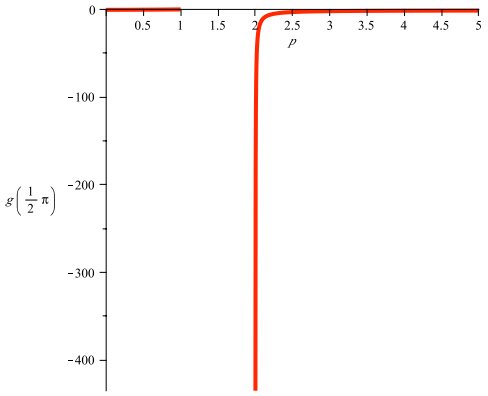

Figure 2.13: A plot of $g\left(\frac{\pi}{2}\right)$ for $0 \leq p \leq 5$, $\alpha = \kappa_0 = 1$ in which the general expression of $g\left(\frac{\pi}{2}\right)$ for every p is given in Equation (2.77).

Additionally, we examine the slope of C, which is defined by

$$\frac{df}{dg} = \frac{df}{ds}\frac{ds}{dg}. \tag{2.78}$$

Substituting Equation (2.66) and Equation (2.69) in Equation (2.78) yields

$$\frac{df}{dg} = -\frac{\cos\theta}{\sin\theta}. \tag{2.79}$$

At the apex, $\theta = 0$. Taking both sides of Equation (2.79) close to $\theta = 0$ leads to

$$\lim_{\theta \to 0} \frac{df}{dg} = -\frac{\cos\theta}{\sin\theta} = -\infty, \tag{2.80}$$

which shows the slope at the apex is represented by a vertical line. Next, taking both sides of Equation (2.79) close to $\theta = \frac{\pi}{2}$ yields

$$\lim_{\theta \to \frac{\pi}{2}} \frac{df}{dg} = -\frac{\cos\theta}{\sin\theta} = 0, \tag{2.81}$$

where the slope at the apex is represented by a horizontal line.

2.7.2 Cases

Case 1: $p = 0$

Note that since $p = 0$, so $n \propto$ constant. The wall-building material deposition is independent of κ, where the wall-building materials are deposited equally in the tip.

Substituting $p = 0$ in Equation (2.66) and Equation (2.69), respectively yields

$$f(\theta) = (\alpha\kappa_0^0)\left(\frac{\cos\theta\sin\theta}{2} + \frac{\theta}{2}\right), \tag{2.82}$$

and

$$g(\theta) = -(\alpha\kappa_0^0)\left(\frac{1}{2} - \frac{(\cos\theta)^2}{2}\right). \tag{2.83}$$

From Equation (2.82), the "tip radius" is

$$\lim_{\theta \to \frac{\pi}{2}} f(\theta) = \frac{\sqrt{\pi}}{2}\frac{\Gamma\left(\frac{3}{2}\right)}{\Gamma(2)}, \tag{2.84}$$

$$= \frac{\pi}{4}, \tag{2.85}$$

where $\alpha = 1 = \kappa_0$. While, from Equation (2.83), the "tip length" is

$$\lim_{\theta \to \frac{\pi}{2}} g(\theta) = \lim_{\theta \to \frac{\pi}{2}} \left[\left((\cos\theta)^2 \frac{1}{2} \right) - \left(\frac{1}{2} \right) \right], \tag{2.86}$$

$$= -\frac{1}{2}, \tag{2.87}$$

where $\alpha = 1 = \kappa_0$. Note that in the following computation of $\lim_{\theta \to \frac{\pi}{2}} f(\theta)$ and $\lim_{\theta \to \frac{\pi}{2}} g(\theta)$ for different p, we as well take $\alpha = 1 = \kappa_0$.

Equivalently, Equation (2.85) and Equation (2.87) can be achieved by substituting $p = 0$ in Equation (2.74) and Equation (2.77), respectively.

A parametric plot of Equation (2.82) and Equation (2.83) is shown in Figure 2.14.

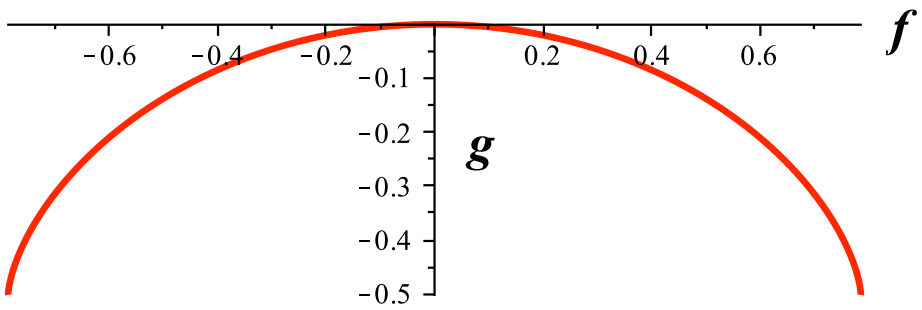

Figure 2.14: A parametric plot of $(f(\theta), g(\theta))$ for $p = 0$, $0 \leq \theta \leq \frac{\pi}{2}$, $\alpha = \kappa_0 = 1$ as given by Equation (2.82) and Equation (2.83).

Case 2: $0 < p < 1$

Referring to Equation (2.66), the general formula for the "tip radius" f is equivalent to

$$f(\theta) = (\alpha \kappa_0^p)^{\frac{1}{1-p}} \int_0^\theta (\cos\phi)^{\frac{2-p}{1-p}} \, d\phi, \tag{2.88}$$

and from Equation (2.69), the "the tip length" g is

$$g(\theta) \;=\; -(\alpha\kappa_0^p)^{\frac{1}{1-p}} \int_0^{\theta} (\sin\phi)(\cos\phi)^{\frac{1}{1-p}}\, d\phi. \tag{2.89}$$

When $\theta = \frac{\pi}{2}$, both Equation (2.88) and Equation (2.89) are bounded because the integrand of Equation (2.88) and Equation (2.89) are bounded.

As we mentioned earlier, the gamma function of a positive integer is a positive integer, while the gamma function of zero goes to infinity. From Equation (2.74), a plot of $f\left(\frac{\pi}{2}\right)$ for $0 < p < 1$ is shown in Figure 2.15. Plots of the numerator and denominator of Equation (2.74) is given by Figure 2.16. Based on the numerator of Equation (2.74), $\frac{2p-3}{2p-2} \in \left(\frac{3}{2}, +\infty\right)$ for $0 < p < 1$. This shows that $\frac{2p-3}{2p-2}$ results in positive integers for every p in this case. Hence, the numerator of Equation (2.74) are positive integers, where $\sqrt{\pi}\Gamma\left(\frac{2p-3}{2p-2}\right) \in \left(\sqrt{\pi}\Gamma\left(\frac{3}{2}\right), +\infty\right)$ for $0 < p < 1$. Similarly, from the denominator of Equation (2.74), $\frac{3p-4}{2p-2}$ gives positive integers for $0 < p < 1$. From that it follows $(\alpha\kappa_0^p)^{\frac{1}{p-1}} 2\Gamma\left(\frac{3p-4}{2p-2}\right) \in \left((\alpha\kappa_0^p)^{\frac{1}{p-1}} 2\Gamma(2), +\infty\right)$. However, the denominator increases slightly faster compared to the numerator and so Equation (2.88) is bounded. A plot of $g\left(\frac{\pi}{2}\right)$ is shown in Figure 2.17 based on Equation (2.77). In this case, $g\left(\frac{\pi}{2}\right)$ is bounded if exponent of $\cos\theta$ is equal or greater than 0 and so Equation (2.89) is bounded for every $0 < p < 1$.

As an example for this case, we choose $p = 0.5$. Subsequently, by substituting $p = 0.5$ in Equation (2.66) and Equation (2.69), respectively, yields

$$f(\theta) \;=\; \frac{1}{(\alpha\kappa_0^{0.5})^{-2}} \int_0^{\theta} (\cos\phi)^3 d\phi = \frac{(\cos\theta)^2 \sin\theta}{3} + \frac{2\sin\theta}{3}, \tag{2.90}$$

and

$$g(\theta) \;=\; -\frac{1}{(\alpha\kappa_0^{0.5})^{-2}} \int_0^{\theta} \frac{\sin\phi}{(\cos\phi)^{-2}} d\phi = -\frac{1}{3} + \frac{(\cos\theta)^3}{3}. \tag{2.91}$$

A parametric plot of Equation (2.90) and Equation (2.91) is shown in Figure 2.18. From Equation (2.90), the "tip radius" is

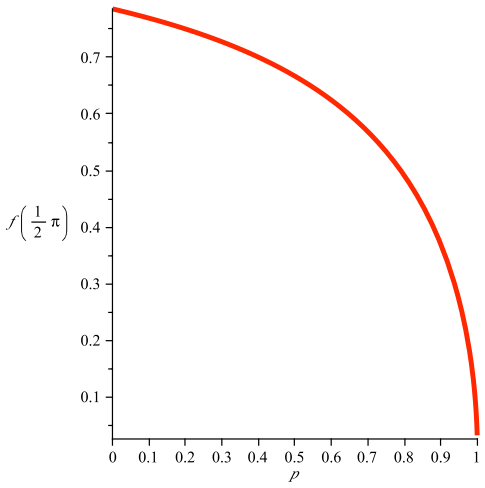

Figure 2.15: A plot of $f\left(\frac{\pi}{2}\right)$ for $0 < p < 1$, $\alpha = \kappa_0 = 1$ in which the general expression $f\left(\frac{\pi}{2}\right)$ for every p is given in Equation (2.74).

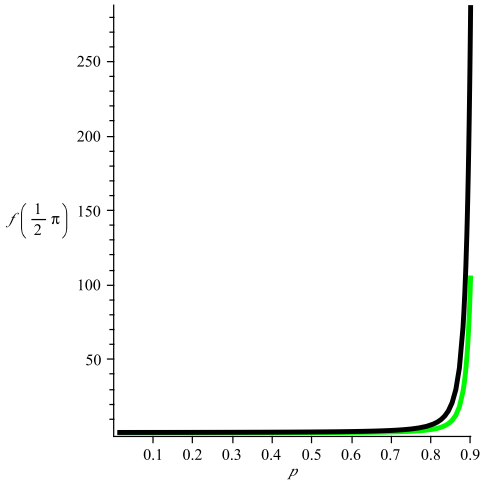

Figure 2.16: Plots of the numerator (green) and the denominator (black) of $f\left(\frac{\pi}{2}\right)$ for $0 < p < 1$ $\alpha = \kappa_0 = 1$ in which the general expression $f\left(\frac{\pi}{2}\right)$ for every p is given in Equation (2.74).

$$\lim_{\theta \to \frac{\pi}{2}} f(\theta) \quad = \quad \frac{2}{3}, \tag{2.92}$$

while, from Equation (2.91), the "tip length" is

$$\lim_{\theta \to \frac{\pi}{2}} g(\theta) \quad = \quad -\frac{1}{3}. \tag{2.93}$$

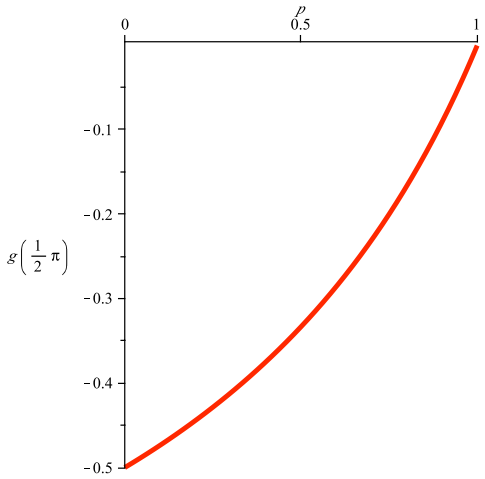

Figure 2.17: A plot of $g\left(\frac{\pi}{2}\right)$ for $0 < p < 1$, $\alpha = \kappa_0 = 1$ in which the general expression $g\left(\frac{\pi}{2}\right)$ for every p is given in Equation (2.77).

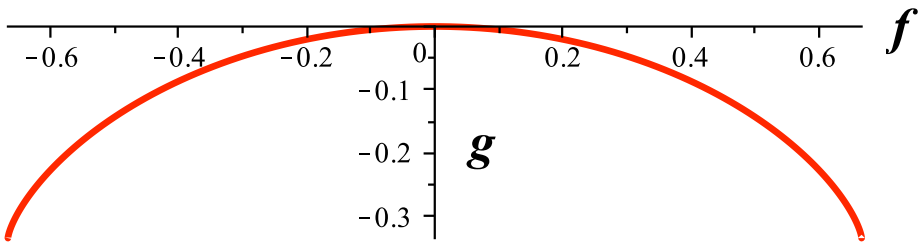

Figure 2.18: A parametric plot of $(f(\theta), g(\theta))$ for $p = 0.5$, $0 \leq \theta \leq \frac{\pi}{2}$, $\alpha = \kappa_0 = 1$ as given by Equation (2.90) and Equation (2.91).

Additionally, as stated by [31], $p = 1$ is not relevant to the tip geometry. Substituting $p = 1$ in Equation (2.61) yields $\theta = \cos^{-1}\left(\frac{1}{\alpha\kappa_0}\right)$, which is a constant.

In Figure 2.19, we show a plot showing the tip shape for various values of p for $0 < p < 1$. Such plot simply describes how p alters the tip shape in between $0 < p < 1$.

Case 3: $1 < p \leq 1.5$

As illustrated by Figure 2.12, behavior for $1 < p \leq 1.5$ appears somewhat erratic and so we discuss it here.

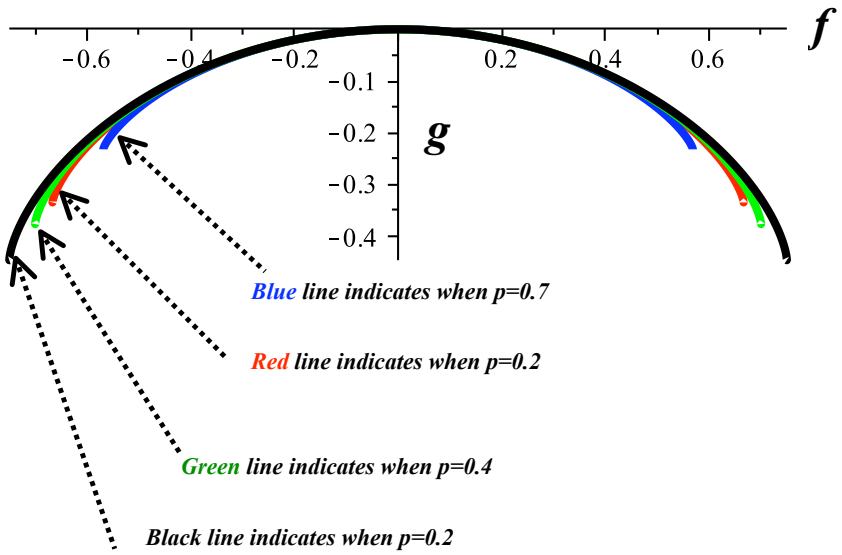

Figure 2.19: A parametric plot showing the tip shape for various values of p for $0 < p < 1$.

Rewriting the general expression of the "tip radius" $f(\theta)$ given in Equation (2.66) yields

$$f(\theta) = \frac{1}{(\alpha\kappa_0^p)^{\frac{1}{p-1}}} \int_0^\theta \left(\frac{1}{(\cos\phi)^{\frac{2-p}{p-1}}} \right) d\phi, \tag{2.94}$$

and the general expression of the "tip length" $g(\theta)$ is as in Equation (2.69). Both Equation (2.94) and Equation (2.69) show an unbounded integrand when $\theta = \frac{\pi}{2}$.

The gamma function of a negative integer is invariably infinite and same holds for the gamma function of zero. A plot of $f\left(\frac{\pi}{2}\right)$ for $1 < p \leq 1.5$ based on Equation (2.74) is shown in Figure 2.20. Plots of the numerator (green) and the denominator (black) of $f\left(\frac{\pi}{2}\right)$ for $1 < p \leq 1.5$ are given in Figure 2.21. Referring to the numerator of Equation (2.74), $\frac{2p-3}{2p-2}$ gives negative integers for $1 < p \leq 1.5$, namely $\frac{2p-3}{2p-2} \in (-\infty, 0)$. Subsequently, the numerator of Equation (2.74), $\sqrt{\pi}\Gamma\left(\frac{2p-3}{2p-2}\right)$, shows infinite number of p's go to infinity as shown in Figure 2.20. While, from the denominator of Equation (2.74), $\frac{3p-4}{2p-2}$ as well gives negative

integers for $1 < p \leq 1.5$, where $\frac{3p-4}{2p-2} \in (-\infty, 0.5)$. Therefore, the denominator of Equation (2.74), $(\alpha\kappa_0^p)^{\frac{1}{p-1}} 2\Gamma\left(\frac{3p-4}{2p-2}\right)$, shows infinite number of p's go to infinity for $1 < p \leq 1.5$ shown in Figure 2.20. All these tells us that the tip radius is not relevant for p in this case. From Equation (2.77), $g\left(\frac{\pi}{2}\right)$ is unbounded because exponent of $\cos\theta$ is less than 0 for every $1 < p \leq 1.5$ and so the tip length is as well not relevant in this case.

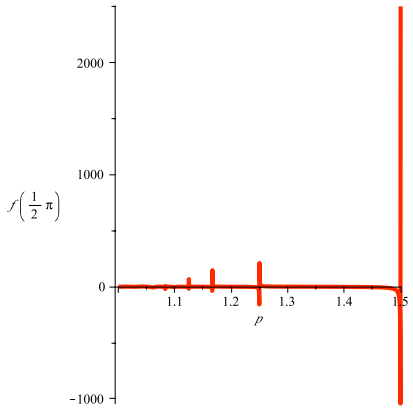

Figure 2.20: A plot of $f\left(\frac{\pi}{2}\right)$ for $1 \leq p \leq 1.5$, $\alpha = \kappa_0 = 1$ in which the general expression $f\left(\frac{\pi}{2}\right)$ for every p is given in Equation (2.74).

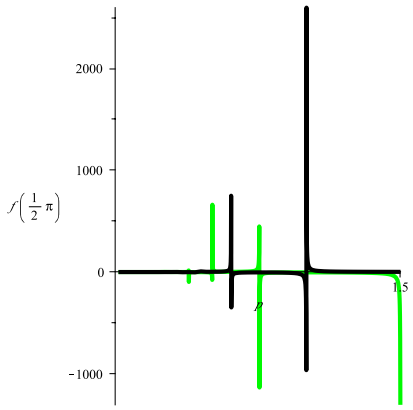

Figure 2.21: Plots of the numerator (green) and the denominator (black) of $f\left(\frac{\pi}{2}\right)$ for $1 < p \leq 1.5$, $\alpha = \kappa_0 = 1$ in which the general expression $f\left(\frac{\pi}{2}\right)$ for every p is given in Equation (2.74).

Case 4: $1.5 < p < 2$

The general expression of the "tip radius" in Equation (2.66) for p in this region is given by Equation (2.94) and the "tip length" is by Equation (2.69). For $1.5 < p < 2$, when $\frac{\pi}{2}$, the integrand of Equation (2.94) is bounded and so Equation (2.94) is well-defined. But the integrand of Equation (2.69) is unbounded.

A plot of $f\left(\frac{\pi}{2}\right)$ for $1.5 < p < 2$ based on Equation (2.74) is shown in Figure 2.22. Similarly, plots of the numerator (green) and the denominator (black) of $f\left(\frac{\pi}{2}\right)$ for $1.5 < p < 2$ are given in Figure 2.23. Referring to the numerator of Equation (2.74), $\frac{2p-3}{2p-2}$ gives positive integers, where $\frac{2p-3}{2p-2} \in (0, 0.5)$ for $1 < p < 1.5$. From that it follows, the numerator of Equation (2.74), $\sqrt{\pi}\Gamma\left(\frac{2p-3}{2p-2}\right) \in (0, +\infty)$ for $1 < p < 1.5$. While, from the denominator of Equation (2.74), $\frac{3p-4}{2p-2}$ as well gives positive integers for $1 < p \leq 1.5$, where $\frac{3p-4}{2p-2} \in (0, 1)$. Therefore, the denominator of Equation (2.74), $(\alpha\kappa_0^p)^{\frac{1}{p-1}} 2\Gamma\left(\frac{3p-4}{2p-2}\right) \in (2, 2\Gamma(0.5))$. From Equation (2.77), $g\left(\frac{\pi}{2}\right)$ is unbounded because exponent of $\cos\theta$ is less than 0 for every $1.5 < p < 2$ and so the tip length is not relevant in this case.

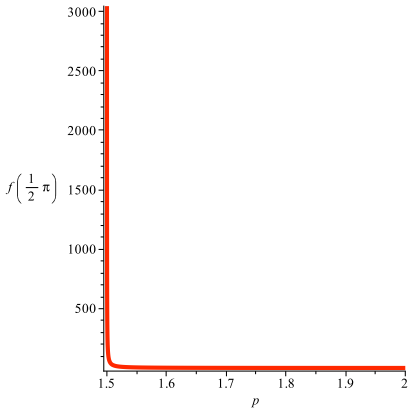

Figure 2.22: A plot of $f\left(\frac{\pi}{2}\right)$ for $1.5 < p < 2$, $\alpha = \kappa_0 = 1$ in which the general expression $f\left(\frac{\pi}{2}\right)$ for every p is given in Equation (2.74).

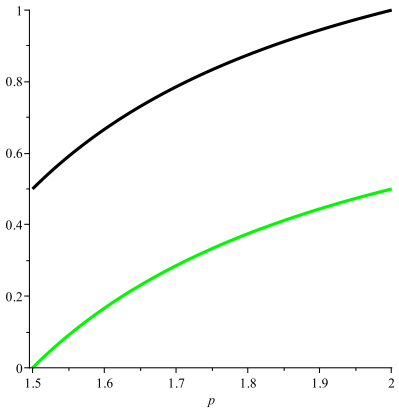

Figure 2.23: Plots of the numerator (green) and the denominator (black) of $f\left(\frac{\pi}{2}\right)$ for $1.5 < p < 2$, $\alpha = \kappa_0 = 1$ in which the general expression $f\left(\frac{\pi}{2}\right)$ for every p is given in Equation (2.74).

Case 5: $p = 2$

The choice of $p = 2$ is chosen by [31]. By using our approach and substituting $p = 2$ respectively in Equation (2.66) and Equation (2.69) yields

$$f(\theta) = \frac{1}{(\alpha\kappa_0^2)}\int_0^\theta d\phi = \frac{1}{(\alpha\kappa_0^2)}\theta, \tag{2.95}$$

and

$$g(\theta) = -\frac{1}{(\alpha\kappa_0^2)}\int_0^\theta \frac{\sin\phi}{\cos\phi}d\phi = \frac{1}{(\alpha\kappa_0^2)}\ln(\cos\theta). \tag{2.96}$$

A parametric plot of Equation (2.95) and Equation (2.96) is shown in Figure 2.24.

The "tip radius" given by Equation (2.91) is

$$\lim_{\theta\to\frac{\pi}{2}} f(\theta) = \frac{\pi}{2}. \tag{2.97}$$

While, the "tip length" in Equation (2.92) is

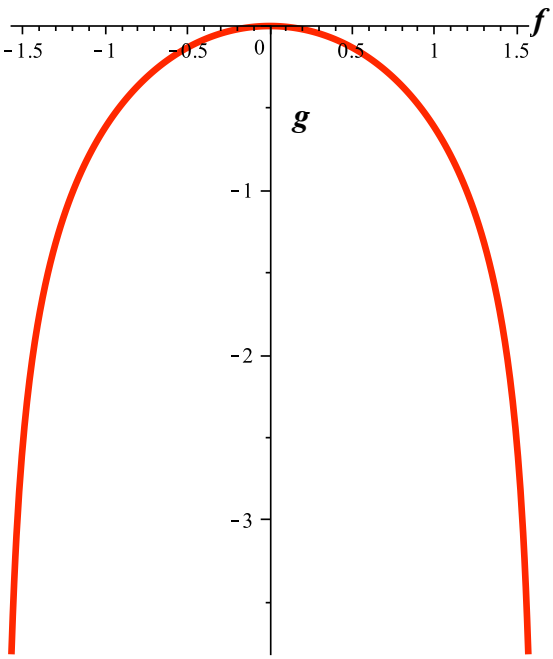

Figure 2.24: A plot of $(f(\theta), g(\theta))$ for $p = 2$, $0 \leq \theta \leq \frac{\pi}{2}$, $\alpha = \kappa_0 = 1$ as given by Equation (2.95) and Equation (2.96) based on the general expressions of Equation (2.66) and Equation (2.69).

$$\lim_{\theta \to \frac{\pi}{2}} g(\theta) \quad = \quad -\infty. \tag{2.98}$$

Both Equation (2.97) and Equation (2.98) can as well be achieved directly from Equation (2.74) and Equation (2.77). Referring to Equation (2.98), the ''tip length" seems unreasonable since the wall-building material deposition does not occur at distal region.

For $p = 2$, one can describe the plot in Figure 2.24 in terms of x and y. From Equation (2.91), $\theta = (\alpha\kappa_0^2)f$ and substituting it in Equation (2.92) yields $g = \frac{1}{\alpha\kappa_0^2}\log(\cos(\alpha\kappa_0^2 f))$. This is equivalently to $y = \frac{1}{\alpha\kappa_0^2}\log(\cos(\alpha\kappa_0^2 x))$.

Case 6: $p > 2$

Referring to Equation (2.66), the integrand of Equation (2.66) is bounded for $p > 2$ when $\theta = \frac{\pi}{2}$ and so the integral in Equation (2.66) is well-defined. Similarly, for the integrand of Equation (2.69).

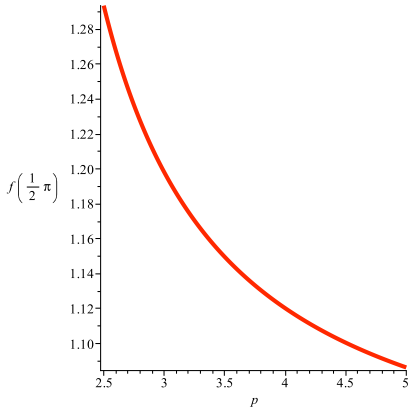

Figure 2.25: A plot of $f\left(\frac{\pi}{2}\right)$ for $p > 2$, $\alpha = \kappa_0 = 1$ in which the general expression $f\left(\frac{\pi}{2}\right)$ for every p is given in Equation (2.74).

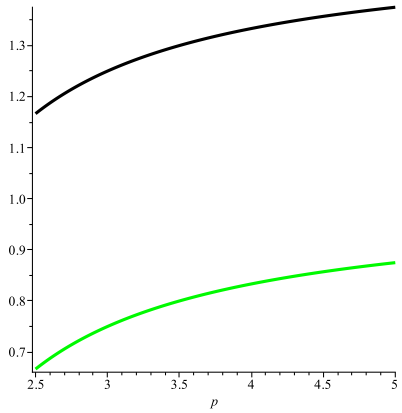

Figure 2.26: Plots of the numerator (green) and the denominator (black) of $f\left(\frac{\pi}{2}\right)$ for $p > 2$, $\alpha = \kappa_0 = 1$ in which the general expression $f\left(\frac{\pi}{2}\right)$ for every p is given in Equation (2.74).

A plot of $f\left(\frac{\pi}{2}\right)$ for $p > 2$ based on Equation (2.74) is shown in Figure 2.25. Plots of the numerator (green) and the denominator (black) of $f\left(\frac{\pi}{2}\right)$ for $p > 2$ are given in Figure 2.26. Referring to the numerator of Equation (2.74), $\frac{2p-3}{2p-2}$

gives positive integers for $p > 2$, where $\frac{2p-3}{2p-2} \in (0, +\infty)$. From that it follows, the numerator of Equation (2.74), $\sqrt{\pi}\Gamma\left(\frac{2p-3}{2p-2}\right) \in (0, +\infty)$ for $p > 2$. While, from the denominator of Equation (2.74), $\frac{3p-4}{2p-2}$ as well gives positive integers for $p > 2$, where $\frac{3p-4}{2p-2} \in (0, +\infty)$. Therefore, the denominator of Equation (2.74), $(\alpha\kappa_0^p)^{\frac{1}{p-1}} 2\Gamma\left(\frac{3p-4}{2p-2}\right) \in (0, +\infty)$. From Equation (2.77), $g\left(\frac{\pi}{2}\right)$ is bounded because exponent of $\cos\theta$ is greater than 0 for every $p > 2$. The tip geometry is relevant for $p > 2$.

As an example in this case, we choose $p = 4$ and substituting it in Equation (2.66) and Equation (2.69) respectively yields

$$f(\theta) = \frac{1}{(\alpha\kappa_0^4)^{\frac{1}{3}}} \int_0^\theta (\cos\phi)^{\frac{2}{3}} d\phi, \tag{2.99}$$

and

$$g(\theta) = -\frac{1}{(\alpha\kappa_0^4)^{\frac{1}{3}}} \int_0^\theta \frac{\sin\phi}{\cos\phi^{\frac{1}{3}}} d\phi. \tag{2.100}$$

A parametric plot of Equation (2.99) and Equation (2.100) is shown in Figure 2.27.

The "tip radius" given by Equation (2.99) is

$$\lim_{\theta \to \frac{\pi}{2}} f(\theta) \approx \Gamma\left(\frac{5}{6}\right). \tag{2.101}$$

While, the "tip length" in Equation (2.100) is

$$\lim_{\theta \to \frac{\pi}{2}} g(\theta) = -\frac{3}{2}. \tag{2.102}$$

In Figure 2.28, we show a plot showing the tip shape for various values of p for $p > 2$. Such plot simply describes how p alters the tip shape when $p > 2$.

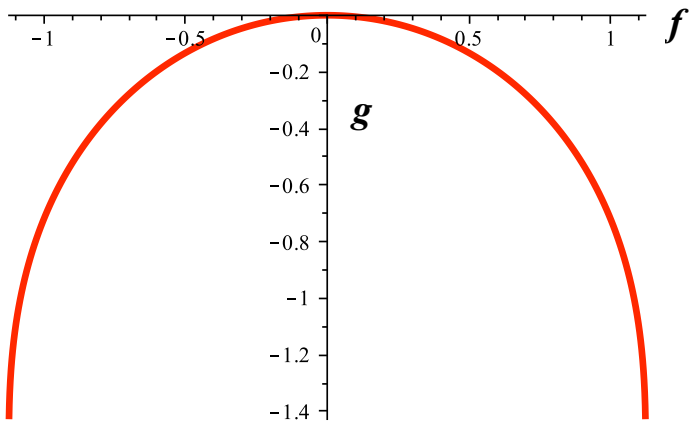

Figure 2.27: A plot of $(f(\theta), g(\theta))$ for $p = 4$, $0 \leq \theta \leq \frac{\pi}{2}$, $\alpha = \kappa_0 = 1$ as given by Equation (2.99) and Equation (2.100) based on the general expressions of Equation (2.66) and Equation (2.69).

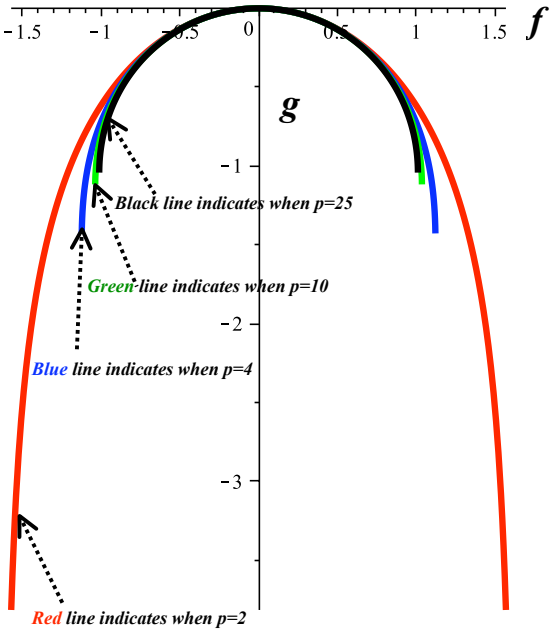

Figure 2.28: A parametric plot showing the tip shape for various values of p for $p > 2$.

Case 7: $p \to \infty$

We consider the extreme case $p \to \infty$. This models the case where the wall building material deposition is almost totally focused to areas of curvature $\kappa \geq 1$

with almost no deposition for $\kappa < 1$.

Taking $p \to +\infty$ for $f(\theta)$ in Equation (2.66) yields

$$\lim_{p\to\infty} f(\theta) = \lim_{p\to\infty} \left(\frac{1}{(\alpha\kappa_0^p)^{\frac{1}{p-1}}} \int_0^\theta (\cos\phi)^{\frac{p-2}{p-1}} d\phi \right), \tag{2.103}$$

$$= \lim_{p\to\infty} \left(\int_0^\theta (\cos\phi)^{\frac{1-2/p}{1-1/p}} d\phi \right), \tag{2.104}$$

$$= \sin\theta. \tag{2.105}$$

Similarly, for $g(\theta)$ in Equation (2.69) is

$$\lim_{p\to\infty} g(\theta) = -\lim_{p\to\infty} \left(-\frac{1}{(\alpha\kappa_0^p)^{\frac{1}{p-1}}} \int_0^\theta \frac{\sin\phi}{(\cos\phi)^{\frac{1}{p-1}}} d\phi. \right), \tag{2.106}$$

$$= -\lim_{p\to\infty} \left(\int_0^\theta (\sin\phi) d\phi \right), \tag{2.107}$$

$$= -1 + \cos\theta. \tag{2.108}$$

Both Equation (2.105) and Equation (2.108) show that they are bounded when $\theta = \frac{\pi}{2}$.

Furthermore, taking $p \to +\infty$ for $f\left(\frac{\pi}{2}\right)$ and $g\left(\frac{\pi}{2}\right)$ in Equation (2.74) and Equation (2.77), respectively, yields

$$\lim_{p\to\infty} f\left(\frac{\pi}{2}\right) = 1, \tag{2.109}$$

and

$$\lim_{p\to\infty} g\left(\frac{\pi}{2}\right) = -1. \tag{2.110}$$

Both Equation (2.109) and Equation (2.110) show that the tip geometry is relevant for $p \to +\infty$.

From Equation (2.105), the "tip radius" is

$$\lim_{\theta \to \frac{\pi}{2}} f(\theta) \quad = \quad f\left(\frac{\pi}{2}\right) = 1. \tag{2.111}$$

From Equation (2.108), the "tip length" is

$$\lim_{\theta \to \frac{\pi}{2}} g(\theta) \quad = \quad g\left(\frac{\pi}{2}\right) = -1. \tag{2.112}$$

A parametric plot of Equation (2.105) and Equation (2.108) is shown in Figure 2.29.

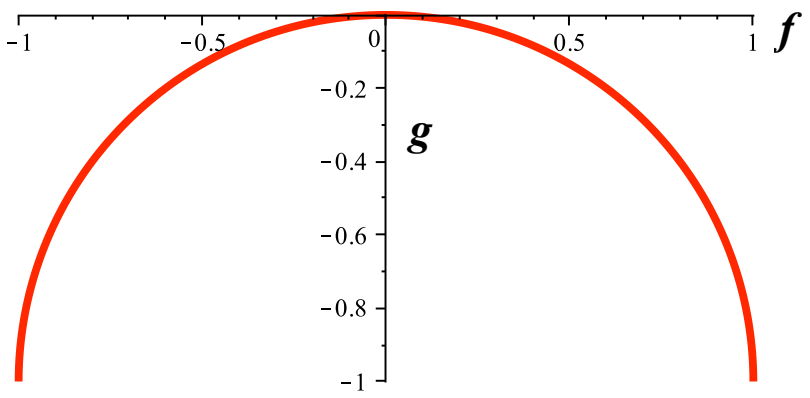

Figure 2.29: A plot of $(f(\theta), g(\theta))$ for $p \to +\infty$, $0 \leq \theta \leq \frac{\pi}{2}$, $\alpha = \kappa_0 = 1$ as given by Equation (2.101) and Equation (2.104) based on the general expressions of Equation (2.66) and Equation (2.69).

2.8 Full 3-D Geometrical Model

First off, recall that the incorporation of wall-building material is given by Equation (2.53) and then is further assumed by Equation (2.54), that is,

$$\frac{s_t f_s}{f} + \frac{\lambda_t}{\lambda} \quad = \quad N_0 n(s,t). \tag{2.113}$$

Since $\frac{\lambda_t}{\lambda} = \theta_s U_0 \cos\theta$ and $s_t = U_0 \sin\theta$ and substituting all these in Equation (2.113) yields

$$\cos\theta\left(\frac{\sin\theta}{f} + \theta_s\right) = \frac{1}{\alpha} n(s,t). \tag{2.114}$$

Note that $\alpha = \frac{U_0}{N_0}$ and the bracketed term on the left-hand side of Equation (2.114), $\frac{\sin\theta}{f} + \theta_s$ represents sum of the latitudinal curvature, k, and the longitudinal curvature, κ. In fact, sum of k and κ represents mean curvature, K_m, at a point on the axisymmetric tip surface. Simplifying Equation (2.114) yields

$$K_m \cos\theta = \frac{1}{\alpha} n(s,t). \tag{2.115}$$

Since f is unknown, rewriting Equation (2.115) leads to the following system

$$\theta_s = \frac{1}{\alpha} n(s,t) \sec\theta - \frac{\sin\theta}{f}, \tag{2.116}$$

$$f_s = \cos\theta, \tag{2.117}$$

with boundary conditions $\lim_{s\to 0}(\theta, f) = (0,0)$ and $\lim_{s\to\infty}(\theta, f) = \left(\frac{\pi}{2}, f_\infty\right)$, where f_∞ is the asymptotic radius of the tip.

The wall-building material deposition, $n(s,t)$, must be set to zero along the flat surface of the tip and increase of $n(s,t)$ implies increase of the curvature. The surface is described by both mean and *Gaussian* curvatures, K_m and K_g, respectively, in which $K_m = \frac{\kappa + k}{2}$ and $K_g = \kappa k$. Geometrically, $K_m \neq 0$ along the flat surface because $k \neq 0$. Obviously, $K_g = 0$ along the flat surface. Following [31], we have

$$n(s,t) = K_g N(K_m, K_g), \tag{2.118}$$

where $N(K_m, K_g)$ describes the wall assembly. Subsequently, $N(K_m, K_g)$ is chosen to be a constant 1, which yields $n(s,t) \propto K_g$. Expanding the right-hand side of Equation (2.118) yields

$$n(s,t) \;=\; \frac{K_g}{K_0} = \frac{1}{K_0}\frac{\theta_s \sin\theta}{f}, \tag{2.119}$$

where K_0 is a radius of *Gaussian* curvature and assumed to be 1, used to produce tip shapes figuratively

2.8.1 Computation of Full 3-D Geometrical Model

Substituting the right-hand side Equation (2.119) in the right hand-side of Equation (2.116) gives

$$\theta_s \;=\; \frac{1}{f}\left(\frac{1}{\alpha}\frac{1}{K_0}\theta_s \sin\theta \sec\theta - \sin\theta\right). \tag{2.120}$$

Simplifying Equation (2.120) yields

$$\cos\theta f + \frac{df}{d\theta}\sin\theta \;=\; \frac{\sin\theta}{\alpha K_0}, \tag{2.121}$$

which is called the *Bernoulli*'s equation. Dividing Equation (2.121) by $\sin\theta$ gives

$$\cot\theta f + \frac{df}{d\theta} = \frac{1}{\alpha K_0}. \tag{2.122}$$

Note that a general solution of Equation (2.122) is given by

$$f = e^{-\int \cot\theta d\theta}\int\left(\frac{1}{\alpha K_0}\right)e^{\int \cot\theta d\theta}d\theta + ce^{-\int \cot\theta d\theta}, \tag{2.123}$$

where c is a constant. Solving Equation (2.123) yields

$$f(\theta) = \frac{1}{\alpha K_0}\left(\frac{c\alpha K_0 - \cos\theta}{\sin\theta}\right). \tag{2.124}$$

Let $c\alpha K_0 = 1$ which stems from $f(0) = 0$ and substituting it in Equation (2.124) gives

$$f(\theta) \;=\; \frac{1}{\alpha K_0}\left(\frac{\sin\theta}{\cos\theta + 1}\right), \tag{2.125}$$

where the bracketed term on the right-hand side of Equation (2.125) is equivalent to $\tan\frac{\theta}{2}$ and it will be used later on.

Next is the derivation of κ, which begins by the following chain rule

$$\frac{df}{d\theta} \;=\; \frac{df}{ds}\frac{ds}{d\theta}. \tag{2.126}$$

Substituting derivative of Equation (2.125) with respect to θ and Equation (2.117) in Equation (2.126) and simplifying it yields

$$\frac{1}{\kappa} \;=\; \frac{1}{\alpha K_0(\cos\theta + 1)}\frac{1}{\cos\theta},$$

which, then gives

$$\kappa \;=\; \alpha K_0 \cos\theta(\cos\theta + 1). \tag{2.127}$$

Alternatively, it is much simpler to substitute the left-hand side of Equation (2.126) with $\frac{1}{\alpha\kappa_0} - \cot\theta f$ given by Equation (2.122), which results in Equation (2.127).

The derivation of k is done by substituting Equation (2.125) in Equation (2.45), namely,

$$k = \frac{\sin\theta}{f}, \tag{2.128}$$

$$= \frac{\sin\theta}{\frac{\sin\theta}{\alpha\kappa_0(\cos\theta+1)}}, \tag{2.129}$$

which then gives

$$k = \alpha K_0(\cos\theta + 1). \tag{2.130}$$

Furthermore, on setting $K_0 = K_g(0) = \kappa(0)k(0) = 4\alpha^2 K_0^2$ gives $K_0 = \frac{1}{4\alpha^2}$ [31].

The derivation of $g(\theta)$ starts with the following chain rule

$$\frac{dg}{d\theta} = \frac{dg}{ds}\frac{ds}{d\theta}. \tag{2.131}$$

Substituting $\frac{dg}{ds} = -\sin\theta$ and Equation (2.127) in Equation (2.131)

$$\frac{dg}{d\theta} = \frac{-\sin\theta}{\alpha K_0 \cos\theta(\cos\theta + 1)}. \tag{2.132}$$

Solving Equation (2.132) yields

$$g(\theta) = \frac{1}{\alpha K_0} \ln\left(\frac{\cos\theta}{\cos\theta + 1}\right). \tag{2.133}$$

Note that an equivalent chain rule for Equation (2.131) is $\frac{dg}{d\theta} = \frac{dg}{df}\frac{df}{d\theta}$, which solving it results in Equation (2.133).

Finally is the derivation of the tip shape in terms of Cartesian coordinates. From that it first follows the chain rule given by

$$\frac{dg}{df} = \frac{dg}{d\theta}\frac{d\theta}{df}, \tag{2.134}$$

where $\frac{dg}{d\theta} = \frac{dg}{ds}\frac{ds}{d\theta} = -\frac{\sin\theta}{\alpha K_0 \cos\theta(\cos\theta+1)}$ and $\frac{df}{d\theta} = \frac{df}{ds}\frac{ds}{d\theta} = \frac{1}{\alpha K_0(\cos\theta+1)}$ and substituting them in the right hand-side of Equation (2.133) yields

$$\frac{dg}{df} = -\tan\theta. \tag{2.135}$$

From Equation (2.135), $dg = -\tan\theta df$ and so θ should be in terms of f. Refering Equation (2.124), $\frac{\theta}{2} = \tan^{-1}(\alpha K_0 f)$. Based on $\tan\left(\frac{\theta}{2}+\frac{\theta}{2}\right) = \frac{2\tan\frac{\theta}{2}}{1-\tan^2\frac{\theta}{2}}$ and so $dg = \frac{-2\tan\frac{\theta}{2}}{1-\tan^2\frac{\theta}{2}}df$. Since $\frac{\theta}{2} = \tan^{-1}(\alpha K_0 f)$ and so $2\tan(\tan^{-1}(\alpha K_0 f)) = 2\alpha K_0 f$ and $\tan^2(\tan^{-1}(\alpha K_0 f)) = (\alpha K_0 f)^2$. Substituting all these in Equation (2.135) and solving it yields

$$g = \frac{1}{\alpha K_0}\ln(1-(\alpha K_0 f)^2). \tag{2.136}$$

Substituting $K_0 = \frac{1}{4\alpha^2}$ gives

$$g = 4\alpha \ln\left(1-\frac{f^2}{16\alpha^2}\right), \tag{2.137}$$

and it is equivalent to $y = 4\alpha\ln\left(1-\frac{x^2}{16\alpha^2}\right)$.

A parametric plot Equation (2.125) and Equation (2.133) with $N = 1$ is shown in Figure 2.30.

2.9 Extension of Full 3-D Geometrical Model

Recall that from Equation (2.115), we have $K_m\cos\theta = \frac{1}{\alpha}n(s,t)$, where $n(s,t) = K_g N(K_m, K_g)$. Subsequently, we choose $N = K_m\cos\theta = \kappa\cos\theta + k\cos\theta$, which models as follows:

- At distal region of the tip, the wall-building material deposition does not occur. Based on Figure 2.6, distal region is represented when $\theta = \frac{\pi}{2}$ and so $N = 0$ because $\cos\left(\frac{\pi}{2}\right) = 0$, and

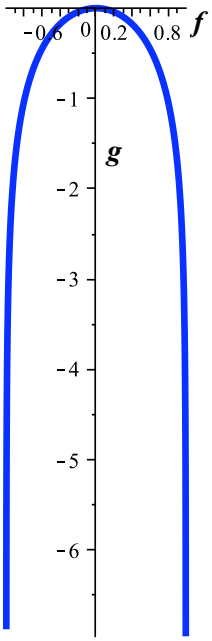

Figure 2.30: A plot of $(f(\theta), g(\theta))$, $0 \leq \theta \leq \frac{\pi}{2}$, $\alpha = \kappa_0 = 1$ as given by Equation (2.125) and Equation (2.133), where $N = 1$.

- At the apex, the wall-building material deposition is maximum, where $0 \leq \theta < \frac{\pi}{2}$. From that it follows $N \neq 0$ because $\cos 0 = 1$, $\kappa =$ maximum and $k \neq 0$, which gives $n \neq 0$, that is, assumed to be maximum.

Substituting $N = K_m \cos\theta$ in the right hand-side of Equation (2.115) yields

$$K_m \cos\theta = \frac{1}{\alpha K_0} K_g K_m \cos\theta, \tag{2.138}$$

$$K_g = \alpha K_0. \tag{2.139}$$

Since $K_g = \kappa k$, $\kappa = \frac{d\theta}{ds}$ and $k = \frac{\sin\theta}{f}$, by substituting all these in left-hand side of Equation (2.139) gives

$$f\frac{df}{d\theta} = \frac{1}{\alpha K_0} \cos\theta \sin\theta. \tag{2.140}$$

Integrating both sides of Equation (2.140) gives

$$f(\theta) = \frac{\sin\theta}{\sqrt{\alpha K_0}}. \tag{2.141}$$

For the longitudinal curvature κ, using the chain rule, namely, $\kappa = \frac{d\theta}{df}\frac{df}{ds}$, so we have $\frac{d\theta}{ds} = \kappa$. While, the latitudinal curvature $k = \frac{\sin\theta}{f} = \sqrt{\alpha K_0}$. By setting $K_0 = K_g(0)$, we have $K_0 = \alpha K_0$.

To get $g(\theta)$, use the chain rule $\frac{dg}{d\theta} = \frac{dg}{df}\frac{df}{d\theta}$ (or equivalently $\frac{dg}{d\theta} = \frac{dg}{ds}\frac{ds}{d\theta}$) and from that it follows:

$$\frac{dg}{d\theta} = -\frac{\sin\theta}{\sqrt{\alpha K_0}}, \tag{2.142}$$

$$g(\theta) = \frac{1}{\sqrt{\alpha K_0}}(\cos\theta - 1). \tag{2.143}$$

Finally is the derivation of the tip shape in terms of Cartesian coordinates. From that it first follows the chain rule given by

$$\frac{dg}{df} = \frac{dg}{d\theta}\frac{d\theta}{df}, \tag{2.144}$$

$$dg = -\tan\theta df. \tag{2.145}$$

Referring to Equation (2.141), we get $\theta = \sin^{-1} f\sqrt{\alpha K_0}$ and substituting it in Equation (2.145) yields

$$g(f) = -\frac{\sqrt{1-f^2} + f^2 - 1}{\sqrt{1-f^2}}, \tag{2.146}$$

which is equivalent to $y(x) = -\frac{\sqrt{1-x^2}+x^2-1}{\sqrt{1-x^2}}$.

A parametric plot of Equation (2.141) and Equation (2.143) with $N = K_m\cos\theta$ is shown in Figure 2.31.

Figure 2.32 shows a comparison full 3-D models,when $N = 1$(blue) and when $N = K_m\cos\theta$ (red).

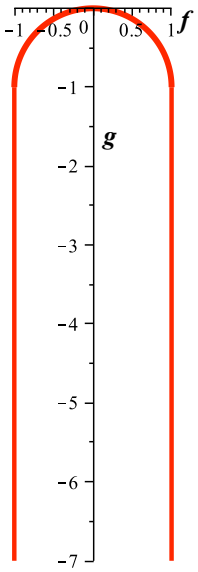

Figure 2.31: A plot of $(f(\theta), g(\theta))$, $0 \leq \theta \leq \frac{\pi}{2}$, $\alpha = \kappa_0 = 1$ as given by Equation (2.141) and Equation (2.143), where $N = K_m \cos\theta$.

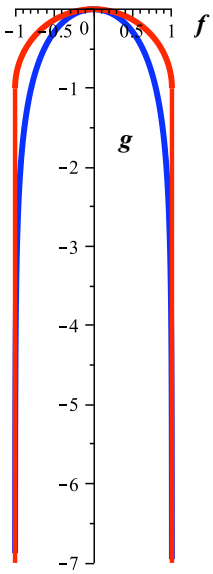

Figure 2.32: A comparison full 3-D models,when $N = 1$(blue) and when $N = K_m \cos\theta$ (red).

2.10 Summary

A geometrical model for the role of the Spitzenkorper in tip growth was proposed by [7]. This model predicts that a moving Spitzenkorper releases exocytic vesicles in all directions and this is hypothesized to be a key for the shape formation

of apical dome. A geometrical equation called hyphoid equation was derived to describe such tip formation that relates deposition of exocytic vesicles per unit time, n, with speed of the VSC, U_0. Although the hyphoid equation does produce a remarkably good fit to images of hyphal tips, a number of problems with the derivation of hyphoid equation were pointed out by [50]. We suggest that the derivation can be revised as follows: maximum deposition of wall-building materials takes place when the change in arc length per unit angle is maximum. Deposition of wall-building materials is associated to tip curvature, namely, curvature equal to the reciprocal of its radius (the distance from the shape-organising center to the tip).

We then study two types of geometrical models proposed by [31]. The first considers deposition of wall-building materials associated to principal curvatures of the tip. When deposition of wall-building materials is proportional to longitudinal curvature, we give a generalized formulae for the tip shape and from that, we examine localization of deposition of wall-building materials. We observe that not every generated tip is biological plausible. When deposition of wall-building materials is associated to longitudinal and latitudinal curvatures, we showed that it is possible to derive a new relationship in generating tip shape.

Chapter 3

Biomechanical Model

3.1 Introduction

Hyphal tip growth of filamentous cells can be modeled by mathematically formulating mechanical processes experienced by a growing hypha. This helps to provide a much better insight of the morphology and mechanical description of the growth.

Here we examine a biomechanical model of hyphal tip growth proposed by [36] (see [32, 33, 34, 35] for details). This framework is based on nonlinear elasticity theory for shells coupled with a simple representation of growth. Construction of this model involves three main components: (i) hyphal tip geometry, (ii) mechanical equilibirium and (iii) constitutive relationships.

Hyphal tip geometry is represented as a 2-D axisymmetric elastic shell. Growth is assumed to be driven by pressure, namely, deposition of wall-building materials is proportional to internal pressure. The growth mechanism is modeled by a process of incremental elastic growth in which the cell wall responds elastically to the continuous addition of new material [36].

Using nonlinear elasticity theory, this model is capable of producing a tip-like shape and capture its essential mechanical features. It demonstrates that the

newly grown tip looks like a translation of the tip shape at the previous grown tip, namely, self-similar tip propagation. Also, effect of surface friction and the hypothesis of orthogonal growth proposed by [67] in 1892 are examined. Following that, it is suggested that as friction increases, the trajectories of material points tend to align with what would be the equivalent orthogonal trajectories on the tip surface. This is in good agreement with experimental results in [14].

In this Chapter, we examine the effect of varying a paramter denoted by σ_1, namely, arc length of the stretchable region on tip shape. We observe that by varying σ_1, it leads to either a narrower or a broader tip shape. This might suggest that σ_1 can be a factor contributing to geomerty of the tip shape. To our knowledge, varying σ_1 has not been discussed before. Another result given in this Chapter relates to a function known as the effective pressure profile, $q_n^{(eff)}$. The profile $q_n^{(eff)}$ shows a softer material response can be interpreted as an increase in turgor pressure and a rigid material response can be interpreted as a decrease in turgor pressure. We consider evolution of self-similar tip propagation using $q_n^{(eff)}$. We describe variation in pressure for a hypha profile and also the effective pressure profile using a figurative representation. Our final study is an examination on the effect of surface friction and the hypothesis of orthogonal growth being focused only on the apex of what the equivalent germ tube.

This chapter begins with a few general points on mechanical equilibrium, then definitions used in this work followed by systems of equations adopted properly as a main part of the model construction, the computer simulation technique used to generate the tip shape and finally on our results.

3.2 Overview of Mechanical Equilibrium

A few general points when an object in mechanical equilibrium are given as follows [74]:

- The net external force, $\underline{F}$, must be zero, namely, $\Sigma\underline{F} = 0$, and
- The net external torque, $\tilde{\tau}$, must be zero, namely $\Sigma\tilde{\tau} = 0$.

The first condition is a statement of translational equilibirium: The sum of all forces acting on the object must be zero, so the object has no translational acceleration. The second condition is a statement of rotational equilibirium: The sum of all torques on the object must be zero, so the object has no angular acceleration. In much more simpler words, the object is in the state of rest or balance due to equal action of two or more opposite forces.

In [36], it employed a formalism for describing the dynamics of thin shells that was developed earlier for biomembranes by [25]. This is actually the same formalism as is often used to descirbe the inflation of a balloon. It assumes that mechanical equilibirium is maintained througout [47]. At the level of mechanical equilibrium, one simply writes down the balance between the total normal stress and the total applied force whatever its origin is [35, 36]. All that the wall 'senses' is the total normal force acting on the tip.

3.3 Definitions

3.3.1 Elastic Shell

A shell is a 2-D sheet of small but finite thickness that can support bending moments [35].

3.3.2 Coordinate systems

A constant supply of wall-building materials into the tip is necessary in order to maintain growth. Deposition of wall-building materials is then followed by mechanical changes to the tip and thus the tip deforms. Hyphal growth is focused

at its apical region and so a material point, σ, on the tip surface is considered. The deformation of the tip changes the position of σ.

To describe deformation of a continuum requires two Cartesian coordinate systems. The tip is initially represented by a reference configuration. After the tip goes through deformation, σ changes its position and so assumes a new current configuration.

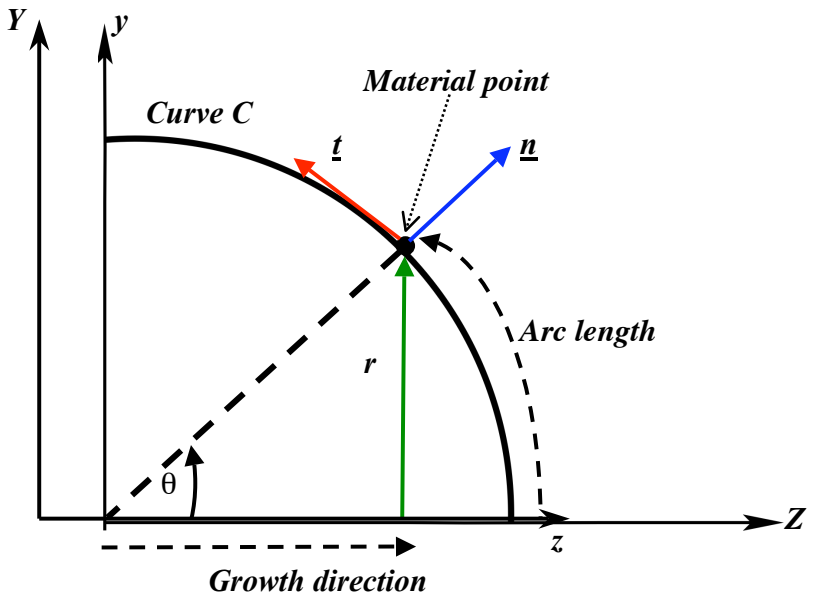

Figure 3.1: The medial section, C, of a generic hyphal tip. Only half the section is shown for clarity. For a given material point, σ, arc length, $s(\sigma)$, is measured from the apex of the shell to that point, $r(\sigma)$ is the radial distance from the z-axis to that point and $\underline{\mathbf{n}}$ and $\underline{\mathbf{t}}$ denotes the normal and tangent vectors, respectively. The angle, $\theta(s)$, is the angle between the normal direction and the z-axis. Redrawn from [36].

Figure 3.1 shows a basic description of the hyphal tip geometry, where half the medial section of hyphal filament, C, is considered. The reference configuration is described by (Y, Z) coordinates and the current configuration by (y, z) coordinates. As shown by Figure 3.1, a growing hyphal filament is modeled by assuming that it is axisymmetric about the z-axis in the (y, z)-plane. To get a basic 3-D representation of the tip, the profile C is rotated about the z-axis

through an angle of 2π shown in Figure 3.2.

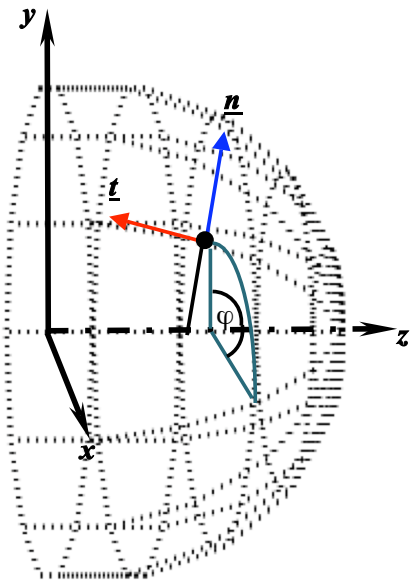

Figure 3.2: Corresponds to Figure 3.1, a basic 3-D representation of the tip, the profile C is symmetrically rotated about the z-axis through an angle of 2π, where φ is the azimuthal angle.

3.3.3 Describing The Tip Shape

Here we describe the tip shape before and after deformation, which is represented in terms of arc length, s, and radial distance, r.

Arc length, s, is a function of σ, namely, $s = s(\sigma)$. For a given σ, s is measured from the apex of the shell to σ. Before deformation or growth, the material parameter, σ, is identified with the arc length [34].

Radial distance, r, is a function of σ, namely, $r = r(\sigma)$. For a given σ, r is measured from the z-axis to σ. Before deformation or growth, r is identified by, $\rho(\sigma)$. The variable ρ is represented in terms of the deformation variables and will be discussed in the subsequent section.

In the light of the description above, the tip shape in the initial configuration is $(\sigma, \rho(\sigma))$. The tip shape in the current configuration is $(s(\sigma), r(\sigma))$.

3.3.4 Deformation Variables

It is assumed that deposition of the wall-building materials together with the internal pressure acting on the tip causes the tip to stretch. This involves two types of stretching, namely, the longitudinal stretching, α_s, and the latitudinal stretching, α_φ. (Note that α_s was denoted by λ in Chapter 2). These variables are defined by

$$\alpha_s := \frac{\partial s}{\partial \sigma}, \tag{3.1}$$

and

$$\alpha_\varphi := \frac{r(\sigma)}{\rho(\sigma)}. \tag{3.2}$$

At a given σ, the variable α_s corresponds to the extensional stretch of arc length. While, the variable α_φ corresponds to the radial stretch.

Another deformation variable is, α_3, measuring changes in the normal thickness of the shell, which is related to α_s and α_φ and is defined by

$$\alpha_3 = \frac{1}{\alpha_s \alpha_\varphi}, \tag{3.3}$$

which in turn comes from the incompressibility condition for the shell, namely, $\alpha_s \alpha_\varphi \alpha_3 = 1$ (see [32, 36] for details). Based on the formulation given by (3), as growth continues and thus the tip continuously stretches, α_s and α_φ increase and this leads to a small value of α_3. In [47], it explained that the thickness of the cell wall is here assumed to be very small compared to the dimensions of the cell as a whole that it can be approximated by an infinitely thin shell. So the approximation of assuming a constant wall thickness seems a reasonable one.

Figure 3.3 shows directions of longitudinal and latitudinal stretches and thickness of the cell wall in terms of a 3-D figurative representation.

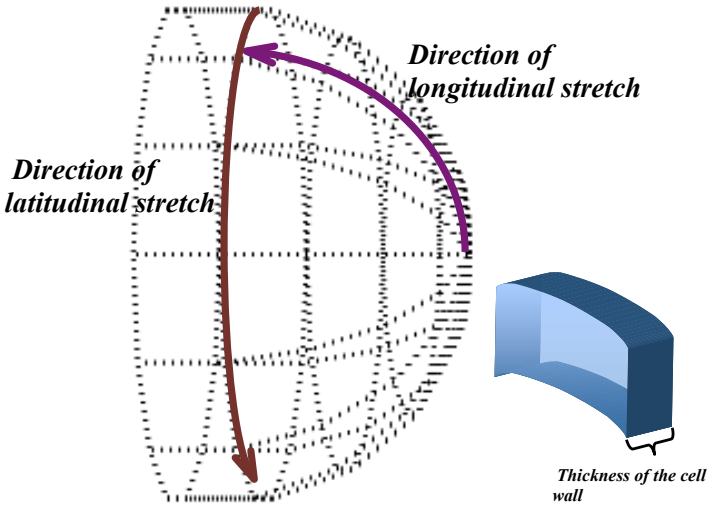

Figure 3.3: Basic illustration of thickness of the cell wall, directions of longitudinal and the latitudinal stretching acting on the tip surface; α_3, α_s and α_φ, respectively.

3.3.5 Mechanical Parameters

Forces

As with all vectorial quantities, forces could be resolved into components: in the case of an axisymmetric shell these are the force components normal to the shell surface and the forces tangential to the surface [35].

The soft tip is stretched by internal forces and thus driven forward. A combination of internal pressure, the developing cytoskeleton and the structure of the cell wall itself make up the driving forces [21]. However, in this model, the origins of those forces are not considered.

Pressure

Pressure is the perpendicular component of force, F_n, per unit area, exerted on the surface of an object, defined by $\frac{F_n}{Area}$. Pressure is a scalar. There is no direction associated with pressure, but the direction of the force associated with the pressure is perpendicular to the surface of interest.

The internal pressure, which in the case of cells is the turgor pressure [35] and results from the hydrostatic pressure due to the difference between the intracellular and extracellular osmotic pressures. This model is pressure difference driven, where pressure difference is denoted by ΔP. There is a debate as to how the tip is actually driven forward. However, experimental results suggest that turgor pressure is a main player. Moreover, a considerable amount of modelling has been developed, where the turgor pressure is assumed to play some role as discussed in detail in [5, 20, 66]. Again, we emphazie that in this model, what matters is that the tip 'senses' the turgor pressure.

Stress

Stress is defined by the force, $\underline{\mathrm{F}}$, exerted on an object per unit cross-sectional area, defined by $\frac{\underline{\mathrm{F}}}{Area}$. Classification of stress depends on the direction of the force acting on the object and so it is a vector quantity.

In this model, note that stresses are with units of force per unit length. Following is stresses of interest exerted on the tip surface that are considered in this model :

- Magnitude of the longitudinal and latitudinal stresses are denoted by t_s and t_φ, respectively, where, *total stress* $= t_s\underline{\mathrm{t}} + t_\varphi\underline{\mathrm{n}}$. The stress t_s on the surface is along the tangent vector, $\underline{\mathrm{t}}$, in the direction of increasing arc length. The stress t_φ is in the direction of increasing azimuthal angle, φ. Figure 3.4 shows directions of longitudinal and latitudinal stresses.

- Magnitude of the tangential and normal shear stresses are denoted by τ_s and q_s, respectively, where, *total shear stress* $= \tau_s\underline{\mathrm{t}} + q_s\underline{\mathrm{n}}$. Note that these stresses are subjected to the position of σ before and after deformation. The stress τ_s corresponds to the friction between the cell surface and the burrowing medium such as soil in the quest for nutrients. The stress q_s

corresponds to the internal pressure. Figures 3.5 and 3.6 show tangential and normal shear stresses, respectively, subjected to the position of σ before and after deformation.

- Magnitude of the total normal stress exerted on the shell is denoted by q_n. The turgor pressure (pressure difference) is a purely normal stress and it is assumed that $q_n = \Delta P$.

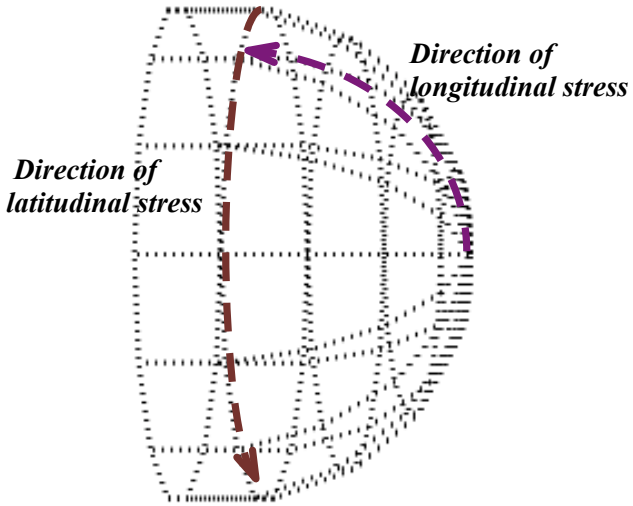

Figure 3.4: Basic illustration of the longitudinal and the latitudinal stresses acting on the tip surface; t_s and t_φ, respectively.

Bending moments

A moment is a force that acts on an object that has a fixed point which tends to twist or rotate the object. Magnitude of the longitudinal and latitudinal moments are denoted by m_s and m_φ, respectively, where, *total bending moment* = $m_s\underline{\mathrm{t}} + m_\varphi\underline{\mathrm{n}}$. In this model, bending moments are assumed to be isotropic.

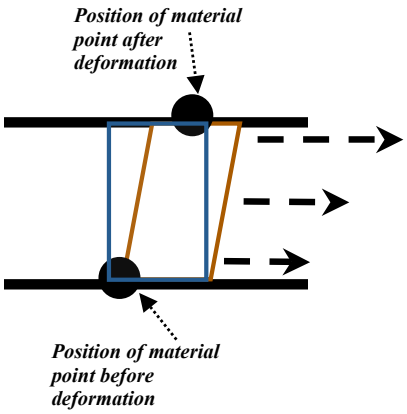

Figure 3.5: Basic illustration of the tangential shear stress acting on the tip surface; τ_s. Arrows represents the tangential shear forces in response to surface friction.

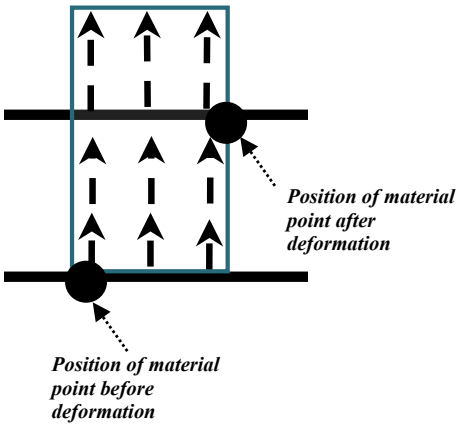

Figure 3.6: Basic illustration of the normal shear stress acting on the tip surface; q_s. Arrows represents the normal shear forces in response to turgor pressure.

Note:

The geometric variables satisfy the equations:

$\frac{dr}{ds} = \cos\theta$ and $\frac{dy}{ds} = -\sin\theta$.

The principal curvatures of the shell are given by:

$\kappa_s = \frac{d\theta}{ds}$ and $\kappa_\varphi = \frac{\sin\theta}{r}$.

All of these have already discussed in Chapter 2, in which κ_s was denoted by κ and κ_φ was denoted by k.

3.3.6 *Young-Laplace* Equation

This model uses physics of science interface in order to capture the mechanical equilibirium of the cell. Examples of such science interface include bubble soap and the inflation of a balloon.

Following is a brief overview of physics of science interface [51]:
Static shapes of surfaces (namely, state of equilibrium) that contain a liquid are governed by the normal stress balance across the surface, mathematically described by the *Young-Laplace* equation.

If an interface between two fluids is curved, there is a pressure difference across it provided the system is in equilibirium. Lets consider a circular part of the surface. The surface tension tends to minimize the area. This results in a planar geometry of the surface. In order to curve the surface, the pressure on one side (internal pressure) must be larger than on the other side (external pressure).

Shortly, provided that the system is in equilibrium, the *Young-Laplace* equation is generally defined in the following form:

$$\textit{Pressure Difference} \quad = \quad (\textit{Surface Curvature}) \cdot (\textit{Surface Tension}),$$

where $\textit{Pressure Difference} = \textit{Internal Pressure} - \textit{External Pressure}$. This equation indicates that the pressure inside a spherical surface is always greater than the pressure outside, but the difference decreases to zero as the radius of curvature becomes infinite (when the surface is flat). In contrast, the pressure difference increases if the radius of the curvature becomes smaller.

3.4 Systems of Equations

Different approaches have been proposed to model tip growth biomechanically, namely, achieving irreversible extension. The plasticity theory, for example, is an approach that has been used for cells ranging from plant cells to root hairs. In [23], a hypha is

represented as a plastically deforming dome whose equator is attached to a nongrowing cylinder of fixed radius. Both the dome and the cylinder are maintained at a prescribed constant thickness. As the tip advances forward under plastic deformation the equatorial line, where the dome and cylinder join is moved forward to follow the advance of the tip. The "growth" is represented in such a way that the deformed meridian is (numerically) remeshed with uniformly spaced points; thereby redefining the arc-length for the "next" propagation step (see [23] for details).

The equations for mechanical equilibrium in this work is for axisymmetric shells as proposed by [25]. Equations proposed by [25] have been widely used to model curved biomembranes as disscussed, for example, by [72, 73, 80]. The novelty of the approaches adopted in this work is to use the techniques of nonlinear elasticity. These techniques enable one to follow large deformation of the cell and to model the actual growth mechanism by an incremental process in which mass is added to the elastically strained cell [32]. In this work, the "growth" of the elastically deforming tip is represented by a reparameterization of the meridional space curve representing the tip profile, namely, a space-curve reparameterization. Such approach shows that it is possible to formulate quite general mechanical models based on nonlinear elasticity theory that, when combined with an appropriate growth mechanism, can describe the morphology and mechanics of a wide variety of growing filamentous cells. The 'morphoelastic' description proposed by [36] is capable of describing many of the observed features of hyphal growth, and that the addition of biophysical information about the cell wall structure can give further insights into the growth process and given sufficient information about the cell wall structure, help to distinguish details of the growth in different filamentous cells.

3.4.1 Mechanical Equilibrium

Newton's laws are used to balance the stresses. At the level of mechanical equilibrium, this model considers the balance between the total of normal stresses and the total applied force whatever its origin is [35].

At a given σ on the tip surface, an applied force acting at σ is followed by body force. Applied forces are related to turgor pressure and surface friction between the tip surface and its burrowing environment. Turgor pressure acting on σ yields the shear stress normal to σ. Surface friction acting on σ yields the tangential stress at σ.

The mechanical equilibrium, including bending moments and external tangential stresses corresponding to a surface frictional effect, is governed by a complex set of differential equations representing the balance of stresses, defined by [36, 25]

$$\frac{1}{r}\frac{d(rq_s)}{ds} = q_n - (\kappa_s t_s + \kappa_\varphi t_\varphi), \tag{3.4}$$

$$\frac{1}{r}\frac{d(rt_s)}{ds} = \frac{\cos\theta}{r} t_\varphi + \kappa_s q_s - \tau_s, \tag{3.5}$$

$$\frac{1}{r}\frac{d(rm_s)}{ds} = \frac{\cos\theta}{r} m_\varphi + q_s. \tag{3.6}$$

Rewriten Equation (3.4) as

$$\frac{1}{r}\frac{d(rq_s)}{ds} + \kappa_s t_s + \kappa_\varphi t_\varphi = q_n. \tag{3.7}$$

Equation (3.7) is a mathematical statement of balance of normal stresses. As we mentioned earlier that for a pressurized shell, $q_n = \Delta P$. This is the *Young-Laplace* equation in which the left-hand side of Equation (3.7) respresents a general form: *Surface curvature* $\cdot$ *Surface stress*.

Rewritten Equation (3.5) as

$$\frac{1}{r}\frac{d(rt_s)}{ds} - \frac{\cos\theta}{r} t_\varphi - \kappa_s q_s = -\tau_s, \tag{3.8}$$

Equation (3.8) is a mathematical statement of balance of tangential stresses acting at a given σ on the tip surface subjected to the surface friction between a growing hypha and its external environment. Note that, previously in [33], Equation (3.8) is given by $\frac{1}{r}\frac{d(rt_s)}{ds} - \frac{\cos\theta}{r} t_\varphi = -\tau_s$ and becomes $\frac{d(rt_s)}{ds} = t_\varphi \cos\theta$ if $\tau_s = 0$. However, [36] considers for $\tau_s \neq 0$ and so a new term, $\kappa_s q_s$ is included to balance the tangential stresses.

Rewritten Equation (3.6) as

$$\frac{1}{r}\frac{d(rm_s)}{ds} - \frac{\cos\theta}{r}m_\varphi - q_s = 0 \tag{3.9}$$

Equation (3.9) is a mathematical statement of balance of bending moments, where bending moments are assumed to be isotropic. Note that $\frac{d(rm_s)}{ds} = m_\varphi \cos\theta$ and accordingly Equation (3.9) becomes $q_s = 0$.

3.4.2 Constitutive Relations

Constitutive relations are used to close the system of mechanical and geometric equations and to describe the elastic properties of the shell. The stretching of the wall, strain and stress are linked to each other using the theory proposed by [25]. These relations require the postulation of an elastic energy. Using an elastic free-energy, function, W (energy per unit volume), constitutive relations are given by

$$W = W(I_1, I_2, I_3), \tag{3.10}$$

where I_1, I_2 and I_3 represent strain invariants of the deformation tensor and are given as follows:

$$I_1 = \alpha_s^2 + \alpha_\varphi^2 + \alpha_3^2, \tag{3.11}$$

$$I_2 = \alpha_s^2\alpha_\varphi^2 + \alpha_s^2\alpha_3^2 + \alpha_\varphi^2\alpha_3^2, \tag{3.12}$$

$$I_3 = \alpha_s\alpha_\varphi\alpha_3. \tag{3.13}$$

For incompressible materials, $\alpha_3 = \frac{1}{\alpha_s\alpha_\varphi}$ making $I_3 = 1$. Therefore, W can only be defined in terms of I_1 and I_2.

Constitutive relation for t_s and t_φ

Standard shell theory shows that the stresses, t_s and t_φ, can be expressed in terms of the derivatives of W with respect to the stretches as follows [32, 36]

$$t_s = 2h\alpha_3(\alpha_s^2 - \alpha_3^2)\left(\frac{\partial W}{\partial I_1} + \alpha_\varphi^2 \frac{\partial W}{\partial I_2}\right), \tag{3.14}$$

$$t_\varphi = 2h\alpha_3(\alpha_\varphi^2 - \alpha_3^2)\left(\frac{\partial W}{\partial I_1} + \alpha_s^2 \frac{\partial W}{\partial I_2}\right), \tag{3.15}$$

with h representing shell thickness. The choice of W in this model is the neo-*Hookean* model, that is

$$W = C_1(I_1 - 3), \tag{3.16}$$

where the coefficient, C_1, for small deformation is related to *Young*'s modulus by $E = 6C_1$. This choice provides constitutive relations similar to those of standard linear elasticity theory.

For any model, the constitutive relation of t_s and t_φ in Equations (3.14) and (3.15), can take the form of

$$t_s = A\alpha_3(\alpha_s^2 - \alpha_3^2)(1 + \mu\alpha_\varphi^2) \equiv Af_s(\alpha_s, \alpha_\varphi), \tag{3.17}$$

$$t_\varphi = A\alpha_3(\alpha_\varphi^2 - \alpha_3^2)(1 + \mu\alpha_s^2) \equiv Af_\varphi(\alpha_s, \alpha_\varphi), \tag{3.18}$$

where f_s and f_φ are dimensionless functions and A provides the dimensional factor appropriate for the scaling of the equilibrium equations.

Constitutive relation for m_s and m_φ

For bending moments, which are assumed to be isotropic and proportional to the change in the surface's mean curvature, the constitutive relation is

$$m_\varphi = m_s = B(\kappa_s + \kappa_\varphi - K_0), \tag{3.19}$$

with K_0 representing the initial mean curvature and B is the bending modulus.

3.4.3 Shell Equations

Geometric and mechanical equations can be combined into a closed system. All derivatives can be written using the material coordinate, σ, leading to ([32, 36])

$$\frac{dz}{d\sigma} = \alpha_s \sin\theta, \tag{3.20}$$

$$\frac{dr}{d\sigma} = \alpha_s \cos\theta, \tag{3.21}$$

$$\frac{d\theta}{d\sigma} = \alpha_s \kappa_s, \tag{3.22}$$

$$\frac{d\kappa_s}{d\sigma} = \alpha_s \left[\frac{\cos\theta}{r} \left(\frac{\sin\theta}{r} - \kappa_s \right) + \frac{q_s}{B} \right], \tag{3.23}$$

$$\frac{dt_s}{d\sigma} = \alpha_s A \left[\frac{\cos\theta}{r}(f_\varphi - f_s) + \kappa_s \frac{q_s}{A} - \frac{\tau_s}{A} \right], \tag{3.24}$$

$$\frac{dq_s}{d\sigma} = \alpha_s A \left[\frac{q_n}{A} - \kappa_\varphi f_s - \frac{\sin\theta}{r} f_\varphi - \frac{q_s}{A}\frac{\cos\theta}{r} \right]. \tag{3.25}$$

Equation (3.6) is used to derive Equation (3.23) using the constitutive relation given in Equation (3.19) and the definition of the curvatures is used to express κ_φ in terms of r and θ. Stresses, t_s and t_φ, in Equations (3.24) and (3.25) are given in terms of α_s and α_φ through the scaled constitutive relations given in Equations (3.16) and (3.17). Equation (3.24) is converted into a differential equation for α_s by eliminating α_φ through the relation, $\alpha_\varphi = \frac{r}{\rho}$.

The above ordinary differential equations (Equations (3.20)-(3.25)), in combination with the relations written in Equations (3.17) and (3.18) and $\alpha_\varphi = \frac{r}{\rho}$ give a closed system for the variables $(z, r, \theta, \kappa_s, \alpha_s, q_s)$. This can be solved for a given initial profile, $\rho(\sigma)$, elastic parameters, A, B, prescribed normal and tangential stresses q_n and τ_n and appropriate boundary conditions.

Equation (3.25) reduces to

$$\frac{q_n}{A} = \kappa_s f_s + \kappa_\varphi f_\varphi, \tag{3.26}$$

when bending moments are ignored, the shell no longer supports an out-of-plane shear force, namely, $q_s = 0$, which is a generalized form of the *Young-Laplace* law. Following that, a more simplified system of equations is given as follows ([32, 36]) :

$$\frac{dz}{d\sigma} = -\alpha_s \sin\theta, \tag{3.27}$$

$$\frac{dr}{d\sigma} = \alpha_s \cos\theta, \tag{3.28}$$

$$\frac{d\theta}{d\sigma} = \alpha_s \kappa_s, \tag{3.29}$$

$$\frac{d\kappa_s}{d\sigma} = \alpha_s \left[\frac{\cos\theta}{r} \left(\frac{\sin\theta}{r} - \kappa_s \right) \right], \tag{3.30}$$

$$\frac{dt_s}{d\sigma} = \alpha_s A \left[\frac{\cos\theta}{r} (f_\varphi - f_s) - \frac{\tau_s}{A} \right] \tag{3.31}$$

Using the constitutive relationship, $t_s = A f_s \left(\alpha_s, \frac{r}{\rho} \right)$, results in a closed system of five equations (Equations (3.27)-(3.31)) for $(z, r, \theta, \kappa_s, \alpha_s)$ with an initial profile, $\rho(s)$, a tangential shear, τ_s and boundary values [32, 36].

3.5 Effective Pressure Profile

The structural details or the architecture of the cell wall is a basis component of any model of apical growth, which represents the cell wall anisotropy. Note that [67] proposed the hypothesis that tip-growing cells have a "soft-spot". The "soft-spot" hypothesis describes that the newly incorporated material at the tip can flow and therefore easily deform [47]. However, for instance, details of the influence of the cross-linking rate of the polymers or the corresponding hardening rate of cell wall on the tip shape is difficult to obtain experimentally.

This model takes a simple approach to capture the essence of the "soft-spot" hypothesis. Basically, the essence of "soft-spot" hypothesis is modelled by prescribing that the elastic response of the cell wall varies along the meridional direction. That is, regions behind the tip are rigid, while the regions near the tip have a much smaller elastic modulus, corresponding to a softer material.

The essence of the "soft-spot" hypothesis is mathematically modelled by a function known as the effective pressure profile, $q_n^{(\text{eff})}(\sigma)$ and is given by

$$q_n^{(\mathrm{eff})}(\sigma) \;=\; \frac{Q}{2}\left[1-\tanh\left(\frac{\sigma-\sigma_1}{a}\right)\right]+b, \tag{3.32}$$

where the parameter Q sets the scale of normal stress and the parameters σ_1 and a describe the length of the apical extension zone. The parameter b describes the effective normal force far from the tip, since $\lim_{\sigma\to\infty} q_n^{(\mathrm{eff})} = b$, where the cell walls are rigid.

Moreover, the profile, $q_n^{(\mathrm{eff})}$, is a function of the elastic modulus and the turgor pressure, which can be considered as ad hoc. This is because the profile, $q_n^{(\mathrm{eff})}$, is obtained by fitting the rate of incorporated wall-building materials (namely, tritiated *N-acetyl D-glucosamine* along the the hyphae of *S. coelicolor*) to experimental data. A typical plot of $q_n^{(\mathrm{eff})}$ is shown in Figure 3.7.

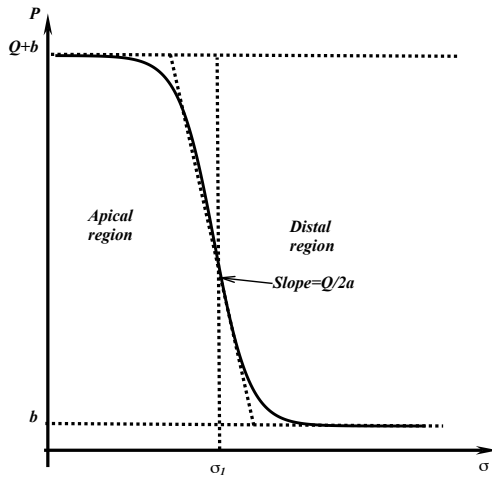

Figure 3.7: A typical plot of the effective normal stress, $q_n^{(\mathrm{eff})}(\sigma)$. Close to the tip ($\sigma = 0$), the walls are soft. In the distal regions, the walls are relatively rigid. Reproduced with kind permission from [36].

Based on Figure 3.7, close to the tip (namely, apical region), $q_n^{(\mathrm{eff})}(\sigma)$ increases to a maximum. However, starting after $\sigma = \sigma_1$, $q_n^{(\mathrm{eff})}(\sigma)$ drops off away from the tip and can reach $q_n^{(\mathrm{eff})}(\sigma) = 0$, which indicates distal regions. The slope of $q_n^{(\mathrm{eff})}(\sigma)$ is always negative, namely, from high $q_n^{(\mathrm{eff})}(\sigma)$ to low $q_n^{(\mathrm{eff})}(\sigma)$. Also, as the growth proceeds, the slope becomes more downhill because of the increasing parameter a. The idealized

profile used for the theoretical analysis is shown with a dashed line indicated that its slope is ∞, where $a = 0$.

3.6 Computer Simulation

Computer simulation of the growth process is represented by a reparameterization of the extended shell once mechanical equilibrium is reached. That is, after each deformation of the wall, the material points are redistributed uniformly: thereby resetting the arc length along the wall for the next deformation step. Without re-parameterization, the shell, would, for a fixed pressure, remain in its equilibrium configuration [32, 35, 36].

Briefly, the computer simulation procedure is implemented as follows ([32, 36]):

- It starts off with an initial shape defined by the function, $\rho_0(\sigma_0)$, $0 \leq \sigma \leq L_0$, and compute the new shape, $r(\sigma_0)$, by solving the mechanical equations subject to the boundary conditions, $r(L_0) = R_0$ and $r(0) = 0$. The new shape, $r_0(\sigma)$, represents the new mechanical equilibrium of the shell.

- Once the stresses are fully relieved, the new reference configuration is characterized by the pair $(\sigma_1 = s(\sigma_0), \rho_1(\sigma_1))$, which defines the new reference shape of length, $L_1 = s(L_0)$ computed from Equations (3.1) and (3.2). The new configuration is then used to compute a new mechanical equilibrium with boundary conditions, $r(L_1) = R_0, r(0) = 0$ and so on.

3.7 Results

3.7.1 Stretchable Region

We begin by examining the effect of varying arc length of the stretchable region on tip shape. In Figure 3.8, the arc length of the stretchable region is represented by orangish dotted line and in Equation (3.32), it is denoted by σ_1.

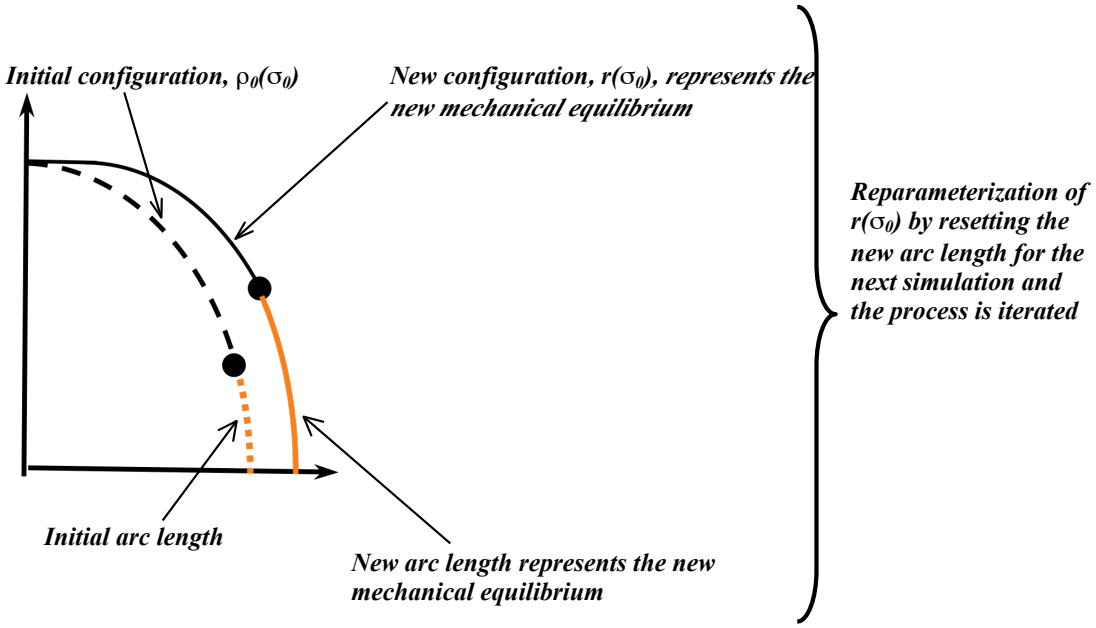

Figure 3.8: Basic schematic representation of surface reparameterization approach used in generating the computer simulation of the tip growth.

A choice of $\sigma_1 = \frac{\pi}{12}$ was made by [32, 33, 34, 35, 36]. Accordingly, evolution of a hyphal tip over number of time steps can be simulated by employing Equations (3.27)-(3.31) with an initial configuration and is shown in Figure 3.9, which represents phases of the tip propagation. Throughout these phases, we observed that at each time step, the newly grown tip has a bigger curvature compared to the tip at the previous time step. As growth proceeds, the tip shape appears to be self-similar.

This model is pressure-driven; increasing pressure results in a narrower tip shape and decreasing pressure results in a broader tip shape. While prior work has shown that pressure can change the geometry of the tip shape, there has been no discussion on the effect of varying σ_1 on the geometry of the tip shape. This basically motivates us to examine another factor that might contribute to differences in geometry of tip shape, namely, σ_1. Using the same pressure value with the same number of time steps shown in Figure 3.9, the tip evolves broadly when the value of σ_1 is changed to 1.0 as shown in Figure 3.10.

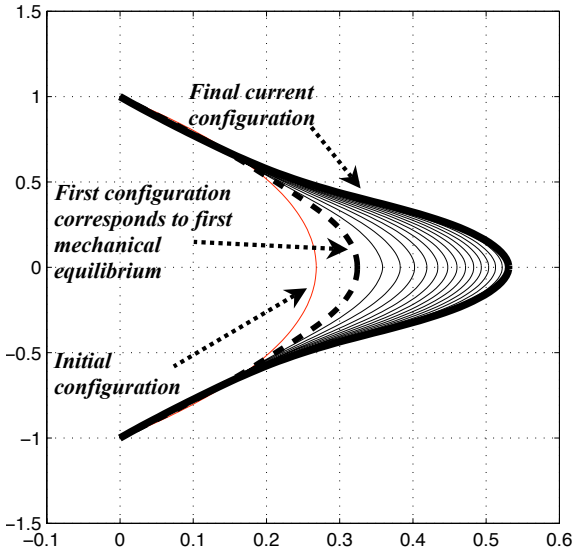

Figure 3.9: Evolution of a hyphal tip over number of time steps when $\sigma_1 = \frac{\pi}{12}$.

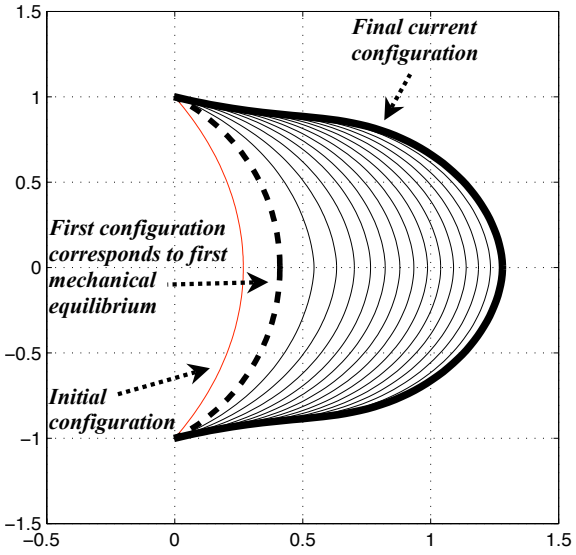

Figure 3.10: Evolution of a hyphal tip over number of time steps when $\sigma_1 = 1.0$.

In comparison to when $\sigma_1 = \frac{\pi}{12}$, setting $\sigma_1 = 1.0$ gives the tip a smaller tip curvature. Therefore, theoretically, we suspect σ_1 could contribute to a different geometry of the tip, which to our knowledge has not been discussed before.

Figures 3.9 and 3.10 correspond to the final current configurations, respectively,

following is each of its 3-D representation rotated about the z-axis through an angle of 2π.

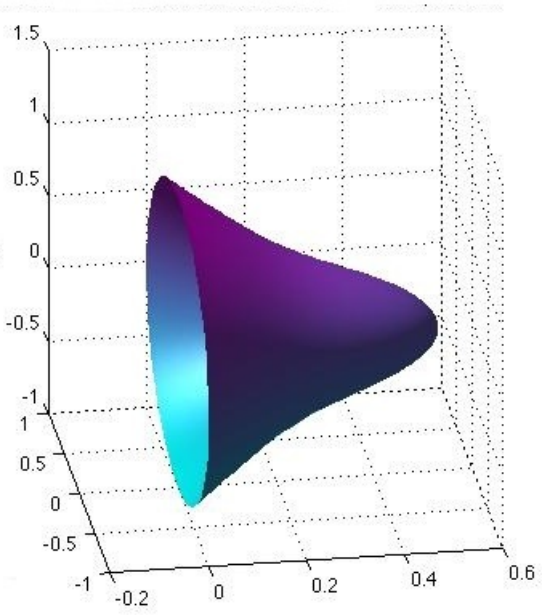

Figure 3.11: Corresponds to the final current configuration shown in Figure 3.9 (namely, when $\sigma_1 = \frac{\pi}{12}$), this its 3-D representation rotated about the z-axis through an angle of 2π.

3.7.2 Self-Similar Tip Propagation

Here we consider the evolution of self-similar tip propagation using the effective pressure profile, $q_n^{(\text{eff})}$. This is given by Equation (3.32), which mathematically describes the structural representation of the cell wall. A general plot of Equation (3.32) is shown in Figure 3.8, where elastic response of the cell wall varies along the longitudinal direction.

By employing Equation (3.32) and choosing $\sigma_1 = \frac{\pi}{12}$, we can plot a sequence of effective pressure profiles over number of time steps for a growing tip as shown in Figure 3.13. We can see that from Figure 3.13, each newly generated profile is extremely close to the generated profile in the previous time step. This suggests that convergence to self-similar tip propagation occurs incredibly "fast". Also, Figure 3.13 shows that as growth proceeds, the apical region becomes smaller and the distal region becomes

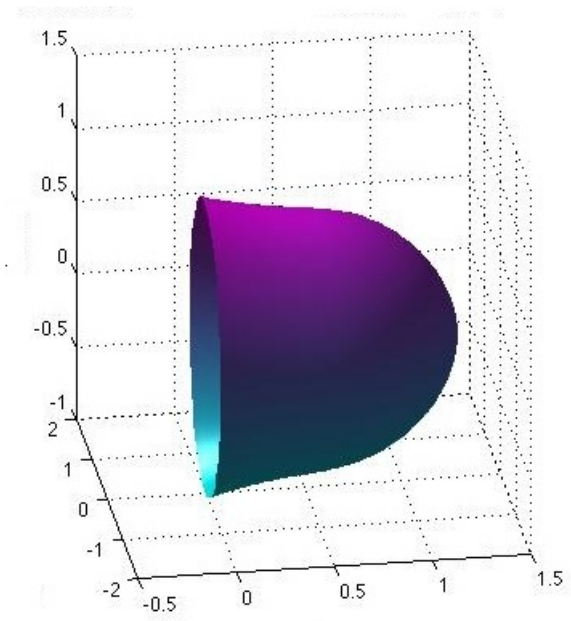

Figure 3.12: Corresponds to the final current configuration shown in Figure 3.10 ($\sigma_1 = 1.0$), this its 3-D representation rotated about the z-axis through an angle of 2π.

bigger.

Figure 3.14 is a plot of sequence of effective pressure profiles over the same number of time steps for a growing tip with $\sigma_1 = 1.0$. We observe that at each subsequent time step, the newly generated profile tends to be closer to the generated profile in the previous time step. Distance between each profile distinguishes this sequence from the previous sequence. Convergence to self-similar tip propagation for this sequence seem to occur "slower" compared to the previous sequence. This suggests that using a different value of σ_1 might cause convergence to self-similar tip propagation to arise differently. However, similarly to the case shown in Figure 3.13, the more distant portions of the cell wall tend to rigidify as the tip progressively elongates.

Simulations of the evolution of a hyphal tip and the evolution of self-similar tip propagation are programmed to run simultaneously. The simulation of the evolution of self-similar tip propagation uses the effective pressure profile, $q_n^{(\text{eff})}$. From that it follows, the same finite number of iterations are specified in both simulations, where

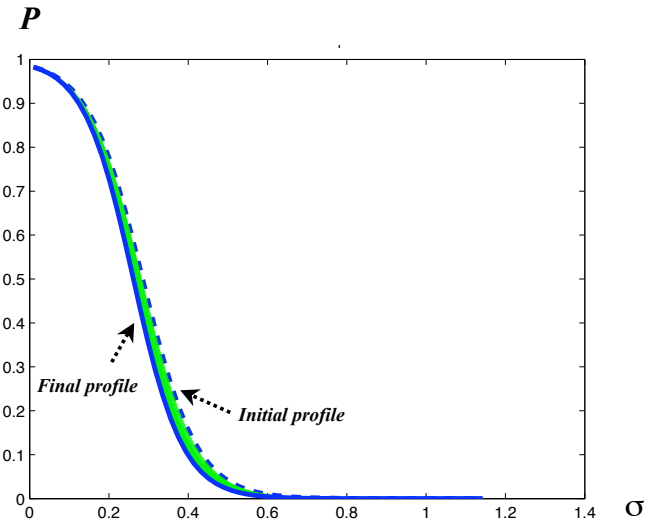

Figure 3.13: Sequence of effective pressure over number of time steps for a tip when $\sigma_1 = \frac{\pi}{12}$.

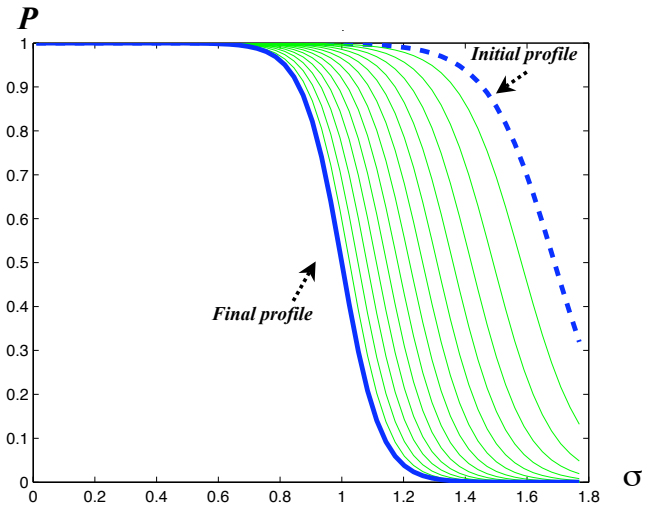

Figure 3.14: Sequence of effective pressure over number of time steps for a tip when $\sigma_1 = 1.0$

number of iterations necessary to obtain a converged solution. Starting with the initial condition, the solution is progressively resolved by iteration until a converged solution is achieved. Say, Num is the finite number of iterations used in the simulation scheme, namely, $Num = Num_{\text{start}}, ..., Num_{\text{end}}$, where N_{end} represents the final iteration generating the 'final profile'. Now let Num with a new Num_{end}, namely, $Num_{\text{new end}}$. The new 'final profile' generating from the new final iteration is the same as the 'final

profile' when Num_{end} is set as the final iteration and this shows that steady state exists.

In [36], the growth of filamentous fungi is described in terms of self-similar tip growth using a growth sequence profile by stating that at each step, the new shape is a duplicate of the previous one properly translated. Here we describe the self-similar tip growth using the effective pressure sequence profile. We show that 'rate' of convergence to self-similar tip propagation depends on the arc length of stretchable region, σ_1, of the initial condition. When the initial condition is set with $\sigma_1 = \frac{\pi}{12}$, distance between a newly material point and a previous material point on a growing tip is extremely close to each other, where the growth is self-similar. Such closeness and self-similar can be shown from the effective pressure profile. That is, the newly generated profile tends to be extremely closer to the generated profile in the previous time step which causes 'fast' convergence to self-similar tip. The 'fast' convergence to self-similar tip simply refers to the extremely small translation distance between the effective pressure profiles.

3.7.3 Variation in Pressure

Variation in pressure for a hypha profile

The cell wall of a hypha is differentially elastic along the longitudinal direction and this leads to variation in pressure exerted on the cell wall. As we mentioned earlier, this model employs the *Young-Laplace* equation to describe pressure difference for a curved surface, where the internal pressure must be greater than the external pressure. According to the equation, maximum pressure corresponds to minimum radius of curvature of a surface and minimum pressure corresponds to maximum radius of a curvature of surface.

We show a figurative description representing variation in pressure acting along the cell wall of a hypha. Different levels of pressure are represented by different colors indicated by the color bar. Maximum pressure level corresponds to the color shown at the top of the bar and minimum pressure level corresponds to the color shown at the

bottom of the bar.

Figures 3.15 and 3.16 show variation in pressure along the cell wall of a hypha when $\sigma_1 = \frac{\pi}{12}$ and $\sigma_1 = 1.0$, respectively. The hypha profile in Figure 3.15 is referred to final current configuration shown in Figure 3.9. The hypha profile in Figure 3.16 is referred to final current configuration shown Figure 3.10.

In Figure 3.15, the pressure increases to a maximum as a tip is approached. Similarly to Figure 3.15, Figure 3.16 as well indicates that the pressure increases to a maximum as a tip is approached. When $\sigma_1 = \frac{\pi}{12}$, the entire tip is under maximum pressure. However, when $\sigma_1 = 1.0$, only a portion of the tip is under maximum pressure. In contrast, when $\sigma_1 = 1.0$, a greater portion of the rigid region is under minimum pressure.

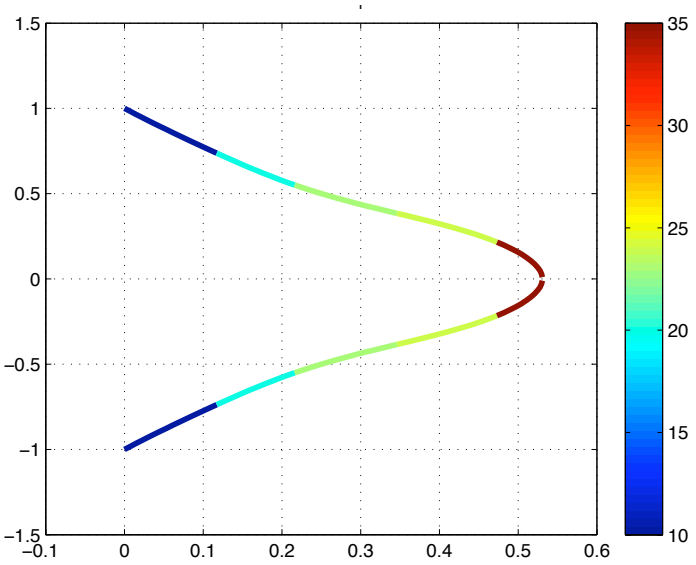

Figure 3.15: Corresponds to the final current configuration shown in Figure 3.9 (namely, when $\sigma_1 = \frac{\pi}{12}$), this is its representation of variation in pressure along the cell wall of a hypha.

Variation in pressure for the effective pressure profile

We consider variation in pressure acting along the cell wall of a hypha using the effective pressure profile, $q_n^{(\text{eff})}$.

A variation in pressure for the effective pressure profile is shown using a figurative

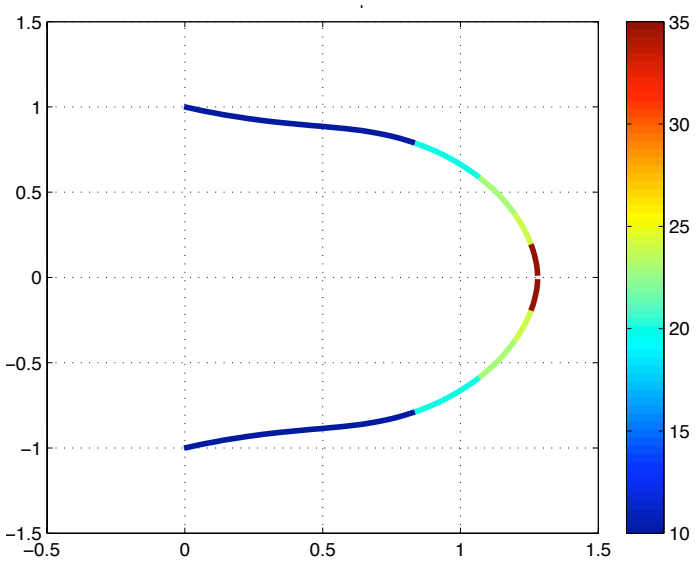

Figure 3.16: Corresponds to the final current configuration shown in Figure 3.10 (namely, when $\sigma_1 = 1.0$), this is its representation of variation in pressure along the cell wall of a hypha.

representation. Different levels of pressure are represented by different colors indicated by the color bar. The color shown at the top of the bar indicates maximum pressure level and the color shown at the bottom of the bar indicates minimum pressure level.

Figures 3.17 and 3.18 show variation in pressure for the effective pressure profiles when $\sigma_1 = \frac{\pi}{12}$ and $\sigma_1 = 1.0$, respectively. The effective pressure profile in Figure 3.17 is referred to final profile shown in Figure 3.13. The effective profile in Figure 3.18 is referred to final profile shown in Figure 3.14.

In Figure 3.17, the pressure increases to a maximum as a tip is approached. Similarly to Figure 3.17, Figure 3.18 as well indicates that the pressure increases to a maximum as a tip is approached. In Figure 3.17, the distance between $\sigma = 0$ and $\sigma_1 = \frac{\pi}{12}$ is governed by a downhill curved line in which the entire line is under maximum pressure. However, in Figure 3.18, the distance between $\sigma = 0$ and $\sigma_1 = 1.0$ is governed by a greater segment of straight line, which is under maximum pressure.

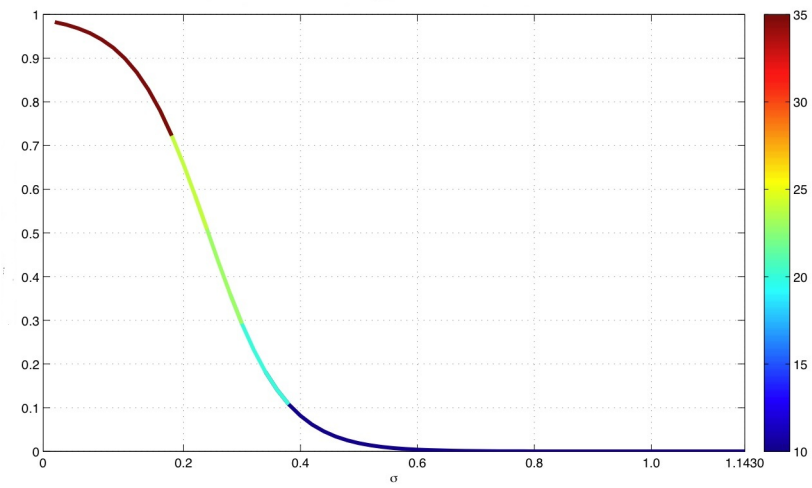

Figure 3.17: Corresponds to the final effective pressure profile shown in Figure 3.13 (namely, when $\sigma_1 = \frac{\pi}{12}$), this is its representation of variation in pressure.

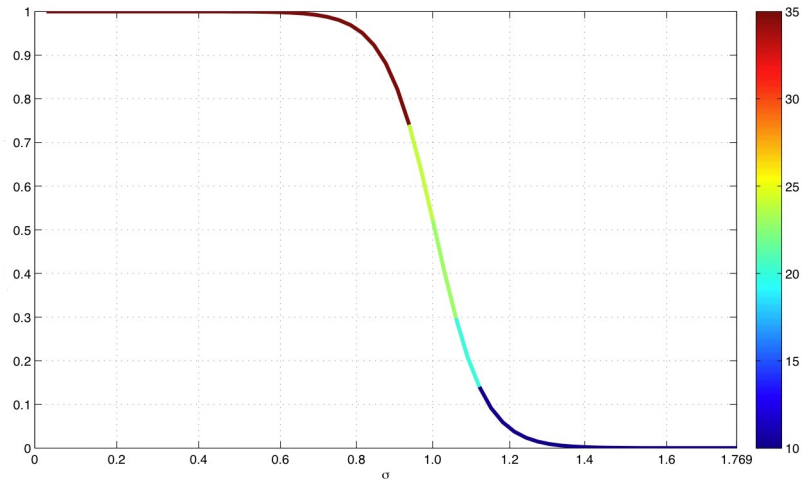

Figure 3.18: Corresponds to the final effective pressure profile shown in Figure 3.14 (namely, when $\sigma_1 = 1.0$), this is its representation of variation in pressure.

3.7.4 Surface Friction and Orthogonal Growth

The hypothesis of orthogonal growth means that material points on the tip appear to move in a direction perpendicular to the tip surface as the tip grows. The possibility of such a growth pattern was discussed well over a hundred years ago by [67] and has been confirmed in experimental studies of fungi by [29] and root hairs by [23].

We show the effect of surface friction, τ_s, together with pressure, Q, exerted on tip shapes resulting from external friction due to the burrowing medium. We only consider material points on the apex of what we assume the equivalent germ tube. Through out our examination, evolution of a germ tube over the same number of time steps can be simulated by employing Equations (3.27)-(3.31) with an initial configuration of $\sigma_1 = \frac{\pi}{12}$. In every figurative representation of evlotion of a germ tube, initial configuration is represented by a red curve, material points on the tip surface are represented by red dots and green lines are what would be the equivalent orthogonal trajectories on the tip surface.

3.7.5 Without surface friction

First, we consider evolution of a germ tube in the absence of surface friction, namely, when $\tau_s = 0$ as shown in Figure 3.19.

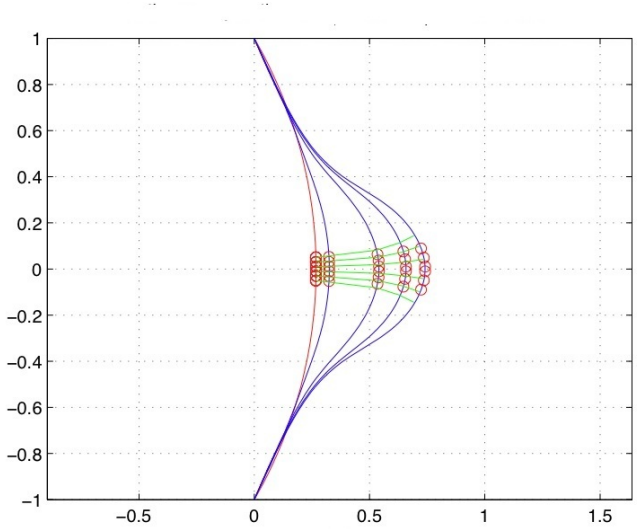

Figure 3.19: Evolution of a germ tube in the absence of surface friction, namely, when $\tau_s = 0$.

In Figure 3.19, we observe that material points on the very first grown tip surface align with the orthogonal trajectories. However, as growth continues, material points on the subsequent grown tips tend to move away from the orthogonal trajectories.

3.7.6 With fixed surface friction and various pressure

We consider evolution of a germ tube by fixing τ_s and varying Q acting on the wall.

Figures 3.20 and 3.21 show evolution of a germ tube when $\tau_s = 0.3$, $Q = 0.1$ and $\tau_s = 0.3$, $Q = 1.0$, respectively. Both in Figures 3.20 and 3.21, we observe that material points on the very first grown tip surface align with the orthogonal trajectories. In Figure 3.20, when $\tau_s = 0.3$, $Q = 0.1$, material points on the subsequent grown tips align with the orthogonal trajectories but then tend to move away as material points on the tip tends distance away from each other. In Figure 3.21, $\tau_s = 0.3$, $Q = 1.0$, material points on the subsequent grown tips slightly align with the orthogonal trajectories. Unlike in Figure 3.20, as the tip propagates, material points shown in Figure 3.21 are close to each other.

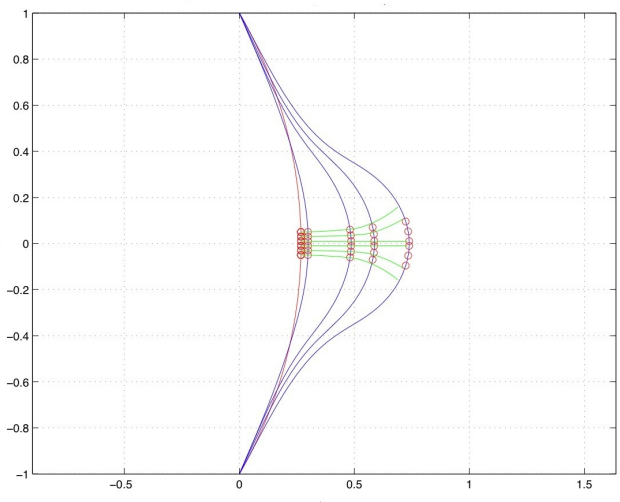

Figure 3.20: Evolution of a germ tube when $\tau_s = 0.3$, $Q = 0.1$.

3.7.7 With various surface friction and fixed pressure

We consider evolution of a germ tube by varying τ_s and fixing Q acting on the wall.

Figures 3.22 and 3.23 show evolution of a germ tube when $\tau_s = 0.6$, $Q = 0.1$ and $\tau_s = 0.3$, $Q = 1.0$, respectively. (Note that Figure 3.23 is Figure 3.21, however, for the sake of clear description of orthogonal growth, we show Figure 3.21 again here as

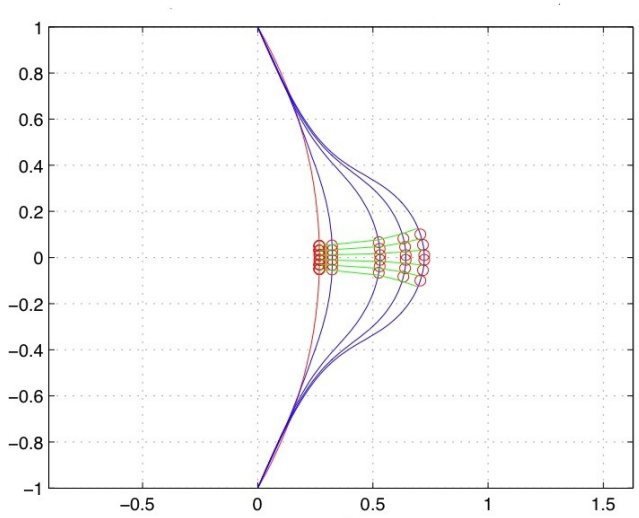

Figure 3.21: Evolution of a germ tube when $\tau_s = 0.3$, $Q = 1.0$.

Figure 3.23). Both in Figures 3.22 and 3.23, we observe that material points on the very first grown tip surface align with the orthogonal trajectories. In Figure 3.22, $\tau_s = 0.6$, $Q = 0.1$, material points on the subsequent grown tips align with the orthogonal trajectories except at the final current configuration tip.

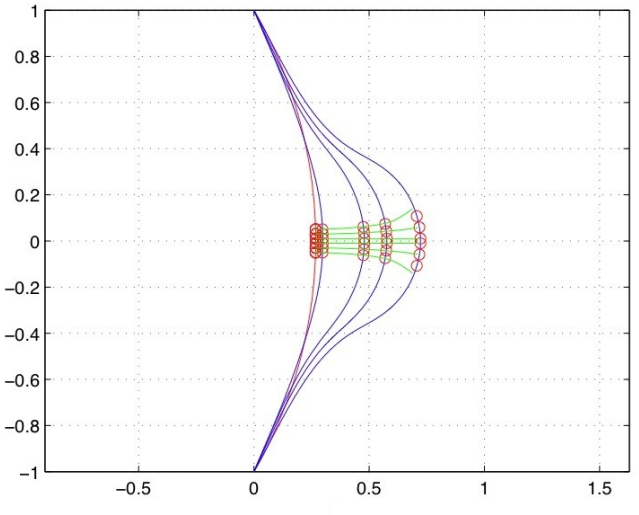

Figure 3.22: Evolution of a germ tube when $\tau_s = 0.6$, $Q = 0.1$.

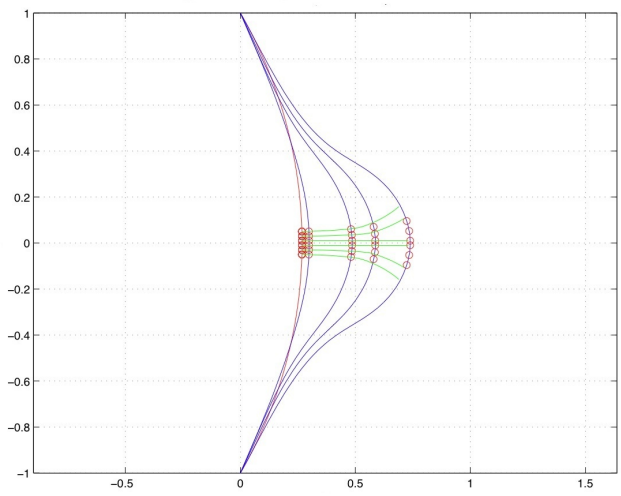

Figure 3.23: Evolution of a germ tube when $\tau_s = 0.3$, $Q = 1.0$.

Note

Through out every examination, we agree that early growth phases of a germ tube fulfill the hypothesis of orthogonal growth. However, this result remains a theory until there is a clear evidence from experimental studies.

"Ideal" orthogonal growth

We consider evolution of a germ tube when $\tau_s = 0.7$, $Q = 1.0$ as shown in Figure 3.24. In Figure 3.24, we observe that material points on every grown tip surface align with the orthogonal trajectories. This is the 'ideal' orhogonal growth.

3.8 Summary

As proposed by [36], this model is pressure driven, where it is assumed that deposition of wall-building materials is proportional to turgor pressure. The formulation presented in this model is sufficiently general to accommodate many different effects. While prior work has shown that pressure can change the geometry of the tip shape, there has been no examination on the effect of varying arc length of stretchable region on tip shape.

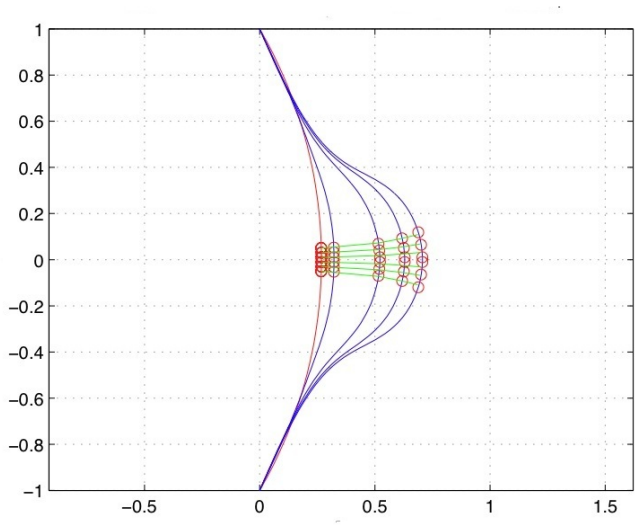

Figure 3.24: Evolution of a germ tube when $\tau_s = 0.7$, $Q = 1.0$.

We observe that varying arc length of stretchable region on the initial tip results in differences in geometry of tip shape profile, effective pressure profile and self-similar tip propagation.

Also, we observe that either when surface friction is increased or decreased (note that same holds when pressure is increased or decreased), early growth phases of what would be equivalent to germ tube experiences the orthogonal growth (wall expansion is normal at right angles to the tip).

Chapter 4

Conclusions and Future Work

4.1 Conclusions

In this thesis, we have studied mathematical modeling of fungal tip growth. We considered both geometrical and biomechanical models, where the tip shape evolves naturally through mathematical formulations for describing growth. Mathematical interpretations of the growth mechanism was the core feature studied here.

Much of the work in this thesis concerned generally deposition of wall-building materials associated with the tip curvature.

In Chapter 2, we are interested with the mathematical derivation of the hyphoid equation as proposed by [7], where a number of problems regarding the derivation were pointed out by [50]. We suggest that the derivation can be revised as follows: maximum deposition of wall-building materials takes place when the change in arc length per unit angle, β, is maximum. Deposition of wall-building materials is associated to tip curvature, namely, curvature equal to the reciprocal of its radius (the distance from the shape-organising center to the tip) provided that β to the growth axis is small, namely, $\beta << 1$. When $\beta << 1$, the position of the Spitzenkorper is not close to the apical wall. Also, $\beta << 1$ indicates that deposition of wall-building materials per unit time is greater than the rate of linear displacement of the Spitzenkorper. From that it follows, broader hyphoid curves are generated. Although when $\beta > 1$ does produce hyphoid

curves-like, these curves are not evolved from the proposed assumptions. Derivation of the hyphoid equation is not unique and so considering $\beta > 1$ subjected to proper assumptions might be a way to expand this work. From this work, it also suggests that the angle to the growth axis cannot be assumed arbitrarily as stated by [7], instead it needs to satisfy a specific condition in order to agree with known fungal physiology.

Also in Chapter 2, we studied when deposition of wall-building materials is associated to principal curvatures of the tip as proposed by [31]. The first model considers when deposition of wall-building materials, n, is associated to longitudinal tip curvature, κ, namely, $n \propto \kappa^p$, where $p > 0$. We showed that it is possible to derive generalized formulae for the tip shape. From the generalized formulae, localization of deposition of wall-building materials can be examined and accordingly, it suggests that not every generated tip is biological plausible. For the tip shape generated when $p = 0$, the wall-building materials are deposited everywhere equally and this contradicts known fungal physiology. For tip shape generated when $0 < p < 1$, localization of deposition of wall-building materials as well contradicts known fungal physiology. This is because when $0 < p < 1$, maximum deposition of wall-building materials occurs at the most distal region of the tip. However, such manner of deposition is applicable for pollen tube tip growth. When $1 < p < 2$, deposition of wall-building materials is not relevant. When $p >= 2$, deposition of wall building materials agrees with known fungal physiology. The second model considers when deposition of wall-building materials is associated to longitudinal and latitudinal curvatures. We showed that it is possible to derive a new relationship in generating tip shape. The new relationship is used to model deposition of wall building materials, which generates a broader tip shape compared to the tip shape proposed by [31]. It is interesting to expand this model by examining on localization of deposition of wall-building materials.

In Chapter 3, we considered deposition of wall-building materials associated to turgor pressure as proposed by [36]. We observed that by varying arc length of stretchable region on the initial tip, it demonstrates differences in geometry of tip shape profile, effective pressure profile and self-similar tip propagation. While prior work has shown

that pressure can change the geometry of the tip shape, there has been no discussion on the effect of varying arc length of stretchable region on the geometry of the tip shape. Also, smaller arc length of stretchable region suggests that convergence to self-similar tip propagation occurs incredibly "fast" and vice versa. We also examined the effect of surface friction and the hypothesis of orthogonal growth focused only on the apex of what we assume as equivalent germ tube. Following that, it suggests that material points on the tip appear to move in a direction perpendicular to the tip surface during early phases of growth either when surface friction is increased or decreased. (Same holds when pressure is increased or decreased.) The reason for this maybe because the turgor pressure uses a perpendicular force to the soft wall in which there is no rigid wall behind it during the early phases of germ tube growth. Soft spot hypothesis proposed by [67] states that tip growing cells have a 'soft-spot, where the newly deposited materials at the tip can flow and therefore can easily deform.

4.2 Future Work

Generally, our future work will consider a computer simulation of vesicle-based model featuring the vesicle diffusion, where the Spitzenkorper plays a role in fungal tip growth. Such model was first proposed by [7] and then later on by [81]. In [7], once released isotropically (equally in all directions) from the Spitzenkorper, vesicles are assumed to be transported ballistically (motion over straight lines) towards the tip boundary. While [81] assumes that vesicles diffuse from the Spitzenkorper towards the tip boundary, where important details of their subsequent fusion with the cell membrane are included.

Our future work is interested with generation of apical swelling using the vesicle-based model. Antibiotics of *b*-lactam cause apical swelling of the hyphae leading, in some cases, to lysis [32]. From a mechanical point of view, apical swelling presumably resulted from an increase in internal hydrostatic pressure acting on the tip wall. Apical swelling has mathematically modeled by [33], where it is represented by an increase of the effective pressure.

According to [7]: For a given number of vesicles released by the Spitzenkorper, the faster the Spitzenkorper advances, the narrower is the tube that is produced. Conversely, for a given rate of linear Spitzenkorper displacement, the greater number of vesicles released per unit time, the broader the tube. In order to interpret apical swelling in terms of computer simulation of vesicle-based model, our setting will first need to involve a situation where for a given rate of linear Spitzenkorper displacement, number of vesicles released varies as the Spitzenkorper advances. Varying number of vesicles released requires further examination. However, we managed to generate a hypha-like shape based on three different approaches as shown in Figures 4.1-4.3.

Following is a brief description of Figures 4.1-4.3:

In Figure 4.1, generation of a hypha-like shape is basically given by

$$\frac{\partial u(x,y,t)}{\partial t} = D\left(\frac{\partial^2 u(x,y,t)}{\partial x^2} + \frac{\partial^2 u(x,y,t)}{\partial y^2}\right), \tag{4.1}$$

where $u(x,y,t)$ is vesicles released by the Spitzenkorper at point (x,y) at time t for $0 \leq x \leq 50$, $0 \leq y \leq 50$, $t \geq 0$ and D is diffusivity with the *Neumann* boundary conditions as follows

$$\frac{\partial u(x,0,t)}{\partial y} = 0, \quad 0 \leq x \leq 1, \tag{4.2}$$

$$\frac{\partial u(x,1,t)}{\partial y} = 0, \quad 0 \leq x \leq 1, \tag{4.3}$$

$$\frac{\partial u(0,y,t)}{\partial x} = 0, \quad 0 \leq y \leq 1, \tag{4.4}$$

$$\frac{\partial u(1,y,t)}{\partial x} = 0, \quad 0 \leq y \leq 1. \tag{4.5}$$

The initial vesicles released by the Spitzenkorper, u_0, is

$$u(x,y,0) = u_0(x,y), \tag{4.6}$$

where $0 \leq x \leq 50$, $0 \leq y \leq 50$. We consider $u_0 = \frac{1}{\exp\left(\frac{(x-x_0)^2}{a} + \frac{(y-y_0)^2}{b}\right)}$ for positive integers a, b, x_0, y_0, which x_0 and y_0, respectively represent the intial position of the Spitzenkorper in the x- and y- directions. A term (x_0, y_0) perhaps can be called as "centre of vesicle diffusion". This setting shows a stage sequence of a common morphological developmennt of filamentous fungi consists of a long filament hypha. The hypha-like shape shown in Figure 4.1 is generated when the Spitzenkorper is programmed to move in a fixed linear direction while releasing vesicles at the same rate. A displacing Spitzenkorper is simply programmed by continuously displacing the "centre of vesicle diffusion" in the y-direction as time proceeds.

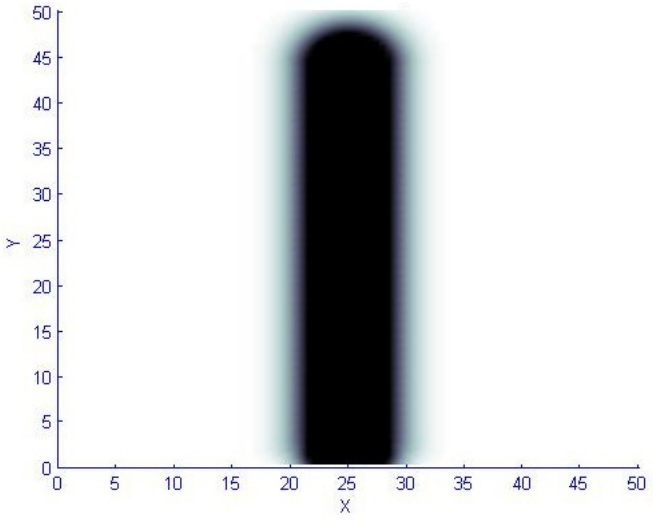

Figure 4.1: Computer simulation of generation of a hypha based on Equation 4.1.

In Figure 4.2, using the same boundary conditions as given in Equations (4.2)-(4.4) and the initial condition, $u_0(x_0, y_0)$, generation of a hypha is basically given by

$$\frac{\partial u(x,y,t)}{\partial t} = D\left(\frac{\partial^2 u(x,y,t)}{\partial x^2} + \frac{\partial^2 u(x,y,t)}{\partial y^2}\right) + \delta(x,y), \tag{4.7}$$

where $\delta(x, y)$ represents the point source. Note that, the Spitzenkorper is taken to be a moving point source. We consider $u_0 = \frac{1}{\exp\left(\frac{(x-x_0)^2}{a} + \frac{(y-y_0)^2}{b}\right)} + \delta_0(x_0, y_0)$ for positive integers a, b, x_0, y_0. The initial point source, $\delta_0(x_0, y_0) = \frac{1}{\exp\left(\frac{c(x-x_{\delta_0})^2}{a} + \frac{c(y-y_{\delta_0})^2}{b}\right)}$

for positive interger c, x_{δ_0} and y_{δ_0}, where $c > 1$ and x_{δ_0} and y_{δ_0}, respectively, represent the intial position of the Spitzenkorper in the x- and y- directions. The moving Spitzenkorper is programmed to move in the y-direcion while releasing vesicles. This setting shows the two-stage sequence of morphological development which occurs during fungal spore germination. We begin with the spherical growth by programming a stationary Spitzenkoper releasing vesicles. This spherical growth can be considered as a spore phase, namely, phase before the emergence of a germ tube. After a period of spherical growth, the Spitzenkorper is programmed to move in a fixed direction while releasing vesicles at the same rate. Subsequently, the shape gradually changes from spherical to tubular.

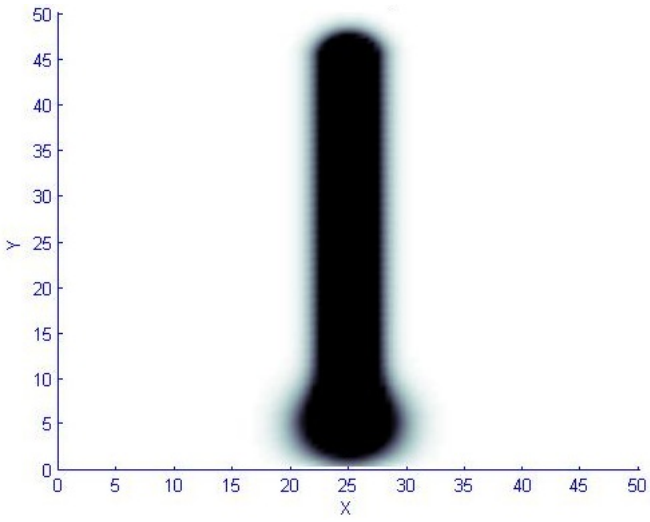

Figure 4.2: Computer simulation of generation of a hypha based on Equation 4.6.

In Figure 4.3, using the same boundary conditions as given in Equations (4.2)-(4.4) and the initial condition, $u_0(x_0, y_0)$, generation of a hypha is basically given by

$$\frac{\partial u(x,y,t)}{\partial t} = D\left(\frac{\partial^2 u(x,y,t)}{\partial x^2} + \frac{\partial^2 u(x,y,t)}{\partial y^2}\right) + \delta(x,y) - \lambda u(x,y,t), \qquad (4.8)$$

where $\lambda u(x, y, t)$ represents "decay" or "absorption" of vesicles at the apical wall after deposition of vesicles. The Spitzenkorper is as well taken to be the moving point source. We consider $u_0 = \frac{1}{\exp\left(\frac{(x-x_0)^2}{a} + \frac{(y-y_0)^2}{b}\right)} + \delta_0(x_0, y_0) - \lambda u(x_0, y_0, t)$ for positive

integers a, b, x_0, y_0. Similarly with the initial point used to produce Figure 4.2, the initial point source here is $\delta_0(x_0, y_0) = \frac{1}{\exp\left(\frac{c(x-x_{\delta_0})^2}{a} + \frac{c(y-y_{\delta_0})^2}{b}\right)}$ for positive interger c, x_{δ_0} and y_{δ_0}, where $c > 1$ and x_{δ_0} and y_{δ_0}, respectively, represent the initial position of the Spitzenkorper in the x- and y- directions. The moving Spitzenkorper is programmed to move in the y-direcion while releasing vesicles. The initial "absorption" of vesicles at the apical wall after deposition of vesicles, $\lambda u(x_0, y_0, t)$, where λ is real such that $0 < \lambda < 1$. As time progresses, "absorption" of vesicles continuously occurs at the wall after veiscles are deposited into the wall. This setting shows the two-stage sequence of morphological development incorporating the "absorption" of vesicles, namely, spherical and tubular.

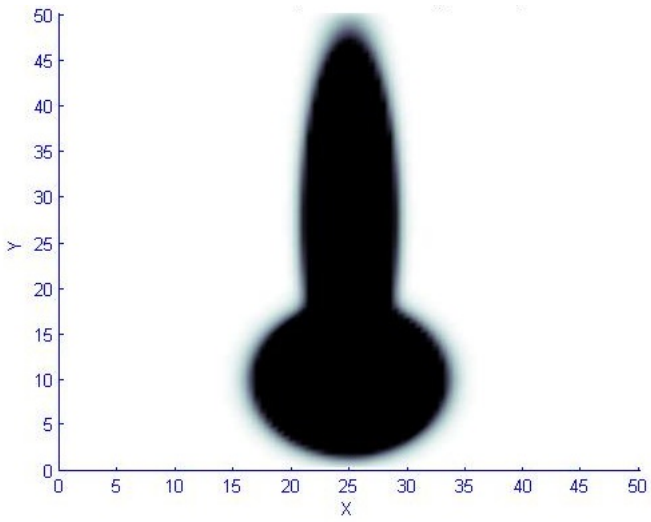

Figure 4.3: Computer simulation of generally of a hypha based on Equation 4.7.

We have developed a framework to describe tip growth using three different approaches based on the vesicle supply center concept. Based on this framework, we suspect that apical swelling could be programmed in such a way that after a period of tubular growth, vesicles then are released from a stationary Spitzenkorper so that the shape gradually changes from tubular to spherical.

Bibliography

[1] O. C. G. Adan and R. A. Samson. *Fundamentals of Mold Growth in Indoor Environments and Strategies for Healthy Living.* Wageningen Academic, 2011.

[2] D. K. Arora and D. Bhatnagar. *Handbook of Fungal Biotechnology.* Marcel Dekker, 2nd edition, 2004.

[3] S. Bartnicki-Garcia. Fundamental aspects of hyphal morphogenesis. *Symposia of the Society for General Microbiology*, 23:245–267, 1973.

[4] S. Bartnicki-Garcia. *The Hypha: Unifying Thread of the Fungal Kingdom. In: B. C. Sutton (ed). A Century of Mycology.* Press Syndicate of the University of Cambridge, 1996.

[5] S. Bartnicki-Garcia. *Hyphal Tip Growth, Outstanding Questions. In: H. D. Osiewacz (ed). Molecular Biology of Fungal Development.* Marcel Dekker, 2002.

[6] S. Bartnicki-Garcia, C. E. Bracker, G. Gierz, R. Lopez-Franco, and H. Lu. Mapping the growth of fungal hyphae: Orthogonal cell wall expansion during tip growth and the role of turgor. *Biophy. J.*, 79:2382–2390, 2000.

[7] S. Bartnicki-Garcia, F. Hergert, and G. Gierz. Computer simulation of fungal morphogenesis and the mathematical basis for hyphal tip growth. *Protoplasma*, 153:46–57, 1989.

[8] L. L. Barton and D. E. Northup. *Microbiol Ecology.* Wiley-Blackwell, 2011.

[9] D. P. Bebber, J. Hynes, P. R. Darrah, L. Boddy, and M. D. Fricker. Biological solutions to transport network design. *Proceedings of the Royal Society B*, 274:2307–2315, 2007.

[10] C. B. Beck. *An Introduction to Plant Structure and Development.* Cambridge University Press, 2005.

[11] L. R. Berg. *Introductory Botany: Plants, People and the Environment.* Thomson Brooks/Cole, 2nd edition, 2007.

[12] G. P. Boswell, H. Jacobs, K. Ritz, G. M. Gadd, and F. A. Davidson. The development of fungal networks in complex environment. *Bulletin Mathematical Biology*, 69:605–634, 2007.

[13] A. Boudaoud. Growth of walled cells: From shells to vesicles. *Physical Review Letter*, 91(1):1–4, 2003.

[14] A. D. Bowen, F. A. Davidson, R. Keatch, and G. M. Gadd. Induction of contour sensing in aspergillus niger by stress and its relevance to fungal growth mechanics and hyphal tip structure. *Fungal Genetics and Biology*, 44:484–491, 2007.

[15] B. Bozic, V. Heinrich, S. Svetina, and B. Zeks. Shapes of nearly cylindrical, axisymmetric bilayer membranes. *The European Physical Journal E*, 6:91–98, 2001.

[16] L. Butcher, P. Eastwood, and A. Macdonald. *Nelson Modular Science*, volume III. Nelson Thornes, 2002.

[17] M. J. Carlile, S. C. Watkins, and G. W. Gooday. *The Fungi.* Academic Press, 2001.

[18] E. S. Castle. The topography of tip growth in a plant cell. *Journal of General Physiology*, 41:913–926, 1958.

[19] D. E. Chandler and R. W. Robertson. *Bioimaging: Current Concepts in Light and Electron Microscopy.* Jones and Bartlett, 2009.

[20] F. A. Davidson. Mathematical modeling of mycelia: A question of scale. *Fungal Biology Reviews*, 21:30–41, 2007.

[21] F. A. Davidson. A blueprint for polarized growth. *Society for General Microbiology: Microbiology Today*, pages 34–37, 2010.

[22] J. W. Deacon. *Fungal Biology.* Wiley-Blackwell, 4th edition, 2006.

[23] J. Dumais, S. L. Shaw, C. R. Steele, S. R. Long, and P. M. Ray. An anisotropic-viscoplastic model of plant cell morphogenesis by tip growth. *Int. J. Dev. Biol.*, 50:209–222, 2006.

[24] K. Esser and R. Fischer. *The Mycota: Growth, Differentiation and Sexuality.* Springer-Verlag, 2nd edition, 2006.

[25] E. A. Evans and R. Skalak. *Mechanics and Thermodynamics of Biomembranes.* CRC Press, 1980.

[26] V. Farkas. *The fungal cell wall. In: J. F. Peberdy and L. Ferenczy (ed). Fungal Protoplasts.* Marcel Dekker, 1980.

[27] G. M. Gadd. *Fungi in Biogeochemical Cycles.* Cambridge University Press, 2006.

[28] S. D. Garrett. *Pathogenic Root-Infecting Fungi.* Cambridge University Press, 1970.

[29] G. Gierz and S. Bartnicki-Garcia. A three-dimensional model of fungal morphogenesis based on the vesicle supply center concept. *Journal of Theoretical Biology*, 208:151–164, 2001.

[30] G. W. Gooday. An autoradiographic study of hyphal growth of some fungi. *Journal of General Microbiology*, 67:125–133, 1971.

[31] A. Goriely, G. Karolyi, and M. Tabor. Growth induced curve dynamics for filamentary micro-organisms. *Journal of Mathematical Biology*, 51:355–366, 2005.

[32] A. Goriely and D. Moulton. *Morphoelasticity: A Theory of Elastic Growth. In: M. B. Amar and A. Goriely and M. M. Muller and L. F. Cugliandolo (ed). New*

Trends in the Physics and Mechanics of Biological Systems. Oxford University Press, 2011.

[33] A. Goriely and M. Tabor. Biomechanical models of hyphal growth in actinomycetes. *Journal of Theoretical Biology*, 222:211–218, 2003.

[34] A. Goriely and M. Tabor. Self-similar tip growth in filamentary fungi. *Physical Review Letter*, 90(10):1–4, 2003.

[35] A. Goriely and M. Tabor. Mathematical modeling of hyphal tip growth. *Fungal Biology Reviews*, 22:77–83, 2008.

[36] A. Goriely, M. Tabor, and A. Tongen. *A Morpho-Elastic Model of Hyphal Tip Growth in Filamentous Organisms. In: K. Garikipati and E. M. Arruda (ed). IUTAM Symposium on Cellular, Molecular and Tissue Mechanics*. Springer, 2010.

[37] N. A. R. Gow and G. M. Gadd. *The Growing Fungus*. Chapman and Hall, 1995.

[38] P. B. Green. Morphogenesis of the cell and organ axis-biological models. *Brookhaven Symposia in Biology*, 25:166–190, 1974.

[39] P. B. Green and A. King. A mechanism for the origin of specifically orientated texture in development with special reference to nitella wall texture. *Australian Journal of Biological Sciences*, 19:421–437, 1966.

[40] D. H. Griffin. *Fungal Physiology*. Wiley-Liss, 2nd edition, 1994.

[41] L. H. S. Guimaraes, S. C. Peixoto-Nogueira, M. Michelin, A. C. S. Rizzatti, V. C. Sandrim, F. F. Zanoelo, A. C. M. M. Aquino, A. B. Junior, and M. L. T. M. Polizeli. Screening of filamentous fungi for production of enzymes of biotechnological interest. *Brazilian Journal of Microbiology*, 37:474–480, 2006.

[42] K. Hammond-Kosack, M. Urban, T. Baldwin, A. Daudi, J. Rudd, J. Keon, J. Lucas, K. Maguire, D. Kornyukhin, H. C. Jing, C. Bass, and J. Antoniw. Plant pathogens: How can molecular genetic information on plant pathogens assist in breeding disease resistant crops. *4th International Crop Science Congress*, 2004.

[43] J. L. Harley. Fungi in ecosystems. *J.Ecol*, 59:653–668, 1971.

[44] S. R. Joshi. *Microbes: Redefined Personality*. S. B. Nangia, 2007.

[45] F. Julicher and U. Seifert. Shape equations for axisymmetric vesicles: A clarification. *Physical Review Letter*, 49(5), 1994.

[46] K. Kavanagh. *Fungi: Biology and Applications*. John Wiley and Sons, 2nd edition, 2011.

[47] M. N. D. Keijzer, A. M. C. Emons, and B. M. Mulder. *Modeling Tip Growth: Pushing Ahead. In: A. M. C. Emons and T. Ketelaar (ed). Root Hairs*. Springer-Verlag, 2nd edition, 2009.

[48] G. Kinsey, R. Paterson, and J. Kelly. *Filamentous fungi in water systems. In: G. M. Gadd (ed). Fungi in Biogeochemical Cycles*. Cambridge University Press, 2006.

[49] A. L. Koch. The shape of fungi. *Journal of General Microbiology*, 128:947–951, 1981.

[50] A. L. Koch. *Bacterial Growth and Form*. Kluwer Academic, 2nd edition, 2001.

[51] K. W. Kolasinski. *Surface Science: Foundation of Catalysis and Nanoscience*. John Wiley and Sons, 3rd edition, 2012.

[52] J. A. Lockhart. An analysis of irreversible plant cell elongation. *Journal of Theoretical Biology*, 8:264–275, 1965.

[53] J. A. Lockhart. *Cell Extension. In: J. Bonner and J. E. Varner. (ed). Plant Biochemistry*. Academic Press, 1965.

[54] R. M. Maier, I. L. Pepper, and C. P. Gerba. *Environmental Microbiology*. Academic Press, 2nd edition, 2009.

[55] P. Markham. *Organelles of filamentous fungi. In: N. A. R. Gow and G. M. Gadd (ed). The Growing Fungus*. Chapman and Hall, 1995.

[56] G. E. Mass. *Schaum's Outlines: Continuum Mechanics*. McGraw Hill, 1970.

[57] D. Moore, G. D. Robson, and A. P. J. Trinci. *Dictionary of Science and Technology*. Academic Press, 1992.

[58] D. Moore, G. D. Robson, and A. P. J. Trinci. *21st Century Guidebook to Fungi*. Cambridge University Press, 2011.

[59] P. Narayanasamy. *Microbial Plant Pathogens-Detection and Disease Diagnosis: Fungal Pathogens*, volume I. Springer, 2010.

[60] D. W. Parry. *Plant Pathology in Agriculture*. Cambridge University Press, 1990.

[61] M. A. Penalva, R. T. Rowlands, and G. Turner. The optimization of penicillin biosynthesis in fungi. *Elsevier*, 16(11), 1998.

[62] D. R. Pittenger. *Retail Garden Center Manual*. UC Peer Reviewed, 9th edition, 2006.

[63] J. C. Pommerville. *Alcamo's Fundamentals of Microbiology*. Jones and Bartlett, 9th edition, 2010.

[64] T. A. Proseus, J. K. E. Ortega, and S.J. Boyer. Separating growth from elastic deformation during cell enlargement. *Plant Physiology*, 119, 1999.

[65] D. G. Rao. *Introduction to Biochemical Engineering*. Tata McGraw Hill, 2nd edition, 2010.

[66] C. M. Regalado, B. D. Sleeman, and K. Ritz. Aggregation and collapse of fungal wall vesicles in hyphal tips: A model for the origin of the spitzenkorper. *Philosophical Transactions of the Royal Society of London*, 352:1963–1994, 1997.

[67] M. O. Reinhardt. Das wachsthum der pilzhyphen. *Jahrbucher fur Wissenschaftliche Botanik*, 23:479–566, 1892.

[68] M. G. Roca, J. Arlt, C. E. Jeffree, and N. D. Read. Cell biology of conidial anastomosis tubes in neurospora crassa. *Eukaryotic Cell*, 4(5):911–919, 2005.

[69] K. Rogers. *Fungi, Algae and Protists.* Britanicca Educational Publishing, 2011.

[70] J. S. Rokem. *Biotechnology: Industrial Mycology*, volume VI. Encyclopedia of Life Support Systems, 2007.

[71] M. Schaechter. *Eukaryotic Microbes.* Academic Press, 2011.

[72] T. W. Secomb. Mechanics and computional simulation of blood flow in microvessels. *Medical Engineering and Physics*, 33:800–804, 2011.

[73] T. W. Secomb and J. F. Gross. Flow of red blood cells in narrow capillaries: Role of membrane tension. *Int. J. Microcirc: Clin. Exp*, 3:229–240, 1983.

[74] R. A. Serway, J. R. Faughs, and C. Vuille. *College Physics*, volume I. Brooks Cole, 9th edition, 2011.

[75] H. Singh. *Mycoremediation: Fungal Bioremediation.* John and Wiley Sons, 2006.

[76] S. E. Smith and F. A. Smith. *Diversity and Integration in Mycorrhizas: Proceedings of the 3rd International Conference on Mycorrhizas.* Kluwer Academic, 2002.

[77] G. Steinberg. Hyphal growth: A tale of motors, lipids and spitzenkorper. *Eukaryotic Cell*, 6(3):351–360, 2007.

[78] P. Tauro, K. K. Kapoor, and K. S. Yadav. *An Introduction to Microbiology.* New Age International, 2004.

[79] M. R. Taylor and N. A. Campbell. *Student Study Guide for Biology.* Benjamin and Cummings, 2002.

[80] S. Timoshenko. *Theory of Plates and Shells.* McGrow-Hill, 1940.

[81] S. H. Tindemans, N. Kernb, and B. M. Mulder. The diffusive vesicle supply center model for tip growth in fungal hyphae. *Journal of Theoretical Biology*, 238:937–948, 2006.

[82] J. S. Tkacz and L. Lenge. *Advances in Fungal Biotechnology for Industry, Agriculture and Medicine*. Kluwer Academic, 2004.

[83] A. P. J. Trinci and Collinge. Hyphal wall growth in neurospora crassa and geotrichum candidum. *Journal of General Microbiology*, 91:355–361, 1975.

[84] A. P. J. Trinci and P. T. Saunders. Tip growth of fungal hyphae. *Journal of Theoretical Biology*, 103:243–248, 1977.

[85] M. J. Waites, N. L. Morgan, J. S. Rockey, and G. Highton. *Microbiology: An Introduction*. Blackwell Science, 2001.

[86] H. A. B. Wsten, M. Richter, and J. M. Willey. Structural proteins involved in emergence of microbial aerial hyphae. *Fungal Genet Biol*, 27:153–160, 1999.

[87] W. M. Zheng and J. Liu. Helfrich shape equation for axisymmetric vesicles as a first integral. *Physical Review Letter*, 48(4):2856–2860, 1993.

[88] O. Y. Zhong-can and W. Helfrich. Bending energy of vesicle membranes: General expressions for the first, second, and third variation of the shape energy and applications to spheres and cylinders. *Physical Review Letter*, 39(10):5280–5288, 1989.